UNIVERSITY OF BRASILIA
GEOSCIENCE INSTITUTE
GRADUATE PROGRAM IN GEOLOGY

Short-term paleoceanographic changes across the Oceanic Anoxic Event (OAE) 1b in the Aptian-Albian Poggio Le Guaine core (Umbria Marche Basin, Italy)

Mudanças paeloceanográficas de curto prazo durante o Oceanic Anoxic Event (OAE) 1b no testemunho PLG do Aptiano-Albiano (Bacia Umbria-Marche, Itália)

PAULA HARETHUSA PEREIRA COSTA VIDAL

Dissertação de Mestrado nº 532

Brasília, 2024

PAULA HARETHUSA PEREIRA COSTA VIDAL

Title: **Short-term paleoceanographic changes across the Oceanic Anoxic Event (OAE) 1b in the Aptian-Albian Poggio Le Guaine core (Umbria Marche Basin, Italy)**

Titulo: Mudanças paeloceanográficas de curto prazo durante o Oceanic Anoxic Event (OAE) 1b no testemunho PLG do Aptiano-Albiano (Bacia Umbria-Marche, Itália)

Dissertation submitted to the Graduate Program in Geosciences at the University of Brasília as a partial requirement for obtaining the title of Master in Geology.

Advisor: Prof. Dr. Martino Giorgioni
(*Universidade de Brasilia)*

Co-advisor: Prof. Dr. Jairo F. Savian
(*Universidade Federal do Rio Grande do Sul*)

Examining Committee:

Prof. Dr. Gabriele Gambacorta
(*University of Firenze - Italy*)

Prof. Dr. Stéphane Bodin
(*Aarhus University - Denmark*)

Ficha catalográfica elaborada automaticamente,
com os dados fornecidos pelo(a) autor(a)

HV649sm

Harethusa Pereira Costa Vidal, Paula
Mudanças paeloceanográficas de curto prazo durante o Oceanic Anoxic Event (OAE) 1b no testemunho PLG do Aptiano-Albiano (Bacia Umbria-Marche, Itália) / Paula Harethusa Pereira Costa Vidal; orientador Martino Giorgioni; co-orientador Jairo Savian. Brasília, 2024.
121 p.

Dissertação(Mestrado em Geologia) Universidade de Brasília, 2024.

1. eventos de anoxia oceánicos. 2. isotopos de carbono. 3. isotopos de neodimio. 4. OAE 1b. 5. paleoceanografia. I. Giorgioni, Martino , orient. II. Savian, Jairo , co-orient. III. Título.

Acknowledgements

First, I would like to thank my family – parents, brothers and nephews - but especially my mum, Luzia, who always gave me the support and motivation to have the best education in every levels.

Thank to my advisor Martino for the opportunities, patience, motivation and all the guidance over the last few years. I extend my gratitude to prof. Jairo Savian (UFRGS), Fabrizio Frontalini, Carla and the students from University of Urbino, I had a great time in Italy.

I would like to thank Gabi Fazio, Gabriel Moizinho, Andre Foguinho, prof. Elder Yokoyama, prof. Marco Ianniruberto and prof. Jeremie Garnier for all the contributions and support in this work.

A special thanks to these friends: Gabi Oliveira, Lucas Bittencourt, Silvia Gehlen, Lais Ossami, Mariana Guedes, for helping me in so many ways.

Thanks God and the whole universe for giving me faith and provisions in my life.

Finally, thanks to Geology, this science that a cherish in my heart since my childhood.

This study was financed in part by the “Coordenação de Aperfeiçoamento de Pessoal de Nível Superior - Brasil (CAPES)” - Finance Code 001, and Conselho Nacional de Desenvolvimento Científico e Tecnológico (CNPq), process n. 307158/2020-9

List of Figures

Fig.11 - Stratigraphic framework of the Poggio le Guaine core drilled on September 2010 with real stratigraphic depths according to bed dip measurements. Also shown are the occurrence and distribution of the organic-rich black shales including the marker beds resulting from Oceanic Anoxic Events (OAEs) and the discrete intervals where reddish colored beds become dominant (Cretaceous Oceanic Red Beds) (Coccioni et al., 2014). The 4 horizons of *OAE* 1b in this study 113/Jacob, Killian, Monte Nerone and Urbino/Paquier

Fig. 12 - Location of the Poggio le Guaine drill site in the Umbria-Marche Basin (northern Apennines, central Italy). The location of the Piobbico drill site—where an 84-m-thick core extending from the upper Albian down to the uppermost Barremian was drilled in 1982—is also shown (Coccioni, 2012)

Fig. 13 - Paleogeographic distribution of OAE 1b records. Early Albian paleogeographic map modified after Bodin (2023) A. Localities spanning the Aptian - Albian transition where lithological, geochemical, or paleontological evidence relates to the OAE 1b sensu *lato*. 1. Vocontian Basin, France (Breheret and Crumiére, 1989; Herrle et al., 2004). 2. Umbria-Marche Basin, Italy (Coccioni et al., 2014). 3. Helvetic shelf and Briançonnais Domain, Switzerland (Strasser et al., 2001; Follmi et al., 2007). 4. Basque–Cantabrian Basin, Spain (Milla´n et al., 2014). 5. Algarve Basin, Portugal (Heimhofer et al., 2003). 6. Essaouira-Agadir Basin, Morocco (Peybernes et al., 2013). 7. Lower Saxony Basin, Germany (Mutterlose et al., 2003). 8. Wessex Basin, England (Grocke, 2002). 9. DSDP site 545, Mazagan Plateau, eastern Proto - North Atlantic (Wagner et al., 2008; Huber and Leckie, 2011; McAnena et al., 2013). 10. ODP site 1049, Blake Plateau, western Proto-North Atlantic (Erbacher et al., 2001; Huber and Leckie, 2011). 11. Northern Cordillera, Mexico, and Comanche Platform, Texas (Bralower et al., 1999; Phelps et al., 2015). 12. Western Interior, Utah (Ludvigson et al., 2015). 13. Axel Heiberg Island, Canada (Herrle et al., 2015). 14. Northeastern peri-Tethys, Caucasus region (Gavrilov et al., 2019). 15. Yujingzi Basin, northwest China (Suarez et al., 2018). 16. Hokkaido, Japan (Ando and Kakegawa, 2007). 17. Tunisian Platform, Tunisia (Ben Chaabane et al., 2019). 18. Western Platform, Peru (Navarro-Ramirez et al., 2015). 19. Central Proto-South Atlantic, Brazil (Caetano-Filho et al., 2017). 20. Southern Tibet, China (Li et al., 2016). 21. DSDP Site 511, Falkland Plateau, southern South Atlantic (Huber and Leckie, 2011; Huber et al., 2018; Matsumoto et al., 2023). 22. ODP sites 1207 and 1213, Shatsky Rise, northwest Pacific (Robinson et al., 2004). 23. DSDP site 463, Resolution Guyot, Mid-Pacific Mountains (Price, 2003; Matsumoto et al., 2020). 24. Fuxin Basin, Northeast China (Xu et al., 2022). B–F. For each OAE 1b sub-levels, map showing the localities where their presence can be identified (star) or suspected (circle), as well as the type of lithological expression

Fig. 14 - Isotopic geochemistry of *OAE* 1b. Integration of isotopic composition data of carbon $\delta^{13}C_{carb}$ from UnB (this study) and Petrobras (2012). In blue points, intervals of Petrobras data; in orange points, UnB data. Neodymium isotopic composition (εNd) for the Aptian - Albian interval ranging from -9 to -17 units.

Fig.15 - XRF data (Al, Si, K, Ti, Fe, V, Cd, Ca, Mn) from PLG core correlated to stratigraphic Marne a Fucoidi Formation.

Fig.16 - Graphs comparing the correlation among XRF data normalized and non-normalized for Ti, Fe, Al and Ca.

Fig. 17 – *Loadings Plots* in reference to Principal Component 1 for Jacob Level. The principal element positively correlated to PC1 is Cadmium. Data generated by PAST4 software.

Fig.18 - *Loadings Plots* in reference to Principal Component 1 for Killian Level. The terrigenous Al, Si, K, Ti, and Fe are the principal element positively correlated to PC1. Data generated by *PAST4* software.

Fig. 19 - *Loadings Plots* in reference to Principal Component 1 for Monte Nerone Level. The terrigenous Al, K, Si, Ti and Fe are the principal elements positively correlated to PC1. Data generated by *PAST4* software.

Fig. 20 - *Loadings Plots* in reference to Principal Component 1 for Urbino Level. PC1 is positively correlated for the terrigenous elements Al. Si, F e K. Data generated by PAST4 software

Fig. 21 - PCA *Scatter Plots* of the anoxic Aptian - Albian levels: Urbino, Monte Nerone, Killian and Jacob. Data generated on *PAST4* software.

Fig. 22 – *Loadings Plots* in reference to Principal Component 1 for PRE OAE 1b. The terrigenous Ti, Al, Si and Fe are the principal elements positively correlated to PC1. Data generated by *PAST4* software.

Fig. 23 – *Loadings Plots* in reference to Principal Component 1 for OAE 1b. The terrigenous Al, Si, K, Ti and Fe are the principal element positively correlated to PC1. Data generated by *PAST4* software.

Fig.24 - *Loadings Plots* in reference to Principal Component 1 for POST OAE 1b. The terrigenous Al, Si, Ti and Fe are the principal element positively correlated to PC1. Data generated by PAST4 software.

Fig.25 – PCA *Scatter Plot* of *Marne a Fucoidi* Stratigraphic Levels during Aptian – Albian OAE 1b. POST 1b (36.02 - 54.61m), OAE 1b (54.64 – 63.02m**)** and PRE OAE 1b (63.05 – 67.41m). (Data generated on *PAST4* software.

Fig. 26 - *Loadings Plots* in reference to Principal Component 1 for Green Level 1 (GL1). Si and Mn are the principal elements positively correlated to PC1. Data generated by *PAST4* software.

Fig.27 - *Loadings Plots* in reference to Principal Component 1 for Red Level 1 (RL1). The terrigenous Al, Si, Ti and Fe are the principal elements positively correlated to PC1. Data generated by PAST4 software.

Fig. 28 - *Loadings Plots* in reference to Principal Component 1 for Green Level 2 (GL2). Al, Si, Ti and Fe are the principal elements positively correlated to PC1. Data generated by PAST4 software.

Fig. 29 - *Loadings Plots* in reference to Principal Component 1 for Red Level 2 (RL2). Al, Si, K, Ti and Fe are the principal elements positively correlated to PC1. Data generated by PAST4 software.

Fig. 30 - Loadings *Plots* in reference to Principal Component 1 for Green Level 3 (GL3). Al, Si, K, Ti and Fe are the principal elements positively correlated to PC1. Data generated by PAST4 software.

Fig. 31 - *Loadings Plots* in reference to Principal Component 1 for Red Level 3 (RL3). High level of Nickel as the principal element positively correlated to PC1. Data generated by *PAST4* software.

Fig.32 – *Loadings Plots* in reference to Principal Component 1 for Green Level 4 (GL4). The terrigenous Al, Si, Ti, V and Fe are the principal element positively correlated to PC1. Data generated by *PAST4* software.

Fig. 33 – PCA *Scatter Plot* of Green (gL1, gL2, gL3 and gL4) and Red (rL1, rL2 and rL3) *Marne a Fucoidi* Stratigraphic Levels during Aptian – Albian OAE 1b. Data generated on *PAST4* software.

Fig.34: Correlation of upper Aptian-lower Albian intervals in the Umbria-Marche Basin (Poggio le Guaine (PLG) core, on the left) with the Briers section (on the right, Bodin et al. 2023) through δ^{13}Ccarb

Fig. 35 – *Integration of our PLG εNd record and δ13C from Matsumoto et al. (2022) with elemental data from this study, Bodin et al. (2023) and Sabatino et al. (2015). Red lines, highlights the long-term cyclic trend of terrigenous elements.*

List of Tables

SUMMARY

Abstract

During mid-Cretaceous (125-89 Ma) the Earth experienced profounds changes in climate and paleoceanography, including extreme greenhouse climatic conditions and a reduction of oxygen at the bottom of the oceans world-wide, associated to episodes of significant deposition of marine organic matter rich sediments (black shales). These episodes are defined as Oceanic Anoxic Events (OAEs) occurred in the early Toarcian (T-OAE, ~183 Ma), early Aptian (Selli event, OAE 1a, ~120 Ma), early Albian (Paquier event, OAE 1b, ~111 Ma), late Albian (Breisthoffer-Pialli event, OAE 1d, ~100 Ma) and Cenomanian–Turonian (Bonarelli event, OAE 2, ~93 Ma). The OAE 1a and OAE 2 are the most intense events and are marked by a thick black shale layer in the stratigraphic records, with a $\delta^{13}C$ signature up to 4.5‰. Currently available data suggest that the major forcing of the OAEs was an abrupt rise in temperature, induced by rapid influx of CO_2 into the atmosphere from volcanogenic and/or methanogenic sources. The Aptian-Albian OAE 1b is considered the most extended in time of the Cretaceous OAEs, however with less extreme climatic conditions compared to the OAE 1a and OAE 2. The overall duration is estimated to be 3.8 Myr, and this event was characterized by reduced circulation and increased nutrient flux, which led to enhanced primary productivity and oxygen consumption in the water column, creating anoxic conditions. One of the most relevant records of this event occurs in the Marne a Fucoidi Formation, in the Umbria-Marche Basin, Central Italy. Here we study a record of the Marne a Fucoidi Fm. in the Poggio Le Guaine (PLG) section, which is a reference section for the Aptian-Albian interval. This pelagic sequence is defined by decimetric layers of black shales, intercalated and contrasting with layers of lighter, carbonate-rich sediments. The OAE 1b recorded in the PLG section is characterized by the occurrence of 5 organic matter-rich levels, which can be traced on regional-to-global scale: Jacob, Killian, Monte Nerone, Urbino, and Leenhardt. In this study, we present a multi-proxy analysis of the Aptian-Albian interval of the PLG section to discuss the mechanisms and paleoceanographic changes occurred during the period of the OAE 1b. Carbonate carbon isotopes allow the identification of anoxic events through the geochemical signature, with fluctuations in $\delta^{13}C$ ranging between 2‰ and 3.5‰. Nd isotope combined with geochemical elemental XRF analysis, suggests a relatively homogenous detrital sediment source throughout the studied interval, with excursions observed during the Killian, Monte Nerone, and Urbino levels. These fluctuations indicate a dominant ancient continental crust (or sedimentary rocks that have been extensively weathered from the continents) influence during

low εNd values, while less negative values are more radiogenic and suggest a mixture with marine sources. Despite the instability, OAE 1b stands out as a distinct event, differing significantly from OAE 1a and 2. Its exceptional nature is characterized by a prolonged duration, extremely unstable climatic conditions, and several unique features. Notably, OAE 1b lacks the extreme carbon cycle disruptions, classical positive geochemical excursions, and significant changes in oceanic circulation, sediment supply, or environmental conditions that are typically associated with other OAEs.

keywords: Isotopic geochemistry; Neodymium isotopes, Elemental geochemistry, Portable XRF, Principal Components Analysis, Oceanic Anoxic Event 1b

Resumo

Durante o Cretáceo Médio (125-89 Ma), a Terra passou por mudanças climáticas e Pale-oceanográficas, incluindo condições climáticas extremas, efeito estufa e uma redução global de oxigênio no fundo dos oceanos associada a episódios de deposição significativa de sedimentos marinhos ricos em matéria orgânica (folhelhos negros). Esses episódios são definidos como Eventos Anóxicos Oceânicos (EAOs) e ocorreram no início do Toarciano (evento Posidonienschiefer, T-OAE, ~183 Ma), início do Aptiano (evento Selli, OAE 1a, ~120 Ma), início do Albiano (evento Paquier, OAE 1b, ~111 Ma), final do Albiano (evento Breisthoffer-Pialli, OAE 1d, ~100 Ma) e Cenomaniano–Turoniano (evento Bonarelli, OAE 2, ~93 Ma). Os OAE 1a e 2 são os eventos mais intensos e são evidenciados por uma espessa camada de folhelho negro nos registros estratigráficos, com uma assinatura de $\delta^{13}C$ de até 4,5‰. Os dados atualmente disponíveis sugerem que a principal força motriz dos EAOs foi um aumento abrupto da temperatura, induzido por um influxo rápido de CO2 na atmosfera proveniente de fontes vulcanogênicas e/ou metanogênicas. O Evento Anóxico Oceânico 1b, no Aptiano-Albiano, é considerado o mais prolongado em tempo dos EAOs do Cretáceo, embora com condições climáticas menos extremas em comparação com os grandes eventos 1a e 2. A duração geral é estimada em 3,8 milhões de anos, e este evento foi caracterizado por uma circulação reduzida e um aumento no fluxo de nutrientes, o que levou a uma maior produtividade primária e consumo de oxigênio na coluna de água, criando condições anóxicas. Um dos registros mais relevantes deste evento ocorre na Formação Marne a Fucoidi, na Bacia Umbria-Marche, na Itália Central. Aqui, estudamos um registro da Formação Marne a Fucoidi na seção Poggio Le Guaine (PLG), que é uma seção de referência para o intervalo Aptiano-Albiano. Esta sequência pelágica é definida por camadas decimétricas de shales negros, intercaladas e contrastantes com camadas de sedimentos mais claros, ricos em carbonato. O EAO 1b registrado na seção PLG é caracterizado pela ocorrência de 5 níveis ricos em matéria orgânica, que podem ser rastreados em uma escala regional a global: Jacob, Killian, Monte Nerone, Urbino e Leenhardt. Neste estudo, apresentamos uma análise elemental multiproxy em alta resolução do intervalo Aptiano-Albiano da seção PLG para discutir os mecanismos e mudanças paleoceanográficas ocorridas durante o período do EAO 1b. Os isótopos de carbono em carbonatos permitem a identificação dos eventos anóxicos por meio da assinatura geoquímica, com flutuações em $\delta^{13}C$ variando entre 2‰ e 3,5‰. A combinação de isótopos de Nd com análise geoquímica elemental XRF sugere uma fonte de sedimento detrito

relativamente constante ao longo do intervalo estudado, com excursões notáveis nos níveis Killian, Monte Nerone e Urbino. Essas flutuações indicam uma influência dominante de crosta continental antiga (ou rochas sedimentares intensamente intemperizadas a partir dos continentes) durante baixos valores de εNd, enquanto valores menos negativos sugerem mistura com fontes marinhas e menos taxa de intemperismo. Apesar da instabilidade, o EAO 1b se destaca como um evento distinto, diferindo significativamente do EAO 1a e 2. Sua natureza excepcional é caracterizada por uma duração prolongada, condições climáticas extremamente instáveis e várias características únicas. Notavelmente, o EAO 1b carece das extremas interrupções do ciclo de carbono, excursões geoquímicas positivas clássicas e mudanças significativas na circulação oceânica, suprimento de sedimentos ou condições ambientais que são tipicamente associadas a outros EAOs

Keywords: Geoquímica isotópica; isótopos de neodímio; geoquímica elemental; XRF; Análise de Componentes Principais, Evento de Anoxia Oceânica.

CHAPTER 1 | Introduction

1.1 | The mid- Cretaceous Period

The Mid-Cretaceous period (125-89 Ma) was characterized by extreme greenhouse conditions, with global temperatures significantly higher than today, particularly at high latitudes (Barron, 1983; Huber et al., 2002; Pucéat et al., 2003; Erbacher et al., 2011; Giorgioni, 2012). Ocean surface temperatures were approximately 5°C warmer than present-day values, and sea levels were 5-170 meters higher, reaching the highest point in the last 250 million years (Haq et al., 1987; Miller et al., 2005; Giorgioni, 2012) (Fig. 1). Concurrently, continental rifting and volcanism in the central and south Atlantic facilitated the rapid breakup of Gondwana (Larson, 1991; Tarduno et al., 1991; Arthur et al., 1991; Erba & Larson, 1991; Bralower et al., 1994). Elevated atmospheric carbon dioxide (CO2) levels, comparable to ~1500 ppmv during the Cenomanian (Hong & Lee, 2012), sustained a strong warm climate. This active outgassing is attributed to the production of oceanic crust and/or massive volcanic activity (Larson, 1991; Matsumoto et al., 2022). The deposition of black shales during this period has been investigated, providing valuable insights into paleoenvironmental and paleoceanographic conditions.

During the mid-Cretaceous, the paleogeographic configuration consisted of two supercontinents, Laurasia and Gondwana, with the low-latitude Tethys Ocean expanding eastward. This setup, combined with the prevailing paleoclimatic conditions, shaped the ocean-climate system of the time. The warm climate suggests that polar ice sheets played a negligible role, although some studies propose their brief presence (Price, 1999; Miller et al., 2003; Bornemann et al., 2008; Mutterlose et al., 2009; Rodriguez Lopez et al., 2016).

The positioning of Laurasia and Gondwana restricted north-south oceanic connections, resulting in a predominantly equatorial oceanic circulation (e.g., Barron & Peterson, 1989; Föllmi & Delamette, 1991; Poulsen et al., 1998; Giorgioni, 2012). In the absence of polar ice caps and significant cold, deep-water formation, deep ocean currents were instead driven by the sinking of warm, saline waters in tropical and subtropical regions (e.g., Hay, 2008), contributing to stagnant conditions in parts of the ocean.

The Aptian-Albian interval, marking the onset of the mid-Cretaceous, is characterized by widespread deposition of organic-rich marine sediments, often occurring in cyclic alternation with bioturbated, less organic-rich facies. These cycles reflect Milankovitch orbital periodicities and are especially prevalent throughout the Tethys and the Atlantic (e.g., Berger & von Rad, 1972).

Between the end of the Early Cretaceous and the beginning of the Late Cretaceous, sedimentary successions become increasingly carbonate-rich, with a corresponding decline in organic content. Upper Cretaceous facies primarily consist of homogeneous micritic limestones, rich in calcareous plankton, indicating a more stable oceanic circulation. These facies, known as chalk, are distinctive of the Cretaceous period and even inspired its name (Huxley, 1868; Hay, 2008; Mortimore, 2011).

Another climate driving mechanism that has been investigated, it is the presence of large volcanic episodes leading to the formation of submarine or continental Large Igneous Provinces (LIPs), such as the Ontong Java, Kerguelen, and Caribbean plateaus (Hays and Pitman, 1973; Schlanger et al., 1981; Matsumoto, 2020), which affected ecological, climatic, and oceanic conditions across the planet during the Cretaceous.

The long-term greenhouse conditions of the mid-Cretaceous are punctuated by the deposition of these globally distributed organic-rich sediments (Erba and Tremolada, 2004; Wagner et al., 2004; Weissert and Erba, 2004; Sabatino, 2015) that were defined as expression of climatic and paleoceanographic perturbations, called Oceanic Anoxic Events (OAEs; Schanger & Jenkyns, 1976).

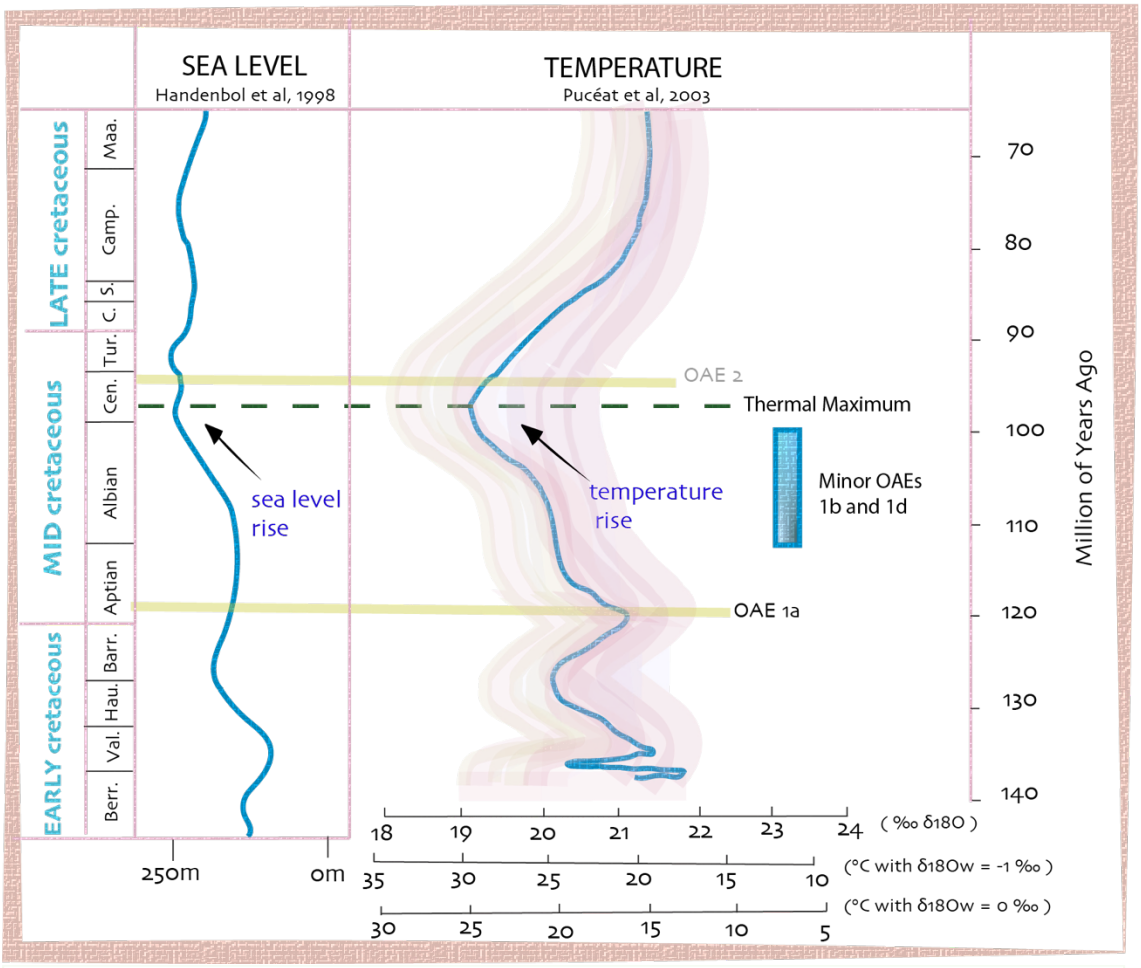

Fig.1- Global sea level and temperature trends through the Cretaceous, based on Hardenbol et al. (1998) and Pucéat et al. (2003) respectively. Periods of major and minor (blue box) Oceanic Anoxic Events (OAE) are also highlighted (after Giorgioni, 2012)

1.1.2 | The Mid-Cretaceous Paleoceanography

Cretaceous ocean circulation differed significantly from modern patterns, characterized by instability and localized dynamics. In contrast to the present day, where large-scale anoxia is unlikely, the Early Cretaceous experienced localized anoxic episodes that expanded to regional and global scales during the mid-Cretaceous.

The current oceanic structure depends on persistent wind systems, which are driven by stable atmospheric pressure patterns influenced by polar ice. However, for most of the Cretaceous, the polar regions were ice-free. In the absence of polar ice, seasonal shifts in high-latitude atmospheric pressure disrupted mid- and high-latitude wind systems.

Hay (2008) punctuated that constant mid-latitude west winds, there would be no subtropical and polar fronts in the ocean, no well-developed oceanic polynocline, and no tropical subtropical gyres dominating ocean circulation. Instead, ocean circulation was likely governed by mesoscale eddies, which played a crucial role in transporting heat toward the polar regions.

Interactions between the atmosphere and the ocean have influenced variations in marine biogeochemistry and sediment supply, with fundamental controls on the richness and quality of sedimentary organic matter and, on the distribution of petroleum source rocks and their potential generation (Wagner et al., 2012). Small-scale internal heterogeneities in black shales, which have been reported in all oceanic environments, are often associated with orbital fluctuations in continental runoff and marine upwelling. These two processes would be generically related under the ascending (tropical) and descending (subtropical) branches of the paleo-Hadley cells, with fluctuations occurring on variable time scales (seasonal, orbital, geological) and spatial scales (platform, margin, deep basin) (Wagner et al., 2012).

These dynamic variations give rise to distinctive patterns of organic matter quantity and quality, with better preservation occurring near continents where the forcing effects are more pronounced. In contrast, offshore environments in the centers of ocean basins experience more indirect effects of atmospheric forcing, which influence the mixing of surface waters and modify ocean currents in frontal systems. As a result, this leads to more widespread and often less distinct patterns of organic matter burial in the central ocean (Wagner et al., 2012). The primary characteristics of atmospheric circulation are inferred using paleogeography and ocean temperatures as boundary conditions. Compared to the present day, these features suggest a significantly weaker westerly wind belt and more pronounced seasonality of wind patterns, resulting in more extreme surface weather on continents. Additionally, the subtropical anticyclones were positioned slightly closer to the equator, and monsoon regimes prevailed over the continental margins bordering the Tethys and central Atlantic oceans (Lloyd, 1982).

1.2 | The Oceanic Anoxic Events (OAE)

The climate and oceanic dynamics of the mid-Cretaceous promoted periods of intense low oxygen concentration on the ocean floor. Such changes in the planet's paleoclimatic and paleoceanographic system were conceptualized and introduced in the geological literature by *Shlanger & Jenkyns* (1976) as Oceanic Anoxic Events (OAEs). These events have a relatively short duration (<1 Myr), and are expressed by the global deposition of black shales in marine settings (Jenkyns, 2010).

The initial observation and investigation of these events began in the 1970s through the DSDP (Deep Sea Drilling Project), a geoscientific research program to map and explore the Pacific ocean. It was observed that these pelagic black shales were synchronous and present in different parts of the planet, from the Pacific Ocean, Atlantic, and in Europe. Initially, two main events were defined: the *Aptian-Albian OAE* or *OAE 1* and the *Cenomanian OAE* or *OAE 2*. During both events, oceanic conditions favored the deposition of sediments enriched in organic matter. As studies progressed, minor OAEs were identified between the two main ones and called OAE 1b and 1d (figure 1). More OAEs were identified also in other periods, such as the Coniacian-Santonian (OAE 3; e.g. Mansour & Wagreich, 2022) and the Toarcian (T-OAE; Jenkyns, 1988). OAEs have a characteristic geochemical signature, which shows an increase of up to 4‰ in the $\delta^{13}C$ curve (Fig. 2). This is interpreted as expression of the great sequestration of isotopically light organic carbon in the oceans, due to the extensive deposition of black shales (Schanger et al., 1980; Jenkyns, 2010).

OAEs as global events are found in sedimentary records from different locations around the world. One of the most relevant records occurs in the Umbria-Marche Basin, Central Italy (Coccioni et al., 2012). In this pelagic succession, these events correspond to decimetric layers of shales rich in organic matter interspersed and contrasted with other under and overlying layers of lighter and carbonate-rich sediments (Coccioni et al., 2014). This succession records the OAE 1a and 2, which occur in the lower Aptian and upper Cenomanian, respectively, as well as the minor anoxic events, OAE 1b and 1d, in the lower and upper Albian, respectively. These lower intensity events have been less studied than the major ones, and present features

that still need to be characterized to advance in the general understanding of Cretaceous anoxic events (Coccioni et al., 2014; Sabatino et al., 2015; Gambacorta et al., 2020).

An increase in volcanic and hydrothermal activity associated with Large Volcanic Provinces (LIPs) has received attention in the last years as the trigger mechanism of the increase in atmospheric pCO_2 (e.g., ~1500 ppm during the Cenomanian; Hong and Lee, 2012) mainly because of new geochemical evidence supporting this theory (Larson, 1991; Matsumoto et.al, 2020; Matsumoto et al., 2022). This led to an increase in global temperature, as well as an increase in weathering rates and nutrient flows into the oceans, altering the chemistry of them, and substantially increasing the export productivity of the oceans (Adams et al., 2010; Frijia and Parente, 2008; Kerr, 1998; Kuroda et al., 2007; Sinton and Duncan, 1997; Turgeon and Creaser, 2008). The trigger mechanism associated to emplacement of LIPs was sporadic and rapid on geological timescales but produced nearly three times as much oceanic crust in the Cretaceous (considering LIPs and spreading centers) as in any comparable period (Larson 1991a, b). Consequently, fluxes of greenhouse gases and other chemical constituents, including nutrients, appear unusually large compared to the rest of the sedimentary record.

This study aims to investigate the paleoceanographic changes that occurred in the Umbria-Marche Basin during the Aptian-Albian OAE 1b intervals, through a geochemical analysis of elemental and stable isotopes records.

1.2.1 | **Oceanic Anoxic Event 1b**

The Aptian-Albian Oceanic Anoxic Event 1b (OAE 1b) is the longest-lasting of the Cretaceous OAEs, spanning approximately 3.8 million years (Coccioni et al., 2014, based on Grippo et al., 2004, and Huang et al., 2010). This event is distinguished by a series of sub-events, marked by organic-rich levels that can be correlated across regional to global scales. The event's climax occurred between the Kilian and Urbino levels, with the latter being the most pronounced sub-event (Bodin et al., 2023). Despite this, previous research has focused primarily on high-precision analyses of the Kilian and/or Urbino/Paquier levels, leaving uncertainties regarding the broader environmental and paleoceanographic context of OAE 1b and its distinction from the overall Aptian-Albian period.

The OAE 1b in the Umbria-Marche basins is currently defined by 5 black shale horizons across the Aptian-Albian boundary interval, called, from the lowest to the highest: *Jacob*, *Kilian*, *Monte Nerone*, *Urbino*/*Paquier*, and *Leenhardt*. These horizons are probably linked to short-term perturbations in the carbon cycle (Arthur and Premoli Silva, 1982; Bréhéret et al., 1986; Bréhéret and Delamette, 1987; 1989; Bréhéret, 1988; 1994; 1997 Premoli Silva and Sliter, 1999; Leckie et al., 2002; Huber and Leckie, 2011; Sabatino et al., 2015).

Together, the stratigraphic interval covered by these five organic matter-rich levels constitutes the OAE 1b cluster, according to some authors (e.g., Leckie et al., 2002; Coccioni et al., 2014; Sabatino et al., 2015), while others consider only the Paquier level (and its equivalent throughout the world) as the lithological expression of the OAE 1b (e.g., Bralower et al., 1993; Herrle et al., 2004; Jenkyns, 2010). This is based on the rationale that the Urbino level is the best expressed and globally traceable organic matter-rich layer in the Aptian/Albian boundary interval (Bodin et al, 2023).

The Monte Nerone level was previously correlated either to the Kilian level or the Paquier level in the Aptian Albian reference section of the Vocontian through, in SE France (e.g., Erbacher, 1994; Leckie et al., 2002; Trabucho Alexandre et al., 2011; Petrizzo et al., 2012). However, it has been finally recognized as a fifth organic matter-rich level comprised between the Kilian and Paquier levels (Coccioni et al., 2014).

These multiple events would be associated with intervals of cooling and sea level fall in the late Aptian, followed by subsequent sea level rise and global warming during the early Albian (Leckie et al., 2002). The $\delta^{13}C$ isotope curve marks a breakpoint between these periods, expressed by a positive excursion at the end of the Aptian followed by a pronounced negative shift at the beginning of the Albian (Weissert and Lini, 1991; Herrle et al., 2004).

This period it is also interpreted as the result of a combination of major geological and climatic factors. First, the existence of an extremely hot and uniform climate on a global scale, which reduced the mixing of water masses and, consequently, the general oxygenation of the ocean floors on a global scale. Secondly, the occurrence of large volcanic provinces (Large Igneous Provinces - LIP) which caused climate and carbon cycle disturbances (Turgeon & Creaser, 2008; Tejada et al., 2009; Jenkyns, 2010).

To elucidate the mechanisms during the OAE 1b and the paleoceanographic changes spanning the Late-Aptian to Early-Albian interval in the Poggio le Guaine section, we present a comprehensive multiproxy dataset that integrates previously published research. This study provides insights that will inform subsequent analyses, with a particular focus on the role of geochemical elements in modulating oceanic processes during the mid-Cretaceous.

1.3 | **Objectives**

This study investigates the paleoceanographic changes recorded across the Oceanic Anoxic Event 1b (OAE 1b) interval in the Marne a Fucoidi Formation. To track potential changes in clay sources, we analyzed Nd isotopes (εNd) in black shales. Additionally, high-resolution elemental XRF data, combined with statistical Principal Component Analysis, enable a detailed reconstruction of oceanographic dynamics in the western Tethys during the recurrence of anoxic episodes.

1.3.1 Specific Objectives

- Refine the geochemical characterization of the OAE 1b in the Umbria-Marche basin using C and Nd isotopes.
- Characterize the paleoceanographic and environmental changes occurred in the Umbria-Marche basin during the OAE 1b with elemental data obtained from XRF (X-ray Fluorescence).
- Investigate the lithological and geochemical variations within and out of the OAE 1b interval in the Umbria-Marche basin to constrain the palaeoceanographic mechanisms responsible for the changes recorded.

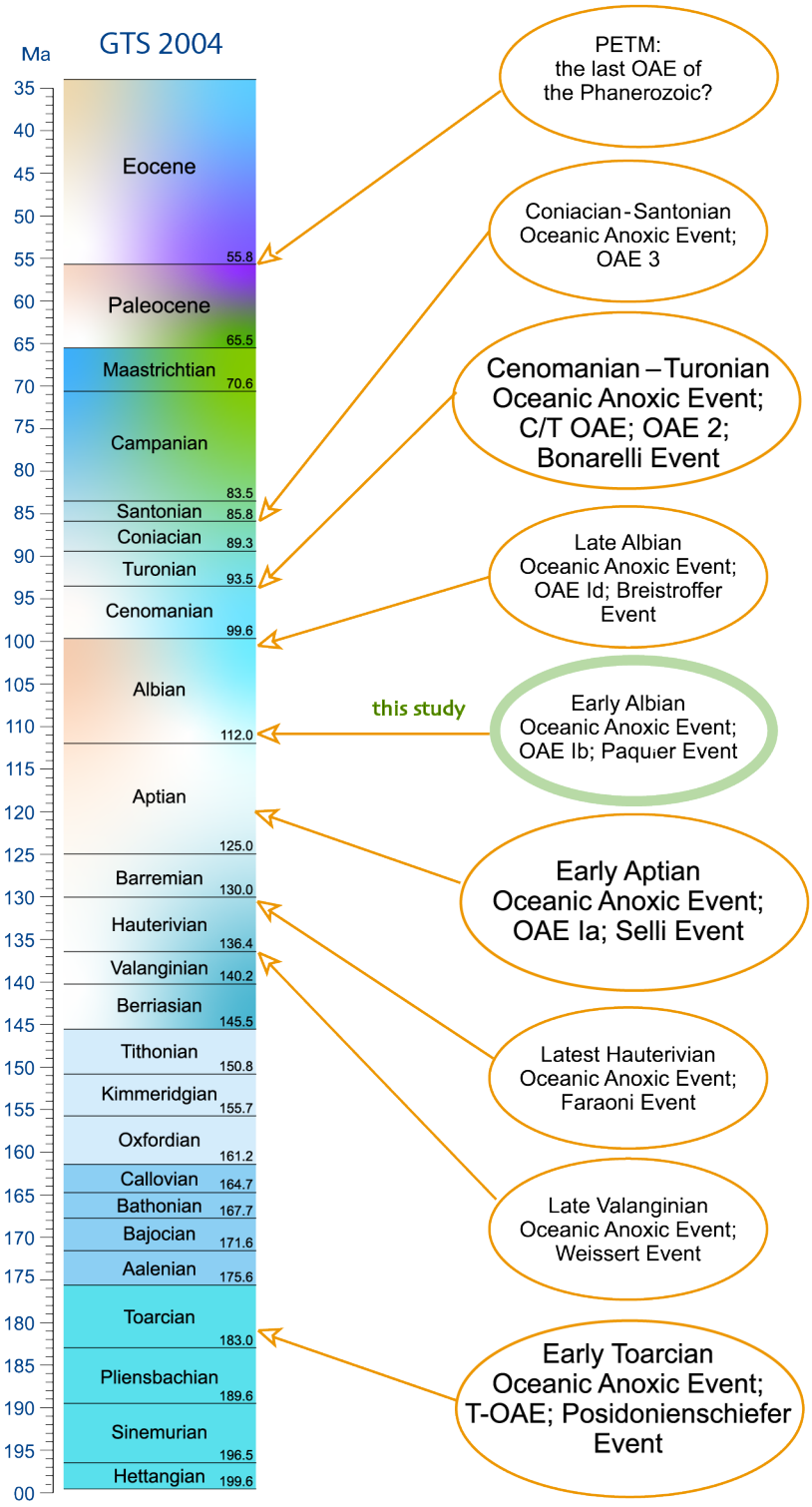

Fig.2 - Time scale (Gradstein et al., 2005; Coccioni, 2010) illustrating the stratigraphic position and nomenclature of OAEs. The major OAEs, identified by the extent of associated chemical change, are denoted by the larger, pink-colored ellipses. *OAE* 1b highlighted.

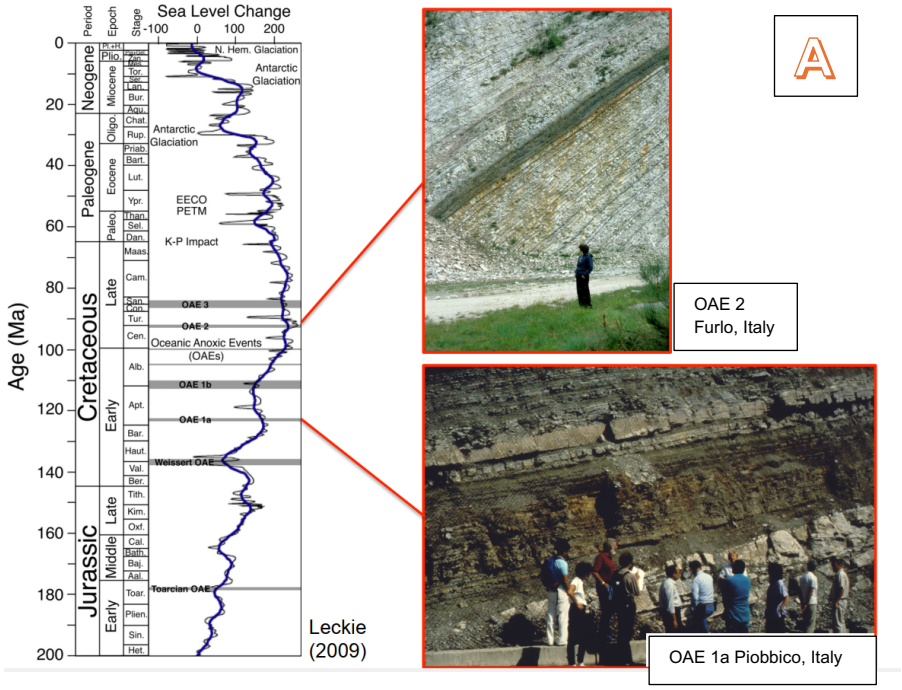

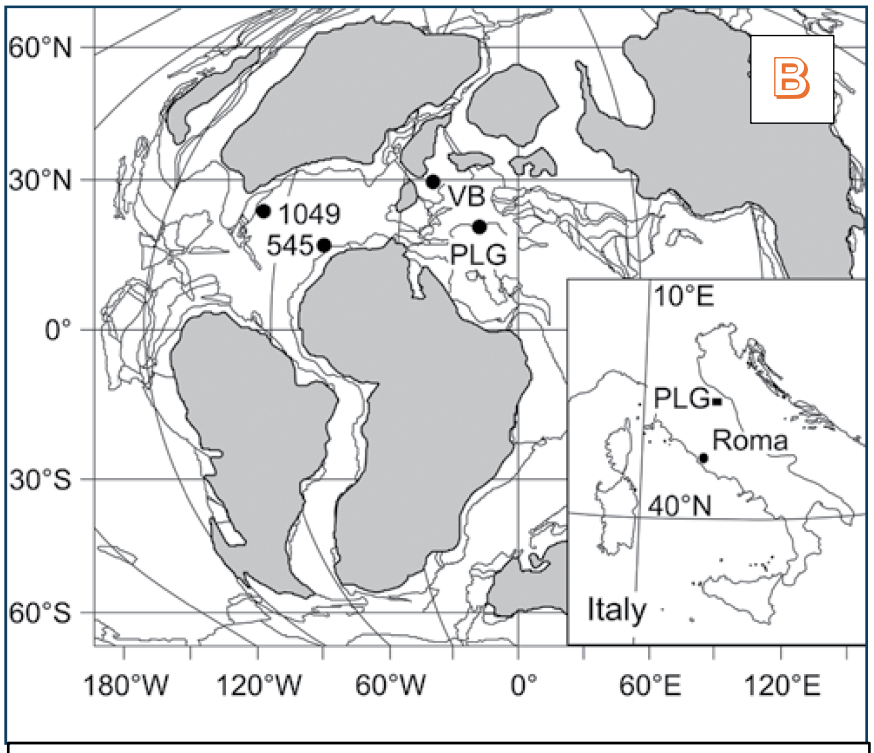

Fig. 3 – A) Outcrop of Cretaceous OAE1a and OAE 2. Paleogeographic Map at 113Ma modified after Huber and Leckie (2011) showing location of Poggio le Guaine (PLG) section.

CHAPTER 2 | Theoretical Background

2.1 | Carbon Cycle and Biological Pump

Carbon, an essential element for life, plays a crucial role in regulating Earth's climate and oxygenating the atmosphere. The biogeochemical carbon cycle facilitates the transfer of carbon between the atmosphere, terrestrial biosphere, hydrosphere, and lithosphere, occurring at varying rates. Atmospheric CO_2 easily dissolves in water, forming carbonic acid (H_2CO_3), which reacts with silicate rocks to produce bicarbonate ions (HCO^{3-}). These bicarbonate ions, transported by river water, are assimilated by marine organisms and eventually form sediments upon their death. Carbon is returned to the atmosphere through volcanic eruptions, a gradual process governed by geological mechanisms. On Earth's surface, carbon is primarily stored in oxidized reservoirs, including sedimentary carbonates, CO_2 (carbon dioxide), and HCO^{3-} (bicarbonate ion). or in reduced reservoirs, comprising organic matter, fossil fuels, and native carbon (Armstrong & Brasier 2005).

The significant variation in CO_2 considerably disturbs the balance between CO_2 and O_2 in the system, triggering the amplification of the greenhouse effect. Furthermore, the release of hydrate gases from melting glaciers is recognized by the scientific community as a potential source of CO_2 at the onset of anoxic events.

In the oceans, elevated CO_2 levels can trigger a cascade of effects, including intensified upwelling, decreased oxygen availability, accelerated hydrological cycles, enhanced organic productivity, increased continental weathering rates, and heightened nutrient discharge into oceans and lakes (Fig.4).

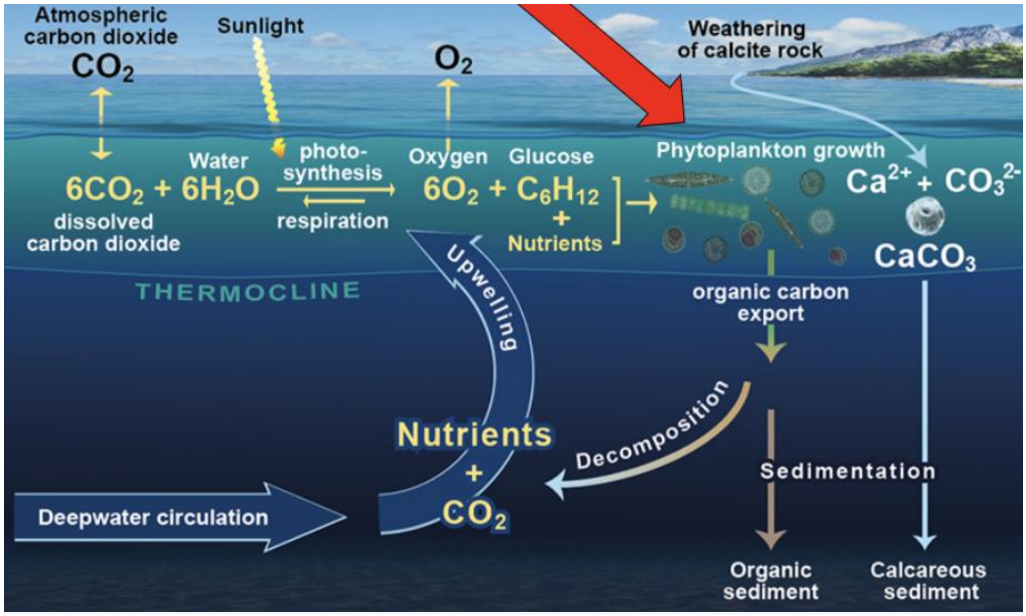

Fig.4 - The dynamic system that transports carbon from the surface ocean to the deep sea is called Biological Pump. In the surface ocean the carbon dioxide is dissolved, so phytoplankton uses this carbon and the sun light to grow.
(Image credit: V. Byfield, National Oceanography Centre - NOC)

2.2 | **Carbon fractionation and OAEs Isotopic Signature**

Carbon is one of the most abundant elements on Earth. It has atomic number 6 and atomic mass 12, occurring naturally as two stable isotopes (^{12}C - organic and ^{13}C - inorganic) and one unstable radioactive isotopes (^{14}C).

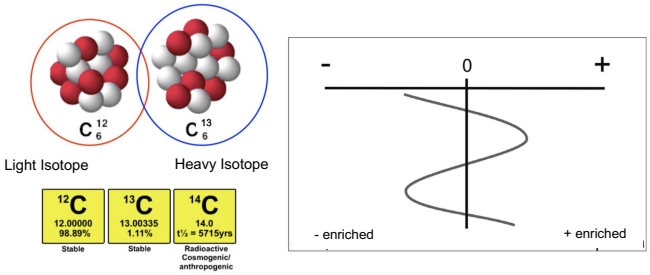

Fig.5 – Carbon isotopes and isotopic composition

The isotopic ratio as a relative measurement, adds fewer analytical errors and is given by equation 1:

(Eq.1) $$R = \frac{\text{heavy isotope}}{\text{light isotope}} < 1$$

In general, the heavier isotope is less abundant, and its ratio is less than 1.

The δ (Equation 2) is nothing more than comparing the sample ratio with the reference standard ratio; or how much the sample deviates from the standard. The standard used for C is V-PDB and for O V-PDB or V-SMOW (Rodrigues, G.B; Fauth, G., 2020)

(Eq.2) $$\delta = \frac{(\text{source} - \text{pattern})}{\text{pattern}} \times 1000$$

Carbon fractionation leads to the enrichment of organic carbon in ^{12}C and inorganic carbon in ^{13}C. During biological processes, the lighter isotope ^{12}C reacts more rapidly than ^{13}C, resulting in the enrichment of organic matter in ^{12}C. In contrast, marine carbonates are isotopically heavy, with an average $\delta^{13}C$ value of approximately 0 ‰ (ranging from 1 to 3 ‰), as reported by Hoefs (2004) and Armstrong & Brasier (2005). While organic matter is isotopically light, with an average $\delta^{13}C$ ratio value of around -25 ‰ (spanning -19 to -38 ‰) (Armstrong & Brasier, 2005).

Photosynthesis preferentially utilizes ^{12}C in the formation of organic matter, resulting in the enrichment of the water surface with ^{13}C relative to deeper, colder subsurface waters. Nutrients stored in the photic zone are transported from the subsurface waters, accompanied by excess ^{12}C released from decomposing organic matter. As these nutrients sink, they accumulate within the thermocline, a zone characterized by a sharp temperature gradient beneath the ocean's surface layer (Rodrigues, G.B; Fauth, G., 2020).

The fractionation of $\delta^{13}C$ values between air and water is sensitive to temperature variations (Wefer et al. 1999). During warmer periods of anoxia, increased temperatures enhance isotopic fractionation. The primary surface processes influencing $\delta^{13}C$ fractionation in marine carbonates are: surface water productivity, which removes ^{12}C resulting in a more positive $\delta^{13}C$ value; biological oxidation due to the respiration of organic matter in the water and on the ocean floor, resulting in the return of ^{12}C to the water column and a more negative $\delta^{13}C$ ratio value; recirculation and mixing bringing ^{13}C to the surface; the effects of the micro habitat; carbon deposits formed due to an increase in primary productivity, an increase in stagnant water and an increase in sediment accumulation rates, which result in an increase in the value of the $\delta^{13}C$ ratio in the ocean-atmosphere system; the vital effect, which is the influence of the metabolic effects of many species on carbonate precipitation; diagenesis, as some diagenetic fluids tend to capture ^{12}C and thus make the value of the $\delta^{13}C$ ratio slightly more negative (Armstrong & Brasier 2005).

The overall isotopic signature of Oceanic Anoxic Events is marked by a positive excursion in the $\delta^{13}C$ curve. In smaller events like 1b and 1d this anomaly is still not well defined.

The analysis of stable isotopes such as carbon and oxygen are applied both to shells of microfossils (foraminifera, calcareous nannofossils and radiolarians) and to rock material (total fraction of the rock). The Gas Bench II gas source mass spectrometers (GC-IRMS), Thermon Electron Delta Plus XP (Coccioni et al., 2014) and DeltaPLus XP (Matsumoto et al., 2020) are among the most used analytical techniques.

2.3 | **Nd isotope as a provenance tracer**

Neodymium is a rare earth element (REE) and has seven naturally occurring isotopes, with ^{143}Nd and ^{144}Nd being the most commonly studied in geochemical applications. ^{143}Nd is radiogenic, produced by the alpha decay of ^{147}Sm (Samarium) with a half-life of approximately 106 billion years (Yannick et al., 2017). ^{144}Nd is a stable isotope and serves as a reference for isotope ratio measurements. Nd is a rare earth element, making it a chemically immobile element that is not very sensitive to weathering processes. It has five natural isotopes (^{142}Nd, ^{143}Nd, ^{145}Nd, ^{146}Nd, ^{148}Nd). Among them, isotopes ^{142}Nd and ^{143}Nd are radiogenic, while

isotopes ^{144}Nd and ^{150}Nd are radioactive. However, these latter isotopes have sufficiently long half-lives (2.29 x 10^6 Ga and 6.8 x 10^9 Ga, respectively) to be considered stable on the scale of Earth's history. The radioactive isotope 147 of samarium (^{147}Sm) has a half-life of 106 Ga. Even though it is long, this half-life is sufficient to produce, after the decay of ^{147}Sm into ^{143}Nd, measurable variations in ^{143}Nd abundances over periods of several million years. The evolution of the concentration of ^{143}Nd over time is calculated by the following equation.

(Eq.3)
$$^{143}Nd_{actuel} = {}^{143}Nd_0 + {}^{147}Sm\ (e^{\lambda t} - 1)$$

where $^{143}Nd_0$ represents the initial abundance of ^{143}Nd, **t** the age of the studied system, and **λ** the radioactive decay constant of the ^{147}Sm-^{143}Nd pair, equal to 6.54 x 10^{-12} yr^{-1} (Lugmair and Marti, 1977).

The εNd signature of seawater at ocean margins is primarily controlled by local riverine weathering inputs and "boundary exchange" (BE) with sediments, as described by Lacan and Jeandel (2005). This process imprints the regional εNd signature on the water mass. In contrast, εNd exhibits quasi-conservative behavior in the ocean interior, making it a valuable tracer for ocean circulation and mixing (Goldstein and Hemming, 2003). Moreover, Nd isotopes are incorporated into Fe-Mn coatings on the seafloor, preserving the isotopic composition of the overlying water mass. These precipitates offer valuable insights into the state of ocean circulation at the time of their formation (Tachikawa et al., 2014).

The Nd isotope composition of clays and silts reveals that intense weathering processes significantly impact the distribution of Rare Earth Elements (REEs) in sediments. River systems exhibit isotopic variability between clay and silt fractions, providing valuable insights into geological processes (Bayon et al., 2015). Different clay fractions can be distinguished based on their distinct εNd values, indicating distinct sources (Liu et al., 2005). Furthermore, εNd isotopic analyses offer valuable information on long-distance sediment transport and recycling processes within the sedimentary system (Harlavan et al., 2021).

2.4 | **Major and Trace Elements Geochemistry**

Major elements, comprising more than 1% of a rock's weight, serve as the fundamental building blocks of minerals and rocks. They are essential for classifying and understanding geological materials. The most common major elements include silicon (Si), aluminum (Al), iron (Fe), calcium (Ca), magnesium (Mg), potassium (K), titanium (Ti), and manganese (Mn). These elements play a crucial role in the formation of the Earth's crust and significantly influence its physical and chemical properties (Sabatino et al., 2015). The abundance of major elements in bulk rocks can be accurately measured using techniques such as X-ray fluorescence (XRF), inductively coupled plasma optical emission spectrometry (ICP-OES), and inductively coupled plasma mass spectrometry (ICP-MS). XRF offers a non-destructive, rapid, and accurate analytical method. In contrast, ICP-OES and ICP-MS provide precise, multi-element measurements, making them valuable tools for geochemical analysis (Sabatino et al., 2015).

Trace elements, present in concentrations below 1%, are measured in parts per million (ppm) or parts per billion (ppb). Despite their low concentrations, trace elements provide invaluable insights into geological processes and conditions. Common trace elements include rare earth elements (REEs) such as neodymium (Nd) and cerium (Ce), transition metals like chromium (Cr) and nickel (Ni), and other elements including barium (Ba), and manganese (Mn). In seawater, trace elements are often linked to biological processes, such as phytoplankton uptake (Sabatino et al., 2015). Metals like iron (Fe), zinc (Zn), and copper (Cu) play a crucial role in marine productivity (Bruland et al., 2013). To analyze trace elements, highly sensitive techniques are employed, including inductively coupled plasma mass spectrometry (ICP-MS), X-ray fluorescence (XRF), and neutron activation analysis (NAA). ICP-MS is particularly valued for its ability to detect trace elements at extremely low concentrations, making it essential for detailed geochemical investigations. Although less common, NAA provides precise quantification of trace elements and is often utilized in specialized research applications (Sabatino et al., 2015).

In this study the following elements are considered for characterizing the detrital and authigenic/biogenic constituents:

Potassium (K)

Potassium (K) can serve as a valuable proxy for understanding past aridity and humidity conditions in geological and paleoenvironmental studies (Wehausen and Brumsack, 2001). Its concentration in sediments, soils, and various mineral deposits is influenced by weathering processes that are, in turn, strongly affected by climate. In arid climates, potassium is less likely to be leached from soils and rocks due to limited water availability, resulting in its relative accumulation in the mineral layers. In contrast, humid conditions promote the leaching and depletion of potassium as increased rainfall and water infiltration facilitate its removal from sediments. Moreover, potassium is often bound to clay minerals, such as illite, which form mainly in drier conditions, further reinforcing its importance as an indicator of past arid environments. By examining the concentration and distribution of potassium in sedimentary records, the humidity and aridity levels over time can be inferred (Calvert et al., 1993). This proxy can be particularly useful in reconstructing paleoclimate conditions and understanding shifts in climatic zones that impact ecosystems and weathering rates.

Calcium (Ca)

In the earth's crust, calcium makes up about 3.4% of the mass, and it is an abundant element in carbonate rich sediments, predominantly in the carbonate shells of organisms. Therefore, it generally represents the biogenic fraction (Duesing, 1985). The major source of calcium to the ocean is rivers, which carry 13.2 T mol/yr, derived mostly from weathering of carbonate minerals (about 70% of the total flux), and of silicate minerals (Morse and Mackenzie, 1990, Berner and Berner, 2012). The amount Ca^{2+} dissolved in the ocean varies with different locations and conditions, tightly linked with dissolved CO_3^{2-} ions. Calcium carbonate saturation is greatest in warm shallow water, where it precipitates inorganically or, more commonly, by biogenic processes (biomineralization). As the organisms die their hard or mineralized parts, fall and accumulate onto the ocean floor, or dissolve in the deeper water. This depends on the depth, temperature, and dissolved carbonate concentration. The depth at which $CaCO_3$ starts to dissolve is called Lysocline and the total dissolution is reached at the Carbonate Compensation Depth (CCD, Broecker, 2010). Therefore, the $CaCO_3$ flux in pelagic sediments depends on the balance between biogenic production at the surface and dissolution at the bottom. In this case, calcium contents can be used to track carbonate productivity and

generally reveals anticorrelation with the terrigenous elements, such as Al, Ti, K, which dilute the biogenic fraction (Wehausen and Brumsack, 2001).

Manganese (Mn)

In marine sediments, manganese is involved in redox reactions that are critical to the cycling of carbon, sulfur, and phosphorus. Mn(IV) is reduced to Mn(II), which can diffuse upward and re-oxidize, forming manganese oxides at oxic-anoxic interfaces (Burdige, 1993). Mn is often cycled between dissolved and particulate forms, with oxic conditions facilitating manganese precipitation and anoxic conditions promoting its dissolution (Elderfield, 1976).

Manganese is exchanged between its reduced Mn (II) form and precipitated Mn oxides in stratified marine basins. This cycling, particularly at oxic-anoxic interfaces, plays a significant role in regulating redox conditions and, therefore, makes Mn a useful proxy for understanding past ocean chemistry. Manganese fluxes in marine sediments respond also to diagenetic processes, which are influenced by redox boundaries and organic matter availability. Mn depletion is an indicative of oxygen-depleted, while its enrichment indicates well oxygenated bottom waters (Sabatino et al., 2015).

Cadmium (Cd)

Cadmium is a trace metal that has been widely used as a proxy for micronutrients and to study past redox conditions in marine environments. It exists in the ocean and sediments as Cd (II) (Morford, 1999) and its behavior is influenced by the redox state of the environment, making it a valuable tool for reconstructing past oceanic conditions and biogeochemical processes.

Cadmium in the ocean exists primarily as Cd^{2+} and is typically found in low concentrations. It is involved in biological processes, being taken up by phytoplankton and incorporated into their tissues. After the death of these organisms, Cd is released back into the water column or buried in sediments. The redox state of an environment influences the speciation, mobility, and deposition of Cd. In oxic conditions Cd is mostly present in dissolved form and can be removed from the water column by biological uptake and subsequent sedimentation.

In anoxic conditions, Cd can form insoluble sulfides (CdS), leading to its removal from the water column and enrichment in sediments (Morford, 1999). Cadmium has a vertical distribution in the oceans. In surface waters, concentrations are generally low due to uptake by organisms, while deeper waters contain higher levels due to the breakdown of organic matter that releases cadmium back into de water column. (Bruland, 1980)

Peaks in Cd concentrations in a sedimentary succession can indicate periods of enhanced organic matter export and deposition, due to high primary productivity or weak bottom ventilation and anoxic conditions. It is released to pore waters during organic matter diagenesis and authigenically enriched in sediments where Mn has been depleted (Gobeil, 1997).

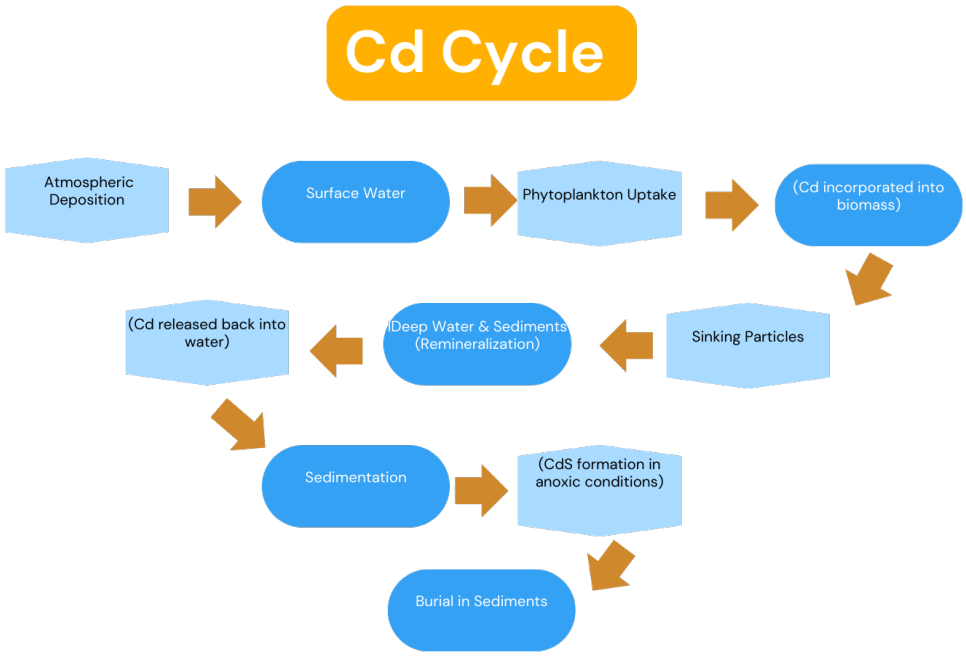

Titanium (Ti)

Titanium (Ti) is bound to minerals such as ilmenite and rutile. In pelagic sediments they are supplied by terrigenous sources, typically transported from continents to the open ocean by wind and rivers. In pelagic environments, titanium serves as an indicator of continental input and is often used to study dust flux, sedimentation rates, and climatic conditions over geological time. It is generally of eolian origin, associated with arid or semi-arid climates, as stronger winds increase the amount of Ti delivered into pelagic basin (Wehausen and Brumsack, 2001).

As titanium is largely insoluble and resistant to chemical weathering, it often serves as a "conservative" element, meaning it does not easily dissolve or alter in seawater. Therefore, when it reaches the open ocean, it settles slowly, often accumulating in sediments at very low rates typical of pelagic environments. It is also a refractory element, meaning it is relatively unaffected by diagenetic processes. This makes it a useful element in paleoceanography and paleoclimate research, as it preserves its initial environmental signature over long periods. Titanium, concentration can serve as a proxy for understanding past weathering on land and transport processes. For example, high levels of titanium can indicate periods of increased aridity or wind strength, as more dust would be transported from land to sea.

Vanadium (V)

Vanadium (V) is a redox-sensitive and relatively abundant trace metal (Wu, et al.,2020). Its oxidation state changes depending on the oxygen conditions, making it a useful indicator of environmental conditions in marine sedimentary settings. In oxygen-rich (oxic) environments, vanadium exists mainly in its +5 oxidation state as vanadate (VO_4^{3-}), which is more soluble, and in oxygen-depleted conditions, vanadium is reduced to vanadyl (VO^{2+}), or further to V^{3+} and V^{2+}, which are less soluble and tend to accumulate in sediments (Wu, et al.,2020).

Natural V mobilization from Earth's crust occurs dominantly through mechanical and chemical rock weathering, with lesser contributions from other pathways such as volcanic emissions and aeolian processes (Shlesinger et al., 2017). In the oceans, vanadium can cycle between dissolved and particulate forms depending on the oxygen levels, making it an important element for understanding the marine redox cycles. Its enrichment can also be

indicative of enhanced productivity and organic matter burial (Wehausen and Brumsack, 2001).

Nickel (Ni)

Nickel is a biologically active trace metal and its dissolved concentration depth profile in the ocean shows a nutrient-like behavior (Cameron & Vance, 2014). Ni is recognized for its distinct physical, chemical, and biological roles and its geochemical importance in both terrestrial and marine environments. It is taken up by marine phytoplankton at the ocean surface and is released back into the water column when organic matter is decomposed in deeper waters. Marine sediments, especially in regions with high organic matter, act as sources of recycled nickel back to seawater. Nickel concentrations in pore fluids of these sediments can be significantly higher than in bottom waters, due to local remineralization of organic matter (Bruggmann et al., 2020). Therefore, as a paleoceanographic proxy, Ni increases in reducing bottom conditions or high paleoproductivity.

Iron (Fe)

Iron is one of the most abundant metals on Earth. It undergoes redox cycling between Fe^{2+} and Fe^{3+} in natural environments, especially in marine sedimentary settings. Fe^{3+} is less soluble and precipitates forming Fe oxides, while Fe^{2+} tends to remain dissolved and precipitates only in euxinic conditions, in which it cand react with SO^{4-} and form FeS_2.

In pelagic sediments iron accumulates primarily from land, via atmospheric dust and river transport, or from hydrothermal sources. Within the sediments, iron undergoes redox reactions, influenced by microbial processes, impacting sediment composition and porewater chemistry (Haese et al., 1998). Iron can also contribute significantly to primary productivity, as it serves as micronutrient for phytoplankton (Bailey et al., 2011). Variations in iron minerals in pelagic sediments are influenced by the environment of deposition and works as an important proxy for detrital input and paleoredox conditions.

Aluminum (Al)

The major source of Al to the ocean is via detrital input, especially fluvial, since rivers carry large concentrations of Al rich particles, mainly composed of aluminosilicate minerals, such as clay minerals, micas, and feldspars (e.g. Kramer et al., 2004, Maring and Duce, 1987, Measures et al., 2005, Orians and Bruland, 1986). When terrigenous sediments enter the ocean, part of their aluminum content (1–15%) dissolves in the uppermost layer and is quickly distributed over the mixed layer by turbulent mixing (Hulten et al., 2013). Most of the Al, however, remains in the particulate phases and sinks to the bottom of the ocean, where it gets buried in the sediment (Gehlen et al., 2003, Sarmiento and Gruber, 2006). Therefore, in pelagic sediments, Al primarily reflects terrigenous input, especially that of fine fractions.

Silicon (Si)

Silicon is the second most abundant element in the Earth's crust, comprising about 28% by mass, mostly in the form of silicon dioxide (SiO_2) or silicate minerals. SiO_2 is commonly found in sand, quartz, and various rocks. It moves between the Earth's crust, oceans, and atmosphere through weathering, biological uptake, and sedimentation. The silicon cycle in the ocean is closely tied to the carbon and nitrogen cycles, as they can all be used by primary producers (Treguer et al., 2021). The inputs into the ocean include river discharge, groundwater, and atmospheric dust deposition, while the primary outputs involve the burial of biogenic silica from organisms like diatoms, radiolaria, and sponges (Tréguer et al., 2021). Thus, depending on the conditions, silica can be used as a proxy either for paleoproductivity or for terrestrial input.

2.5 **Handheld XRF Analysis**

XRF involves directing X-rays at a sample, causing the elements in the sample to emit fluorescent X-rays at characteristic energies. The emitted X-rays are detected and analyzed to determine the elemental composition (fig.10 and 11). This method has several advantages: it can be used for in situ analysis (portable device), is non-destructive, rapid (single reliable measurement in about 1 min), and is characterized by low costs (the only necessity are special measuring cups for powdered and liquid samples).

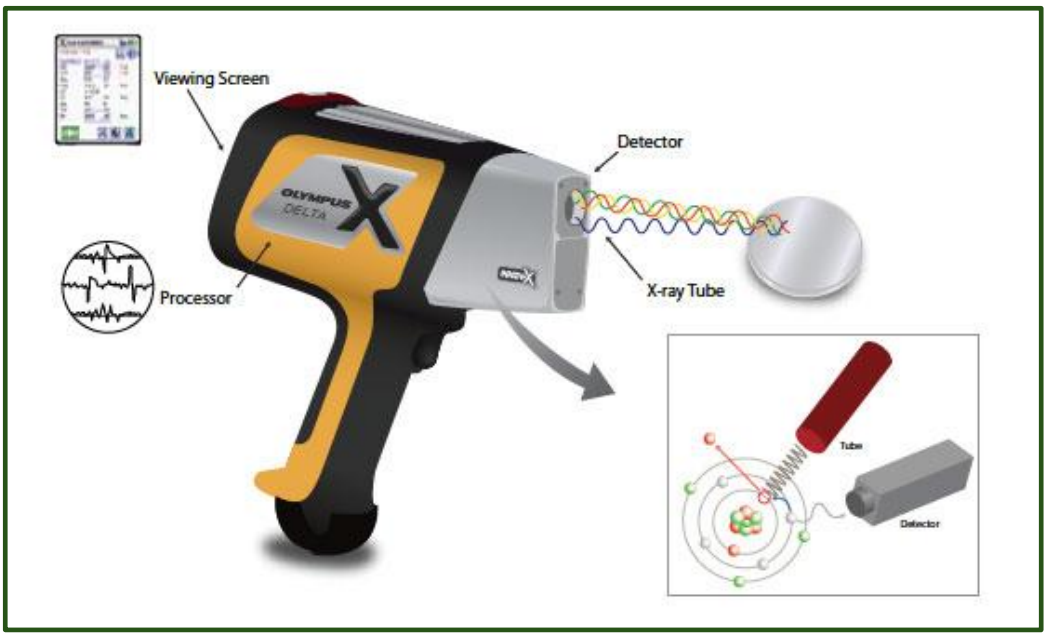

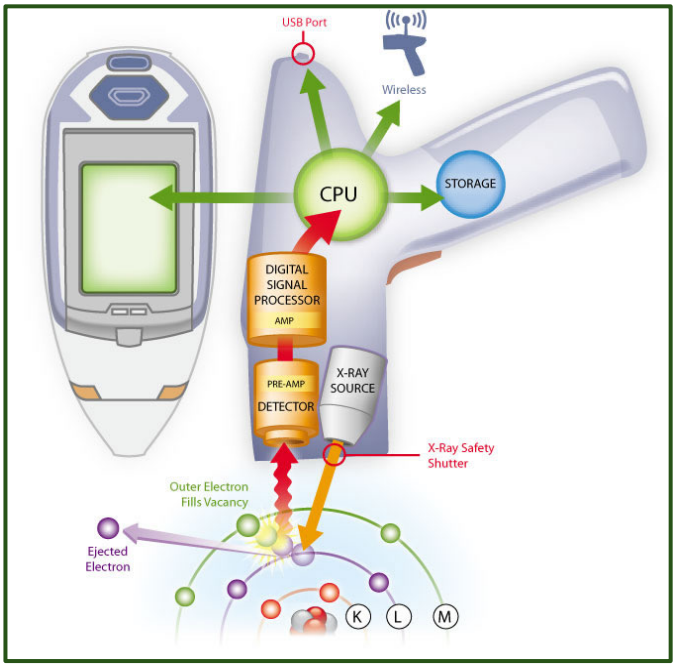

Fig.6 – DELTA X-Ray fluorescence Analyzer componentes.

Compared to conventional methods of elemental determination, such as inductively coupled plasma mass spectrometry (ICP-MS) or atomic absorption spectroscopy (AAS) techniques, it does not require sophisticated and expensive apparatus that, in addition to appropriate conditions and chemicals (eg. high purity argon 5 N; which is expensive), requires adequate laboratory personnel (Fleming, 2015; Ferreira, 2018; Frydrych & Jurowski, 2023)

On the order of limitations, XRF is generally less sensitive than mass spectrometers for trace element detection, and the results can be influenced by sample surface roughness and matrix effects.

Table 1: Advantages and Limitations of Handheld XRF analysis

Advantages	Limitations
Mobility and Convenience Easy to use in remote locations or in situ	**Surface Sensitivity** XRF only analyzes the surface of a sample. surface contamination may skew results
Time Efficiency Immediate analysis without sample preparation	**Detection Limits** While handheld XRF is effective for many elements, it may struggle to detect elements present at very low concentrations (trace elements)
Versatility *Can be used for a variety of materials*	**Matrix Effects** The composition of sample matrix can affect the accuracy of the results for certain elements.
Cost Effective Eliminates the need to send samples to a laboratory for analysis	**Calibration** Requires proper calibration and sometimes sample preparation to get the most accurate results

2.6 Principal Components Analysis (PCA)

With principal components analysis, many independent variables can be systematically reduced to a smaller, conceptually more coherent set of variables. These "Principal Components" are a linear combination of the original variables (George H. Dunteman, 1989)

PCA is a statistical technique used for reducing the dimensionality of data while preserving the most important information or patterns in the data. It's commonly employed in data analysis, machine learning, and various fields. It can transform a set of possibly correlated variables into a set of linearly uncorrelated variables called principal components. It helps in reducing the dimensionality of the data while retaining most of the variance. The first principal component captures the largest variance in the data, the second principal component captures the second largest variance, and so on (Greenacre, Michael et al., 2022).

PCA involves calculating the eigenvectors and eigenvalues of the covariance matrix of the data. The eigenvectors represent the directions of maximum variance, and the eigenvalues represent the magnitude of the variance. The shorter the graph arrow, the less important that variable was for the analysis. Here we explain some terms used to analyze the dataset in this study.

Eigenvalue and Eigenvectors

Eigenvalues indicate the amount of variance captured by each principal component, while the vectors representing the elements are called "singular vectors" or eigenvector for principal components and define the direction of maximum variance in the data. The top pathway of Fig. 7 shows how the principal components can be computed using the eigenvalue decomposition (EVD) of the covariance matrix (Greenacre, Michael et al., 2022)

The plot helps visualize how the original features relate to the principal components and how the data points are distributed in the new component space.

Loadings

Reveal how original features contribute to each component.

Variance

The percentage of variance explained by each principal component can be used to determine the importance of each component. For example, if the first principal component explains 60% of the variance, it is the most significant component in describing the data struct

Higher explained variance means the component captures more information about the data's variability.

PC1 is located on horizontal, x axis,
PC2 is located on vertical, y axis.

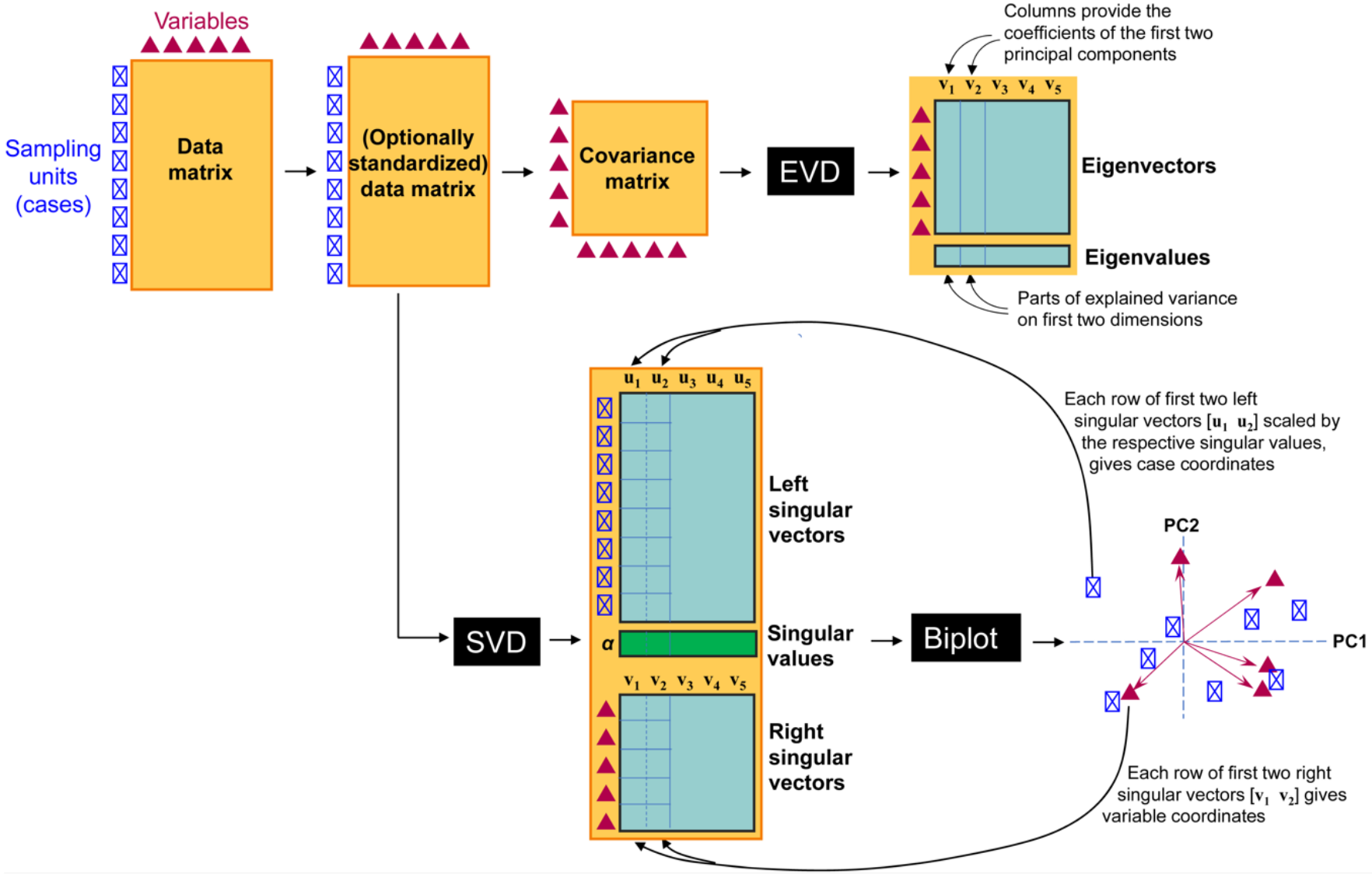

FIg.7 - Schematic view of the PCA workflow. The definition of the principal components (PCs) can be obtained using the eigenvalue decomposition (EVD) of the covariance matrix of the variables, Standardization is optional, but centering is mandatory, and if the variables are divided by their standard deviations, then the covariance matrix is the correlation matrix, and the analysis is sometimes referred to as : correlation PCA: . The first two PCs, PC1 and PC2, using the coefficients defined by the first two eigenvectors, given in (1) and (2), were used in Fig. 1 to obtain a spatial map of the countries. The lower pathway is a more efficient one, using the singular value decomposition (SVD) that leads directly to the positions of the countries as well as vectors serving as directions for the variables in the joint representation in Fig. 2. The eigenvectors are identical to the right singular vectors. For the lower pathway to be exactly equivalent to the upper one, the (optionally standardized) data matrix should be divided by $\sqrt{n}$ (Greenacre, Michael et al., 2022)

CHAPTER 3 | Geological Setting

3.1 | Geology and stratigraphy of the Umbria-Marche Basin

The Umbria-Marche Basin (UMB) is situated in the central part of Italy and is recognized as a reference succession for oceanic anoxic events. It outcrops in the Italian Apennines, forming the southern sector of the Northern Apennines, part of the peri-Mediterranean system of Alpine chains formed by differential movements between Africa and Europe plate. The region has undergone at least three major tectonic phases: (1) a Mesozoic extensional phase, (2) a Neogene compressional phase, and (3) a Late Miocene to Pleistocene extensional phase, confined to the Umbria sector. (Menichetti & Coccioni 2015).

The Umbria-Marche sedimentary basin formed in the late Triassic in a passive continental margin of the southern Tethys Ocean. The sedimentary succession was deposited on a continental-type crust, as evidenced by its affinity with the *Adria* microplate or the *Apulo* block, which probably represents a disarticulated fragment of the northern margin of the African continental plate (Menichetti & Coccioni 2015). The basin is over 3000 m thick stratigraphic succession records the thermal and mechanical subsidence history, transitioning from Jurassic carbonate platforms to the Paleogene pelagic realm. The upper part of the succession consists of Neogene terrigenous clastic, accumulated in a migratory foredeep system, reflecting the Apennines' deformation and sedimentation patterns encroaching into the Adriatic Foreland (Menichetti & Coccioni, 2015).

The Umbria-Marche basin's stratigraphic succession records the extensional regime triggered by the Late Triassic–Early Jurassic opening of the Tethys Ocean, marked by changes in facies type and thickness. This was followed by the deposition of Upper Triassic evaporites and dolomites, and the formation of an Early Jurassic carbonate platform. As the Alpine Tethys Ocean opened during the Early–Middle Jurassic, the persistent carbonate platform (Central Apennines, Latium–Abruzzi region) separated from the pelagic domain (Northern Apennines, Umbro-Marchean region) through a slope-to-basin transitional domain. The extensional phase ended during the Early Cretaceous with the deposition of the Maiolica Fm., which

homogenized lithological facies while maintaining bathymetric differences between former structural highs and lows (Menichetti & Coccioni, 2015).

Sedimentation in the area became more homogeneous with the deposition of the Marne a Fucoidi Formation in the early Aptian. This marked a transition towards hemipelagic lithotypes, characterized by carbonates and marls with abundant chert, which persisted throughout the Late Cretaceous and Paleogene. The Cretaceous Umbria-Marche (UMB) sequence is lithologically subdivided into distinct formations and members, based on variations in color, carbonate content, and the presence or absence of chert and black shales (Menichetti & Coccioni, 2015). A 750 m thick sequence can be recognized, comprising the following formations:

- Maiolica Formation (upper Tithonian – lower Aptian)
- Marne a Fucoidi Formation (lower Aptian – upper Albian)
- Scaglia Bianca Formation (uppermost Albian - lowermost Turonian)
- Scaglia Rossa Formation (lowermost Turonian – lower Lutetian)

3.2 | **Marne a Fucoidi Formation**

The unit of Marne a Fucoidi Formation consists of alternating layers of black, green, and red marlstones and limestones tied to varying oceanographic conditions, such as oxygen depletion and enhanced oxygenation at different times (Giorgioni et al., 2017). It has been studied in detail over the last 36 years, in various outcrops and cores (e.g. Herbert & Fischer, 1986; Tornaghi et al., 1989; Premoli Silva et al. 1989a, b; Grippo et al., 2004; Tiraboschi et al., 2009, Giorgioni et al., 2012). More specifically is observed grayish greenish, bioturbated, pelagic marls and marly limestones, alternating with black shales and most of the color variations reflect couples and bundles matching with Milankovitch periodicities (Herbert & Fischer, 1986; Grippo et al, 2004), but the succession is also punctuated by some meter thick red beds. These sediments could reflect highly variable redox conditions at the bottom of the basin, testifying to a very unstable environment and probably very sensitive to orbital forcing (Grippo et al., 2004; Tiraboschi et al, 2009; Giorgioni et al., 2012). Similar facies patterns are described from other Tethyan localities, suggesting that these unstable conditions were at least

of regional extent (e.g. Wortmann et al., 1999; Luciani et al., 2007; Ylmaz, 2008; Skupien et al., 2009).

High-resolution geochemical analyses indicate that the Marne a Fucoidi Formation recorded significant variability in oxygen levels, driven by orbitally forced changes. These oxygen fluctuations were crucial in controlling the deposition of organic-rich black shales, which reflect unstable circulation patterns characteristic of the Albian (Giorgioni et al., 2017).

Several researchers have investigated the variations between the different lithofacies in the Marne a Fucoidi and sediments of Aptian-Albian age. This study investigates whether geochemical data, obtained through XRF scanning of samples from the PLG core, can provide insights into the fluctuating surface and bottom water conditions that affected the Tethys Ocean during the Aptian-Albian. The XRF scanning technique offers a continuous, high-resolution response that enables detailed examination of transitions between different lithologies.

Fig.8 – PLG core log and stratigraphic section in field. Urbino, Italy (Pictures provided by Prof. Dr. Fabrizio Frontalini).

3.3 | The Poggio le Guaine (PLG) section

The section investigated in this study is from the Poggio le Guaine (PLG) site (fig.8) (lat. 43°32'29.06" N, long. 12°34'51.09" E) that is located on the Monte Nerone ridge of the Umbria–Marche Basin, 6 km west of the town of Cagli (Marche Region; Coccioni et al., 2012). A core 95m long was drilled through the succession in 2012 encompassing the entire Marne a Fucoidi Formation and including the lower and upper boundaries with the Maiolica and Scaglia Bianca formations, respectively.

It was deposited above the CCD (Calcite Compensation Depth), at a paleodepth around 1000-1500 mbsl and presents the most preserved and continuous sedimentary succession of event 1b and 1d. The rare occurrence of thick siliceous fragments along this section is considered an indicative of a pelagic deposition (Coccioni, 1990; 2004). The pre-OAE 1b interval comprises mainly reddish or olive gray clayey limestone and marl enriched in large, heavily calcified planktonic foraminifera, while the OAE 1b interval (Marne to Fucoidi Formation) is characterized by cyclic alternation of gray marls/mudstones -greenish to olive-grey with black shales. (Matsumoto et al., 2020).

The 113/Jacob, Kilian, Monte Nerone, Urbino/Paquier, and Leenhardt levels are the sedimentary expression of the OAE 1b sub-events. The equivalent 113/Jacob level is the first organic matter-rich sediment deposited during *OAE* 1b. Here we analyze the first four *OAE* 1b from the base to the top (Jacob, Killian, Monte Nerone and Urbino/Paquier).

3.3.1 | The expression of the OAE 1b

The Oceanic Anoxic Event 1b is expressed by 5 levels of black shales enriched in organic matter. This study comprehends 4 of them, they are:

First sub-event: Jacob Level

Jacob is the first organic-rich expression of the OAE 1b. The TOC (total organic carbon) levels in the Jacob level vary but tend to be moderately elevated, indicating some organic carbon preservation. However, TOC values are generally less than 1%, except for a few intervals where marine organic matter accumulation increased due to enhanced surface productivity. The black shale horizons at this level show an increase in organic carbon burial rates suggesting reduced bottom water ventilation (Sabatino et al., 2015).

Second sub-event: Killian Level

Kilian is the organic-rich expression of the second sub-event of the OAE 1b, with up to 3,5% carbonate carbon isotope composition measured in this study and also includes organic matter of terrestrial origin (e.g., Bréhéret 1994; 1997; Herrle 2002; Coccioni, 2015). This level formed under increasing surface water productivity and enhanced preservation of organic matter at the sea floor associated with the early Albian Sea–level rise (e.g., Herrle et al. 2004; Hofmann et al. 2008; Wagner et al. 2007; Huber and Leckie 2011; Trabucho Alexandre et al. 2011; McAnena et al. 2013; Peybernes et al. 2013; Coccioni, 2015).

This sub–event of the OAE 1b is accompanied by a negative excursion in marine carbonate carbon isotope composition (~1.5‰). This almost instantaneous warming was preceded in the late Aptian by cooler conditions (i.e., the late Aptian cold snap of Mutterlose et al. 2009; Bottini et al. 2014; Coccioni, 2015). This cooling event coincided with a positive carbon isotope excursion (CIE) of approximately 2‰ in the carbonates potentially triggered by disruptions to marine ecosystems and carbon biogeochemical cycles during the late Aptian to early Albian interval (McAnena et al. 2013; Matsumoto, 2020). This may have been triggered by large–scale volcanism in the southern Indian Ocean that is associated with the emplacement of the Kerguelen Plateau Large Igneous Province (LIP) during ~119–110 Ma in the late Aptian (Frey et al. 2003).

Third sub-event: Monte Nerone Level

This interval is characterized by alternating layers of black shales, marlstones, and limestone. TOC levels during OAE 1b vary, with black shales showing values generally less than 1%, indicating relatively low organic carbon preservation compared to other OAE events. However, the Poggio le Guaine section in the Umbria-Marche Basin reveals that specific black shale levels, such as the Jacob and Urbino/Paquier levels, experienced enhanced organic carbon accumulation rates due to increased surface productivity and reduced bottom-water ventilation (Sabatino et al., 2015).

Fourth sub-event: Urbino/Paquier

The Urbino level, the organic-rich expression of the third sub-event of OAE 1b, is documented in the western Tethys, the western North Atlantic and in Mexico (Bréhéret 1983; 1994; Tribovillard and Gorin 1991; Bralower et al. 1999; Erbacher et al. 1999; 2001; Herrle et al. 2003B; 2004; Tsikos et al. 2004; Wagner et al. 2008; Trabucho Alexandre et al. 2011; Coccioni, 2015). It was formed under increasing surface water productivity and enhanced preservation of organic matter on the sea floor linked to the early Albian Sea level rise (e.g., Herrle et al. 2004; Friedrich et al. 2005; Browning and Watkins 2008; Wagner et al. 2008; Huber and Leckie 2011; Huber et al. 2011; Trabucho Alexandre et al. 2011; Coccioni, 2015).

This sub-event of the OAE 1b is defined by a negative excursion of ~1.5‰ in marine carbonate carbon isotope records (Coccioni, et al. 2015) that can be significantly different between basins or when measured in different (in)organic compounds due to different paleoceanographical settings, variations in the source of organic matter or diagenetic effects (e.g., Bralower et al. 1999; Erbacher et al. 2001; Kuypers et al. 2002; Herrle et al. 2004; Tsikos et al. 2004).

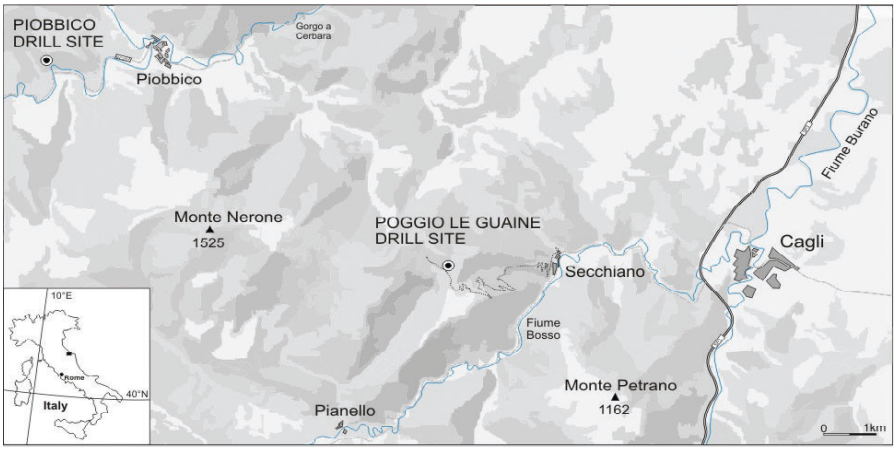

Fig.9a - Location of the Poggio le Guaine drill site in the Umbria-Marche Basin (northern Apennines, central Italy). The location of the Piobbico drill site—where an 84-m-thick core extending from the upper Albian down to the uppermost Barremian was drilled in 1982—is also shown (Coccioni, 2012)

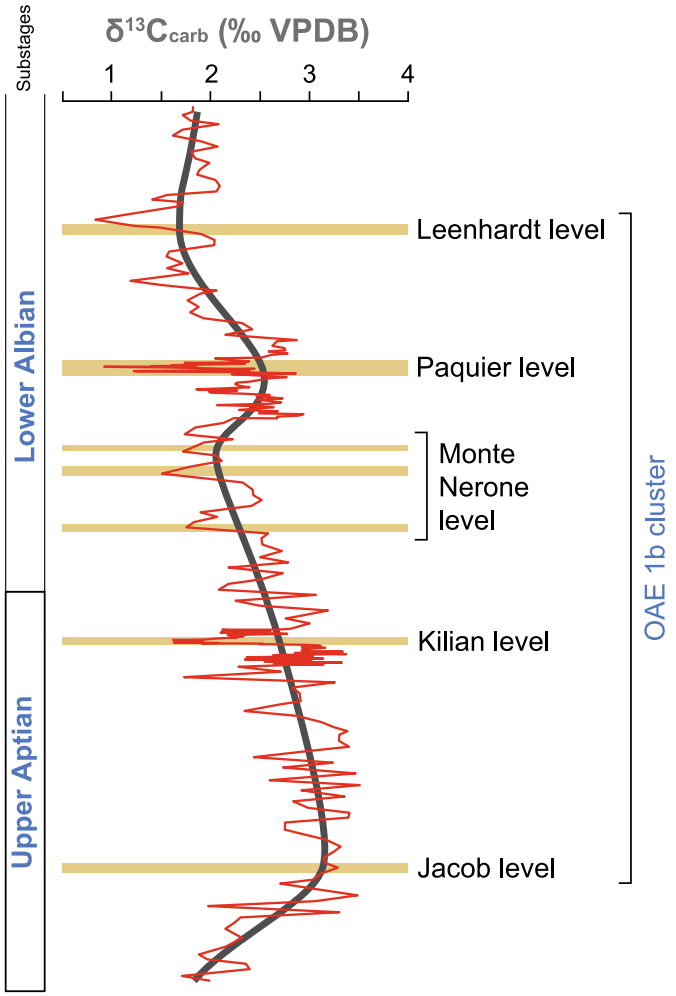

Fig.9b - Position of the OAE 1b sub-events in the Vocontian Basin after Bodin, (2023). Reference high-resolution δ13C curve for the OAE 1b cluster derived from bulk carbonate (Herrle et al., 2004).

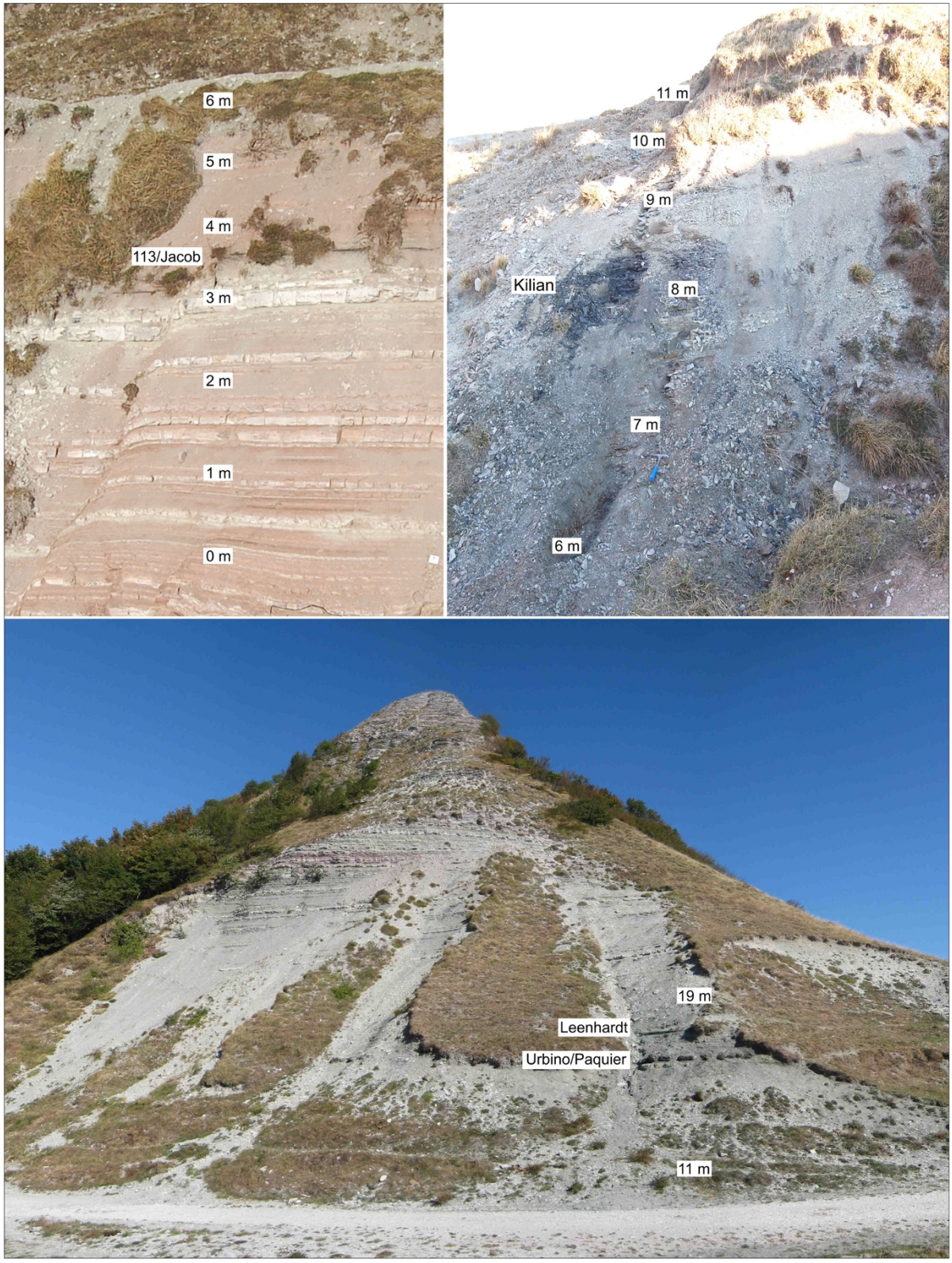

Fig. 10 - Poggio Le Guaine (Italy) in outcrop. The location of the black shale horizons as sedimentary expressions of the 4 sub-events of OAE 1b is highlighted (Coccioni et al., 2014)

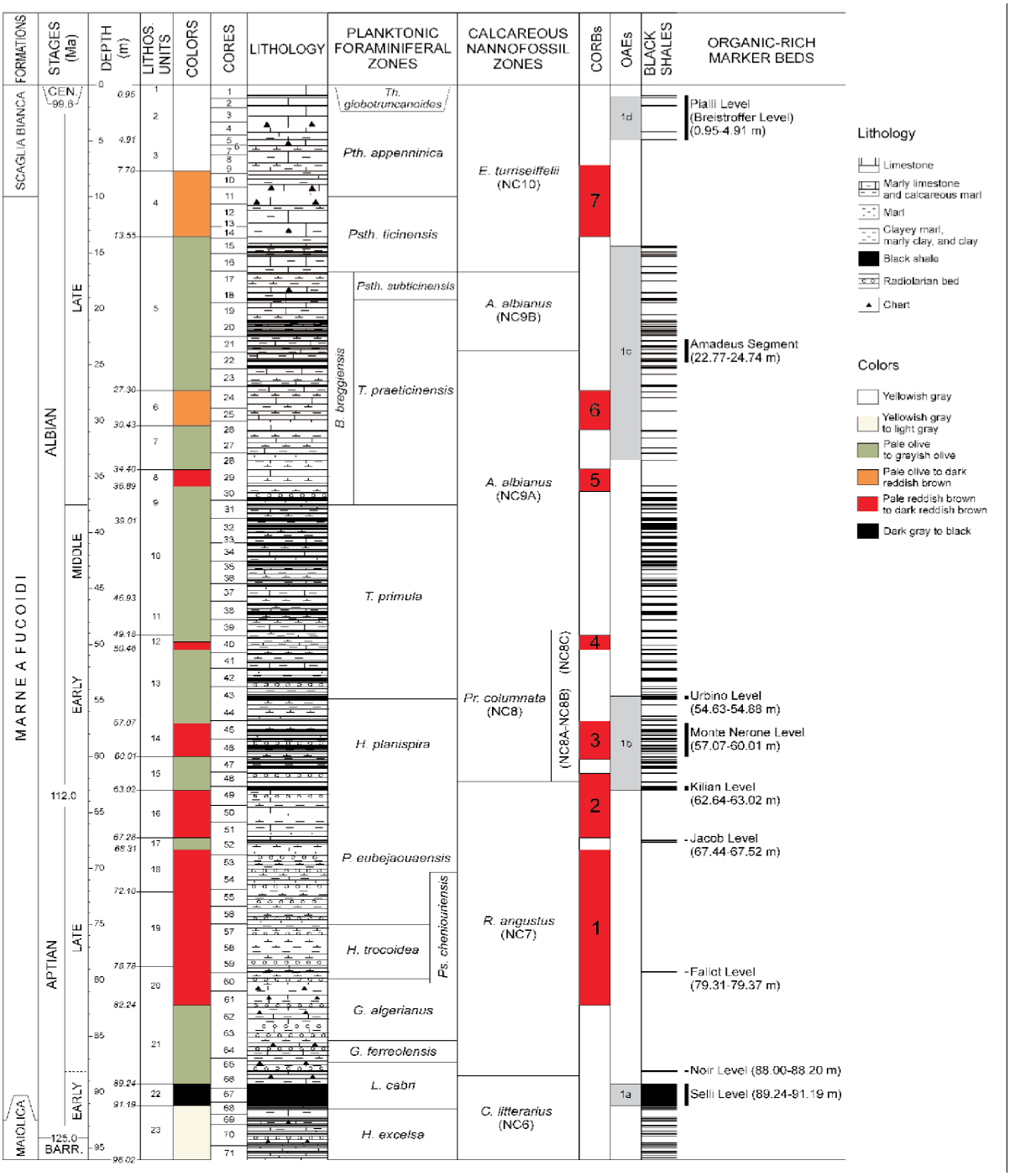

Fig. 11 -. Stratigraphic framework of the Poggio le Guaine core drilled in September 2010 with real stratigraphic depths according to bed dip measurements. Also shown are the occurrence and distribution of the organic-rich black shales including the marker beds resulting from Oceanic Anoxic Events (OAEs) and the discrete intervals where reddish colored beds become dominant (Cretaceous Oceanic Red Beds) (Coccioni et al., 2014). The 4 horizons of *OAE* 1b in this study 113/Jacob, Killian, Monte Nerone and Urbino/Paquier.

CHAPTER 4 | Methodology

4.1. | Carbon Isotope Composition ($\delta^{13}C$)

Carbonate stable carbon ($\delta^{13}C_{carb}$) and oxygen isotopic compositions ($\delta^{18}O_{carb}$) were measured in 62 samples from the PLG section using a *Gas Bench* II apparatus accopled to a Delta V Plus mass spectrometer at the Geochronology Laboratory of University of Brasília.
The samples reacted with H_3PO_4 at a temperature of 72 °C after flushing automatically the flask with helium at a flow rate of 100mL/min using a specialized double-hole needle penetrating the septa to remove air and vapor from the vials.
Stable isotope results are expressed in delta notation as per-mil variations relative to the Vienna Pee Dee Belemnite reference standard (V-PDB) (eq.5) and were calibrated against NBS 18 (δ^{13}CV-PDB = −5.01‰ and δ^{18}OV-PDB = −23.2‰) and NBS 19 (δ^{13}CV-PDB = 1.95‰ and δ^{18}OV-PDB = −2.20‰) standards. Repeated analyses of the NBS 18 standard gave −5.32‰ ± 0.09 for δ^{13}C and − 23.68 ± 0.1 for δ^{18}O (SD, n = 40) close to the recommended value. Linear regression of the standard results followed by correction of the samples data were made to account for instrumental bias. Data uncertainty (SD) varies from ±0.01‰ to ±0.28‰ for δ^{13}C and from ±0.01‰ to ±0.12‰ for δ^{18}O.

(Eq.5)

$$\delta C^{13} = \frac{R_{sample} - R_{standard}}{R_{standard}} \times 1000\ ‰$$

Analytical errors (1σ) on $\delta^{13}C_{carb}$ and $\delta^{18}O_{carb}$ were estimated to be within 0.05‰ and 0.1‰, respectively based on repeated measurements of in-house and international standard materials. The two in-house laboratory carbonate reference materials (standard materials) employed in the study were CABRA 1 and BSB 1, plus the international standards NBS-18, NBS-19 and CO-9.

4.2. | Neodymium Isotope Composition (εNd)

Twenty-one Aptian-Albian black shales rocks were sampled from cores recovered at PLG core in a length of approximately 16 meters (stratigraphic level from 67.46m of Jacob to 51.42m).

First, the samples were prepared by using the *Sequential Leaching* methodology. Neodymium isotope compositions were analyzed by inductively coupled plasma mass spectrometry (ICP-MS) at the Stable Isotopes Laboratory of Geochronology (University of Brasilia). Some samples had not enough concentration after the *Sequential Leaching* (they are: 54.85m – Urbino, 57.15m and 59.48m – Monte Nerone, 60.30m, 60.96m). All the samples are described in table 1, including the ones from the *Pialli* Level (1.46m, 2.22m and 4.88m) which was not considered further in this study (OAE 1d).

The measured $^{143}Nd/^{144}Nd$ ratios were corrected for instrumental mass bias using $^{146}Nd/^{144}Nd = 0.7219$ and an exponential fractionation law. All $^{143}Nd/^{144}Nd$ ratios were normalized to the accepted value of 0.512115 of the JNdi-1 and $BHVO_2$ and are expressed in the e-notation normalized to the value of the Chondritic Uniform Reservoir (CHUR):

(Eq.6). $eNd = [(^{143}Nd/^{144}Nd)\ sample / (^{143}Nd/^{144}Nd)\ CHUR - 1] \times 10{,}000.$

\

The accepted value of CHUR is 0.512638 (Jacobsen and Wasserburg, 1980). The analytical error of each sample analysis is taken as the external reproducibility (2r) of the JM in house standard for each analytical session

4.2.2 | Sequential Leaching Technique

The sample preparation and analysis were conducted in two stages. Initially, the samples were weighed and pulverized at the Geochronology Laboratory University of Brasília. Subsequently, sequential extraction was performed at the Geochemistry Laboratory, UnB Geosciences Institute, utilizing 50ml Falcon tubes, acetic acid (A.A.), hydrogen peroxide (H_2O_2), and Milli-Q water. The separation of the Nd from the sediment leachates and the dissolved residual detritus was conducted following the procedures and methodology of Bayon et al. (2002).

Each sample was finely crushed in an agate mortar. About 1g of the crushed sediment were placed into 50-ml centrifuge tubes for sequential leaching to remove the non-terrigenous sedimentary components.

Two different solutions composed of 5% acetic acid, 15% and 10% MQ H_20 (H_2O_2, 5%) were then added to remove the carbonates, Fe- Mn oxides and organic carbon, respectively.

After the removal of non-terrigenous components, the residual fractions were cleaned with ultrapure water (MQ-H_2O, 18 MΩ). Clayey (<2 μm) and silty (2-63 μm) fractions were then separated by centrifugation in two steps. First, 25 ml of MQ-H_2O were added to the detrital residues in the tubes, shaken vigorously in orbital shaking for 2 hours and 30 minutes and then centrifuged for 20 min at 2000 rpm. The clay-rich supernatants were immediately transferred into new 50 ml centrifuge tubes.

Another 10 ml of MQ H_2O and 10 ml of 2/3 H_2O_2 (peroxide) was added to silt-rich detrital residues, mixed thoroughly again for 48 hours (with intermittent interruptions to relieve pressure in the tubes) centrifuged for 20min at 3.000 rpm, and transferred into corresponding centrifuge tubes.

Finally, clay-size fractions were collected after decantation (48 hours) and centrifugation at 3500 rpm.

The following Table 2 synthetize the whole process.

Sequential Leaching procedures modified after Bayon, 2002

SEQUENCIAL LEACHING (BAYON, 2002)

o Removal of Carbonates
- Add 10 ml of 10% Acetic Acid (CH_3COOH) [+10 ml of MQ H2O = A.A 5%]
- Shake well to mix the solution
- Put in the shaking table for 2-3 hours with the lids half-closed
- Weight (each pair must have no more than 0.1g difference in weight, if it's too different correct it with MQ H2O)
- Centrifuge @2000rpm for 2 minutes
- Throw away supernatants

o Removal of Organic Carbon
- Add 10 ml MQ H2O
- Add 10 ml 2/3 H2O2
- Put in the shaking table for 48 hours with the lids half-closed. Sometimes, depending on the quantity of organic matter, it should stay longer.
- Weight
- Centrifuge @2500 rpm for 2 minutes
- Throw away supernatant
- Add 5 ml of MQ H2O
- Weight
- Shake well
- Centrifuge @3000 rpm for 2 minutes
- Throw away supernatant.

o Clay Separation
- Add 20 ml of MQ H2O
- Weight
- Shake well
- Centrifuge @1000 rpm for 2 minutes
- Transfer clays into clean tubes (cleaned with MQ H2O)
- Add 20ml of MQ H2O into the with residue
- Weight
- Shake well
- Centrifuge @800 rpm for 2:30 minutes
- Transfer clays into the clay tubes
- Add 1ml of concentrated A.A into the clay tubes
- Weight
- Centrifuge @3500 rpm for 3 minutes. If after the first run the solution still is cloudy, run it again
- Throw away supernatant.

By this point the clays are separated from the silt size fraction. Afterwards its necessary to "rinse" the leftover silt size fraction and centrifuge it again to get rid of remaining clays.

- On the residue add 20 ml MQ H2O
- Weight
- Shake well
- Centrifuge @800 rpm for 2:30 minutes

4.3 | **Fieldwork**

A 15-day fieldwork was carried out in the city of Urbino, Marche region of Central Italy, with the professor Jairo Savian, and PhD students of geopaleomagnetism from Federal University of Rio Grande do Sul, Brazil (UFRGS), Carolina Goncalves Leandro and Raquel Gewehr de Mello.

The XRF data were all collected straightly from the Italian cores handed by the University of Urbino under the supervision of Prof. Fabrizio Frontalini.

The other samples were recovered from the PLG core and provided by. Prof. Jairo Savian, who is also coordinator of the project "Processing and interpretation of magnetostratigraphic data from the Cretaceous of the Brazilian Basins", sponsored by the Support Foundation of the Federal University of Rio Grande do Sul and PETROBRAS.

The samples investigated in this study are from the Poggio Le Guaine core and they were recovered in 2012 near the city of Urbino, Central Italy. The core has a total length of 95 meters and comprises the entire Marne a Fucoidi Formation and its upper and lower boundaries. The data acquisition was made at the Geochemistry Laboratory of the Università Degli Studi di Urbino, Urbino, Italy, April 2022. There were 10 days of collections in approximately 34 meters of this section - from 35.98 m to 69.90 m – in a total of 647 measurements with a high-resolution investigation and an average resolution of a sample every 3 cm along the PLG core. (Fig.7)

The analyses were performed directly on the core, targeting flat areas wherever possible, avoiding the proximity of the XRF device to reduce the exposure to radiation emissions. Calibration was performed every 4 measurements. The instrument was configured to yield the most reliable results possible, with each sample undergoing 5 replicate measurements to generate a mean value. Outliers resulting from analytical issues or core surface alterations were identified and removed from the dataset to maintain data integrity.

The main elements detected were K, Ca, Mn, Fe, Al, Si, Sr, Zr, Ti, V, Ni, P, Mo, Cu, V, Sb and Sn. Additional elements were present below the detection limit. To facilitate comparison, the acquired data were normalized to the mean and standard deviation using the following equation:

$$\text{Normalization} = \frac{(x - \text{mean}(x))}{(\text{pad deviation}(x))} \quad \text{(Eq.7)}$$

Where, x = elementary value.

CHAPTER 5 | Results - Scientific Paper

Short-term paleoceanographic changes across the Oceanic Anoxic Event (OAE) 1b in the Aptian-Albian PLG core (Umbria Marche Basin, Italy)

ABSTRACT

Oceanic Anoxic Events (OAEs) have profoundly impacted Earth's climate and paleoceanography, particularly through disruptions to the global carbon cycle. During the *OAE* 1b, reduced circulation intensity and increased nutrient influx led to enhanced primary productivity and oxygen consumption in the water column, creating anoxic conditions, which led to widespread deposition of black shales. The *Poggio Le Guaine* (PLG) section in Central Italy's Umbria-Marche Basin provides a well-preserved record of this event, with a pelagic sequence of black shales and calcareous sediments. This section encompasses four sub-events within the OAE 1b interval, characterized by organic matter-rich levels that can be correlated regionally and globally. Despite numerous studies on OAE 1b, uncertainties remain regarding the environmental and palaeoceanographic changes that occurred during the Aptian-Albian period. This study presents a high-resolution, multi-proxy analysis of the PLG section, integrating $\delta^{13}C$, εNd in clay material, and geochemical elemental analysis to reconstruct the paleoenvironmental and sedimentary dynamics of OAE 1b period. Our results reveal a relatively homogeneous sediment provenance during the whole period, with exceptions at the Killian, Monte Nerone, and Urbino levels, which exhibit excursions in $\delta^{13}C$, εNd values, accompanied by increases in terrigenous input. Despite the instability, OAE 1b stands out as a distinct event, differing significantly from OAE 1a and 2. Its exceptional nature is characterized by a prolonged duration, extremely unstable climatic conditions, and several unique features. Notably, OAE 1b lacks the extreme carbon cycle disruptions, classical positive geochemical excursions, and significant changes in oceanic circulation, sediment supply, or environmental conditions that are typically associated with other OAEs.

keywords: Isotopic geochemistry; Neodymium isotopes, Elemental geochemistry, Portable XRF, Principal Components Analysis, Oceanic Anoxic Event 1b

5.1 | Introduction

Oceanic Anoxic Events (OAEs) represent significant disruptions to the global carbon cycle, resulting in widespread burial of organic matter in oceanic sediments and profound climate changes (Schlanger and Jenkyns, 1976; Jenkyns, 2010). These events have been linked to substantial fluctuations in atmospheric CO_2 levels, potentially driving climate warming. Furthermore, the preservation of organic matter in anoxic sediments can affect the carbon cycle and influence long-term climate patterns (Wagner et al., 2004; Weissert & Erba, 2004).

The study of Oceanic Anoxic Events (OAEs) began in the 1970s through the DSDP (Deep Sea Drilling Project), a geoscientific research program aimed to map and explore the ocean floor. Initial observations revealed that certain black shale-rich intervals in pelagic successions were synchronous and globally distributed, occurring in the Pacific, Atlantic, and European regions. Initially, two Oceanic Anoxic Events were identified: the *Aptian-Albian OAE,* or *OAE 1,* and the *Cenomanian OAE,* or *OAE 2*. During both events, oceanic conditions favored the deposition of sediments enriched in organic matter. Further research led to the discovery of two additional, minor OAEs: OAE 1b and OAE 1d (fig.1). More OAEs were identified also in other periods, such as the Coniacian-Santonian (OAE 3; e.g. Mansour & Wagreich, 2022) and the Toarcian (T-OAE; Jenkyns, 1988).

Large-scale volcanic episodes, particularly from Large Igneous Provinces (LIPs) are considered the main forcing of the OAEs. The intense volcanic activity released significant amounts of CO_2, which led to global warming. This warming accelerated the hydrological cycle, increasing nutrient runoff into oceans, which fueled marine productivity and oxygen consumption at depth (Jenkyns, 2010), (Kuroda et al., 2007). Higher nutrient availability from increased weathering and runoff promoted phytoplankton growth. As organic material sank and decomposed, it consumed available oxygen, resulting in widespread anoxia, particularly in restricted basins like the Western Interior Seaway during the Cretaceous (Adams et al., 2010), (Monteiro et al., 2012). However, other possible causes have also been proposed, such as orbital forcing (e.g. Mitchell et al., 2008; Batenburg et al., 2016).

5.1.2 | Oceanic Anoxic Event - OAE 1b

The Aptian-Albian OAE 1b is the longest-lasting of the cretaceous Oceanic Anoxic Events (OAEs). Based on studies by Grippo et al. (2004) and Huang et al. (2010), Coccioni et al. (2014;2015) estimated its total duration at approximately 3.8 million years. More recently, Ramos et al (2024) estimates a new timespan of around 2.84 Myr.

In the Marne a Fucoidi Formation of the Umbria Marche Basin, in Central Italy, the OAE 1b was initially associated just to the Urbino/Paquier level, a black shale interval of regional extent (Bralower et al., 1993; Herrle et al., 2004; Jenkyns, 2010). However, the current definition of the OAE 1b encompasses a broader interval of five black shale horizons within the Aptian-Albian boundary, which are in stratigraphic order: Jacob, Kilian, Monte Nerone, Urbino/Paquier, and Leenhardt levels. These horizons are associated with short-term perturbations in the carbon cycle and climate (Arthur and Premoli Silva, 1982; Bréhéret et al., 1986; Bréhéret and Delamette, 1987, 1989; Bréhéret, 1988, 1994, 1997; Premoli Silva and Sliter, 1999; Leckie et al., 2002; Huber and Leckie, 2011; Sabatino et al., 2015; Bodin et al., 2023).

The Monte Nerone level has been correlated with either the Kilian or Paquier levels of the Vocontian Trough, in SE France (e.g., Erbacher, 1994; Leckie et al., 2002; Trabucho Alexandre et al., 2011; Petrizzo et al., 2012; Bodin et al., 2023). Recently, it has been recognized as a fifth organic matter-rich level comprised between the Kilian and Paquier levels (Coccioni et al., 2014). These multiple events would be associated with intervals of cooling and sea level fall in the late Aptian, followed by subsequent sea level rise and global warming during the early Albian (Leckie et al., 2002). The $\delta^{13}C$ isotope curve marks a breakpoint between these periods, characterized by a positive excursion at the end of the Aptian followed by a pronounced negative shift at the beginning of the Albian (Weissert and Lini, 1991; Herrle et al., 2004). This period is interpreted as the result of a combination of major geological and climatic factors, including: (1) extremely hot and uniform global climate, which reduced ocean water mixing and oxygenation; and (2) the occurrence of large volcanic provinces (or Large Igneous Provinces, *LIP*), which caused climate and carbon cycle disturbances (Turgeon & Creaser, 2008; Tejada et al., 2009; Jenkyns, 2010).

To better understand the extent of the palaeoceanographic mechanisms acting during the *OAE* 1b and the Late-Aptian to the Early-Albian time in the Umbria-Marche basin, we present a multiproxy dataset of the OAE 1b interval of the PLG core. These findings highlight how geochemical elements record the oceanic processes during the mid-Cretaceous.

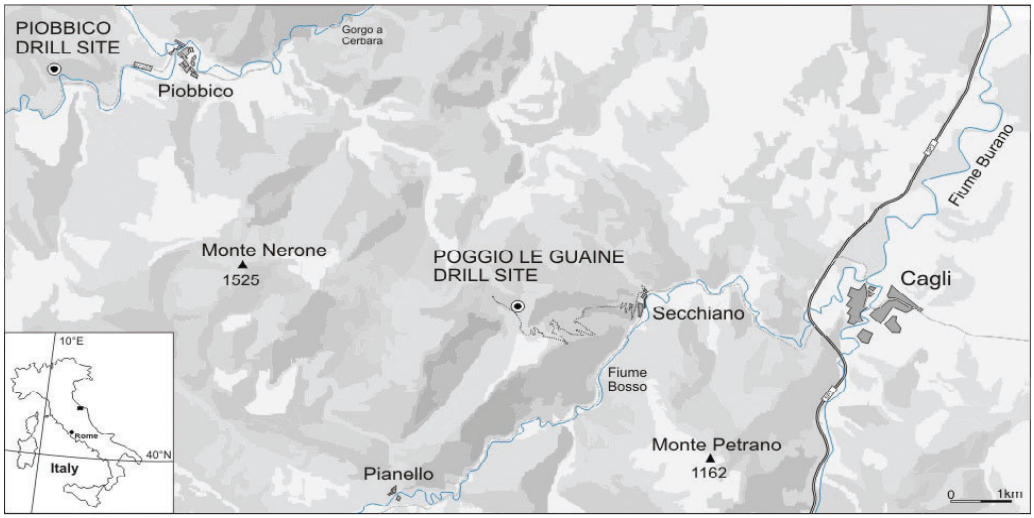

Fig. 12 - Location of the Poggio le Guaine drill site in the Umbria-Marche Basin (northern Apennines, central Italy). The location of the Piobbico drill site—where an 84-m-thick core extending from the upper Albian down to the uppermost Barremian was drilled in 1982—is also shown (Coccioni, 2012)

5.1 | Geological and stratigraphic Setting

5.1.2 Umbria-Marche Basin

The Umbria-Marche Basin (UMB) is situated in the central part of Italy and is recognized as a reference succession for oceanic anoxic events. It outcrops in the Italian Apennines, forming the southern sector of the Northern Apennines, part of the peri- Mediterranean system of Alpine chains formed by differential movements between Africa and Europe plate. The region has undergone at least three major tectonic phases: (1) a Mesozoic extensional phase, (2) a Neogene compressional phase, and (3) a Late Miocene to Pleistocene extensional phase, confined to the Umbria sector (Menichetti & Coccioni 2015).

5.2.3 PLG (Poggio le Guaine Section)

The Poggio Le Guaine (PLG) drill core encompasses the sedimentary record of OAEs 1a, 1b, and 1d (Coccioni et al., 2012), spanning from the upper Maiolica Formation (Tithonian to lower Aptian) to the lower Scaglia Bianca Formation (upper Albian to lower Turonian), with the Marne a Fucoidi Formation in between.

Within this pelagic succession, the sedimentary expression of the OAE 1b consists of pale reddish-brown to dark reddish-brown and pale olive to greyish-olive argillaceous limestones and calcareous marlstones, as well as slightly calcareous to argillaceous mudstones. These deposits include several cyclically alternating organic-rich black shales and mudstones, some of which have been identified as regional to global sedimentary markers of OAE 1b (Coccioni et al., 2014; Leckie et al., 2002; Trabucho Alexandre et al., 2011). The succession was deposited at a paleolatitude of approximately 20°N, based on reconstructions from the Ocean Drilling Stratigraphic Network Plate Tectonic Reconstruction Service (http://www.odsn.de), and at middle to lower bathyal depths (about 1000–1500 m) in a relatively stable pelagic environment, above the calcite compensation depth (Coccioni, 1990; Coccioni et al., 2014).

Several organic-rich horizons within the PLG core represent the regional expression of the global OAE 1b event (Coccioni, 1996; Coccioni et al., 1990, 2012, 2014; Leckie et al., 2002; Matsumoto et al., 2020, 2022; Petrizzo et al., 2012; Sabatino et al., 2015, 2018; Trabucho Alexandre et al., 2011; Bodin et al., 2022). These include the upper Aptian 113/Jacob level, the lowermost Albian Kilian level, the Albian Monte Nerone cluster, the Albian Urbino/Paquier level, and the Albian Leenhardt organic-rich marker beds (Coccioni et al., 2014; Matsumoto et al., 2020, 2022; Sabatino et al., 2015, 2018). This study presents new data from the Jacob to Urbino levels.

The investigation of the Aptian-Albian continuous and undisturbed pelagic section at *Poggio le Guaine*, provides a unique chance to produce a high-resolution overview of the palaeoceanographic changes in Tethys during the *OAE* 1b.

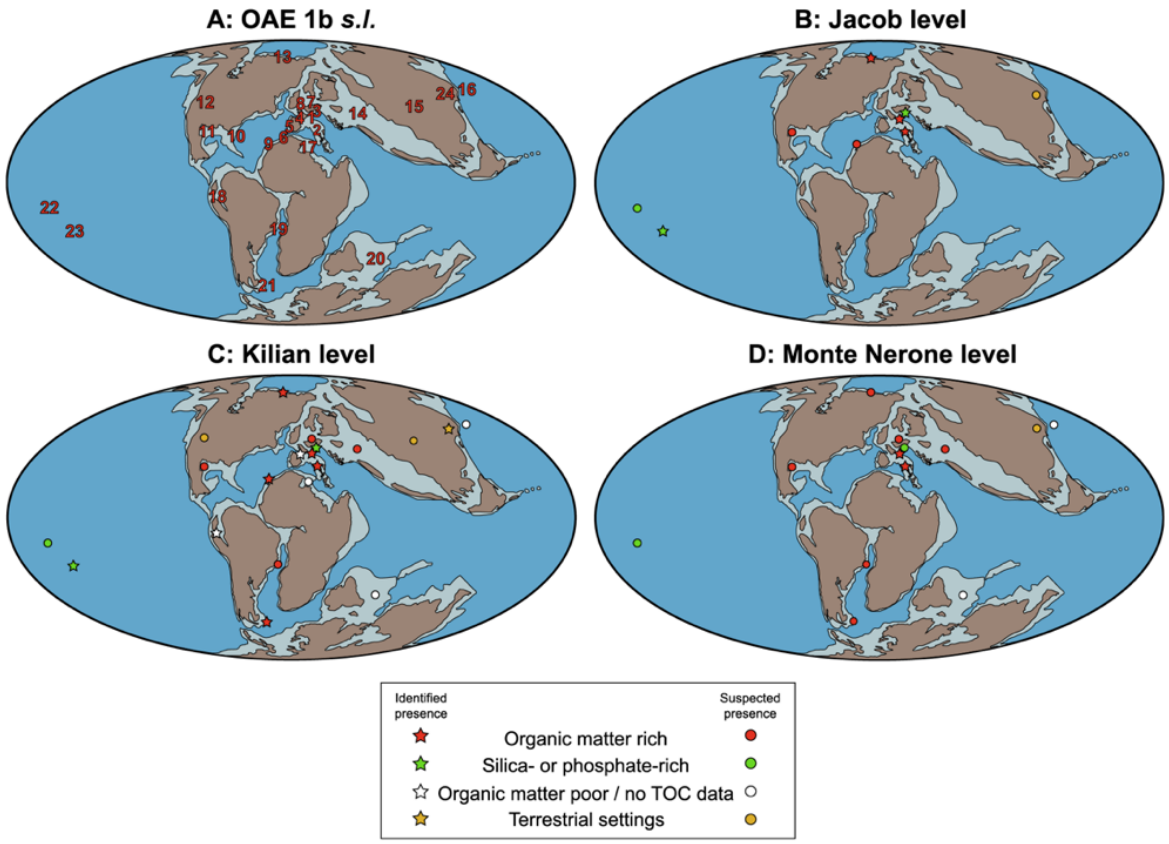

Fig. 13 - Paleogeographic distribution of OAE 1b records. Early Albian paleogeographic map modified after Bodin (2023) A. Localities spanning the Aptian-Albian transition where lithological, geochemical, or paleontological evidences relates to the OAE 1b sensu *lato*. 1. Vocontian Basin, France (Br´eh´eret and Crumi`ere, 1989; Herrle et al., 2004). 2. Umbria-Marche Basin, Italy (Coccioni et al., 2014). 3. Helvetic shelf and Briançonnais Domain, Switzerland (Strasser et al., 2001; Fo˙llmi et al., 2007). 4. Basque–Cantabrian Basin, Spain (Milla´n et al., 2014). 5. Algarve Basin, Portugal (Heimhofer et al., 2003). 6. Essaouira-Agadir Basin, Morocco (Peybernes et al., 2013). 7. Lower Saxony Basin, Germany (Mutterlose et al., 2003). 8. Wessex Basin, England (Grocke, 2002). 9. DSDP site 545, Mazagan Plateau, eastern Proto- North Atlantic (Wagner et al., 2008; Huber and Leckie, 2011; McAnena et al., 2013). 10. ODP site 1049, Blake Plateau, western Proto-North Atlantic (Erbacher et al., 2001; Huber and Leckie, 2011). 11. Northern Cordillera, Mexico, and Comanche Platform, Texas (Bralower et al., 1999; Phelps et al., 2015). 12. Western Interior, Utah (Ludvigson et al., 2015). 13. Axel Heiberg Island, Canada (Herrle et al., 2015). 14. Northeastern peri-Tethys, Caucasus region (Gavrilov et al., 2019). 15. Yujingzi Basin, northwest China (Suarez et al., 2018). 16. Hokkaido, Japan (Ando and Kakegawa, 2007). 17. Tunisian Platform, Tunisia (Ben Chaabane et al., 2019). 18. Western Platform, Peru (Navarro-Ramirez et al., 2015). 19. Central Proto-South Atlantic, Brazil (Caetano-Filho et al., 2017). 20. Southern Tibet, China (Li et al., 2016). 21. DSDP Site 511, Falkland Plateau, southern South Atlantic (Huber and Leckie, 2011; Huber et al., 2018; Matsumoto et al., 2023). 22. ODP sites 1207 and 1213, Shatsky Rise, northwest Pacific (Robinson et al., 2004). 23. DSDP site 463, Resolution Guyot, Mid-Pacific Mountains (Price, 2003; Matsumoto et al., 2020). 24. Fuxin Basin, Northeast China (Xu et al., 2022). B– F. For each OAE 1b sub-levels, map showing the localities where their presence can be identified (star) or suspected (circle), as well as the type of lithological expression.

5.4 | Material and Methods

5.4.1 Carbon and oxygen isotopes analysis

Carbonate carbon ($\delta^{13}C_{carb}$) and oxygen ($\delta^{18}O_{carb}$) stable isotopic compositions were measured in 62 samples from the PLG Core section using a *Gas Bench* II apparatus coupled to a Delta V Plus mass spectrometer at the Geochronology Laboratory of University of Brasília. Additional 28 samples were measured previously in the Stable Isotopes Laboratory at the PETROBRAS/CENPES.

The samples reacted with H_3PO_4 at a temperature of 72°C after flushing automatically the flask with helium at a flow rate of 100mL/min using a specialized double-hole needle penetrating the septa to remove air and vapor from the vials.

Stable isotope results are expressed in delta notation as per-mil variations relative to the Vienna Pee Dee Belemnite reference standard (V-PDB) and were calibrated against NBS 18 ($\delta^{13}C$ V-PDB = −5.01‰ and $\delta^{18}O$ V-PDB = −23.2‰) and NBS 19 ($\delta^{13}C$ V-PDB = 1.95‰ and $\delta^{18}O$ V-PDB = −2.20‰) standards. Repeated analyses of the NBS 18 standard gave −5.32‰ ± 0.09 for $\delta^{13}C$ and − 23.68 ± 0.1 for $\delta^{18}O$ (SD, n = 40) close to the recommended value. Linear regression of the standard results followed by correction of the samples data were made to account for instrumental bias. Data uncertainty (SD) varies from ±0.01‰ to ±0.28‰ for $\delta^{13}C$ and from ±0.01‰ to ±0.12‰ for $\delta^{18}O$. Analytical errors (1σ) on $\delta^{13}C_{carb}$ and $\delta^{18}O_{carb}$ were estimated to be within 0.05‰ and 0.1‰, respectively based on repeated measurements of in-house and international standard materials. The two in-house laboratory carbonate reference materials (standard materials) employed in the study were CABRA 1 and BSB 1, plus the international standards NBS-18, NBS-19 and CO-9

5.4.2 Nd isotope analysis

Twenty-one Aptian-Albian black shales rocks were sampled from cores recovered at PLG core in a length of approximately 16 meters (stratigraphic level from 67.46m of Jacob to 51.42m). First, the samples were prepared by using the *Sequential Leaching* methodology. Neodymium isotope compositions were analyzed by inductively coupled plasma mass spectrometry (ICP-MS) at the Stable Isotopes Laboratory of Geochronology (University of Brasilia). Some samples had not enough concentration after the *Sequential Leaching* (they are: 54.85m – Urbino, 57.15m and 59.48m – Monte Nerone, 60.30m, 60.96m). All the samples are

described in table 1, including the ones from the *Pialli* Level (1.46m, 2.22m and 4.88m) which was not considered further in this study (OAE 1d).

The measured $^{143}Nd/^{144}Nd$ ratios were corrected for instrumental mass bias using $^{146}Nd/^{144}Nd = 0.7219$ and an exponential fractionation law. All $^{143}Nd/^{144}Nd$ ratios were normalized to the accepted value of 0.512115 of the JNdi-1 and BHVO2 and are expressed in the e-notation normalized to the value of the Chondritic Uniform Reservoir (CHUR): $\varepsilon Nd = [(^{143}Nd/^{144}Nd)\ sample/\ (^{143}Nd/^{144}Nd)\ CHUR - 1] \times 10^4$. The accepted value of CHUR is 0.512638 (Jacobsen and Wasserburg, 1980). The analytical error associated with each sample analysis was estimated based on the external reproducibility (2σ) of the in-house standard (JM) for each analytical session, as described by Yannick et al. (2017).

5.4.3 XRF Chemical Analysis

Elemental concentrations of Al, Si, K, Ti, Fe, V, Cd, Ca, and Mn were determined using a handheld XRF Analyzer (Olympus Delta Professional, model DPO-6000), granted by University of Brasilia.

Each spot was analyzed with five repetitions for most of the interval, except for the uppermost 2 meters, where three repetitions were applied. The acquisition time for each analysis was 60 seconds. Notably, no significant differences were observed between the data obtained with different numbers of repetitions.

The elements detected with the best precision and performed in this study were: Potassium (K), Calcium (Ca), Manganese (Mn), Iron (Fe), Aluminum (Al), Titanium (Ti), Silicon (Si), Vanadium (V) and Cadmium (Cd).

5.4.4 Principal Component Analysis (PCA)

The XRF dataset was processed and analyzed using the *PAST 4* software, to provide statistical insights into the geochemical variability throughout the study interval. The analysis was conducted based on three complementary stratigraphic approaches, aligned with lithological type and different intervals:

- Black Shale Intervals: PCA was applied to each of the four main black shale intervals (Jacob, Kilian, Monte Nerone, and Urbino) to identify their characteristic geochemical features.
- OAE 1b and Surrounding Intervals: performed on the entire OAE 1b interval (encompassing the Jacob, Killian, Monte Nerone, and Urbino levels/ 54.64 – 63.02m) and the preceding (PRE OAE 1b/63.05 – 67.41m) and succeeding (POST OAE 1b/ 36.02 – 54.61m), to investigate geochemical changes across the event.
- Color-Based Intervals: Notably, the black shales exhibited varying colors, with some intervals in red and others appearing green. Despite the unknown cause of these color differences, the geochemical data were analyzed separately for the red and green intervals to investigate potential differences in their geochemical signatures.

5.5 Results

5.5.1 Stable carbon isotope analyses ($\delta^{13}C$)

Figure 14 presents the carbonate carbon isotopic data ($\delta^{13}C_{carb}$) analyzed in this study, alongside those obtained previously by Petrobras, throughout the interval encompassing the OAE 1b in the PLG core. The $\delta^{13}C_{carb}$ values range between 2.4‰ and 3.5‰, displaying both long-term and short-term variations. The highest values occur in the lowermost part, and then general trends display a decrease of 1‰ from about 67m to 57.7m, followed by an increase of nearly 0.6‰ in the upper part of the interval, up to 50.4m. The minimum value between the two main trends occurs within the Monte Nerone level. These trends are punctuated by several short-term fluctuations with amplitudes of about 0.5‰. The Killian and Urbino levels present significative $\delta^{13}C_{carb}$ negative excursions, with amplitude of approximately 0.5‰, and 1‰, respectively. These results are consistent with previous studies of PLG sections in core and outcrop samples (Sabatino et al., 2015; Matsumoto et al., 2020).

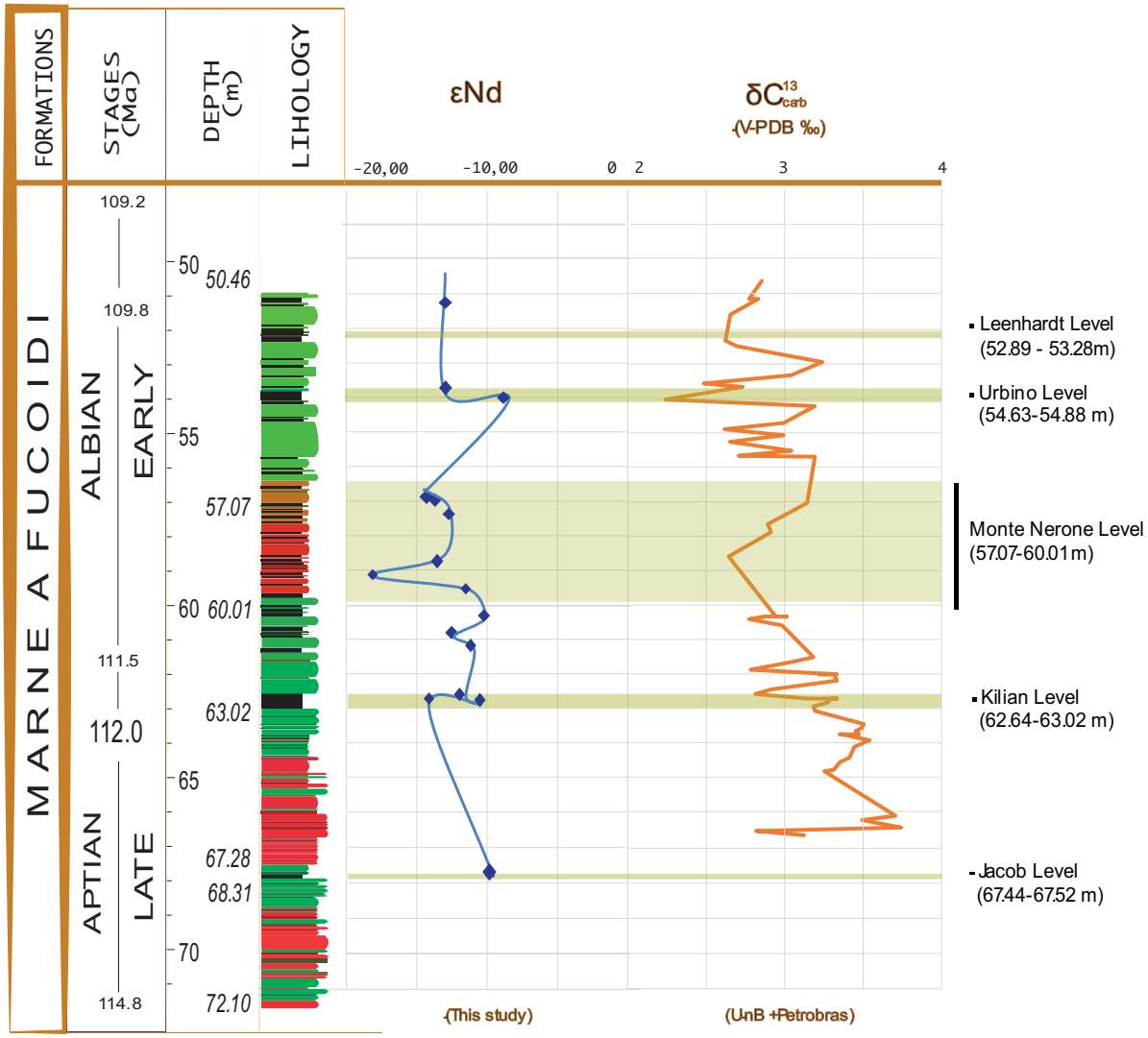

Fig. 14 - Integration of isotopic composition data of carbon $\delta^{13}C_{carb}$ from University of Brasilia (this study) and Petrobras (2012) – orange line. Neodymium isotopic composition (εNd) for the Aptian-Albian PLG interval ranging from -9 to -17 units – blue line.

5.5.2 Neodymium Isotope Results

The results of neodymium isotopic composition (εNd) in the clay fraction of black shale layers within the OAE 1b interval of the PLG core section are also shown in figure 14 and table 2. Most of the values range between -9,02 and -14.90, with an outlier of -17,96 occurring within the Monte Nerone level. In general, they do not display any significant trend within the studied interval, nor significant difference between the most prominent levels with regional significance, such as the Jacob, Kilian, and Urbino, and the minor ones. These values are consistent also with those from the Pialli level, representing the OAE 1d in the PLG core section (table 2).

Table 2: Nd isotope results of the clay fraction from various black shale layers of the PLG section. Some samples are from intervals with regional significance, such as the Jacob, Kilian, Monte Nerone, Urbino, and Pialli levels. The values of reference materials (JM, JNDI, and BHVO2) are reported to show the analytical reproducibility.

Sample	Dip Corrected (M)	Nd (ppm)	143Nd/144Nd ± 2SE	eNd (0)	Stratigraphic level
JM	-	-	0.512249+/-6	-7,59	
JM	-	-	0.512251+/-6	-7,55	
JM	-	-	0.512248+/-5	-7,61	
JM	-	-	0.512258+/-6	-7,41	
JM	-	-	0.512268+/-6	-7,22	
JNDI_20221227			0.512108+/-5	-10,35	
Nd_BHVO2_20221227		25,678	0.512987+/-8	6,81	
PLG 1,46	1,26	11,954	0.511925+/-16	-13,91	Pialli
PLG 2,22	1,92	15,551	0.512046+/-8	-11,55	Pialli
PLG 4,88	4.23	17,605	0.511874+/-30	-14,90	Pialli
PLG 53,13	51.42	21,972	0.511963+/-10	-13,16	
PLG 56,34	54.63	18,238	0.511965+/-17	-13,13	Urbino
PLG 56,47	54.76	59,337	0.512176+/-5	-9,02	Urbino
PLG 58,86	57.15	17,817	0.511906+/-11	-14,27	Urbino
PLG 58,88	57.17	20,335	0.511893+/-19	-14,54	Monte Nerone
PLG 59,40	57.68	22,026	0.511978+/-5	-12,87	Monte Nerone
PLG 60,68	58.96	21,521	0.511955+/-22	-13,32	Monte Nerone
PLG 61,17	59.46	22,991	0.511717+/-28	-17,96	Monte Nerone
PLG 61,56	59.84	19,487	0.512044+/-14	-11,59	Monte Nerone
PLG 62,30	60.58	25,392	0.512097+/-7	-10,56	Monte Nerone
PLG 62,79	61.07	19,491	0.511994+/-10	-12,56	
PLG 63,16	61.44	19,581	0.512060+/-10	-11,27	
PLG 64,31	62.88	25,191	0.512033+/-6	-11,81	
PLG 64,60	62.98	29,335	0.512080+/-7	-10,89	Killian
PLG 64,70	67.46	24,816	0.511910+/-23	-14,21	Killian
PLG 69,1		24,225	0.512124+/-7	-10,03	Jacob

5.5.3 XRF elemental data

High-precision geochemical data acquired via portable X-ray fluorescence (XRF) spectroscopy across the lower Albian interval of the PLG core are presented in Figure 16. A summary of the main statistics per each element, including average, maximum, and minimum values of the raw data, is provided in Table 3.

Table 3: Statistical data for XRF results

	MAX	Depth (m)	Lithology	Colors	MIN	Depth (m)	Lithology	Colors	AVERAGE
Al	6,19	55.58	Black Shale/ Urbino	GL3	0,41	57.02	Limestone	GL3	3,26
Si	36,41	62.84	Black Shale/ Killian	GL4	0,79	36.16	marl, clayey marl	GL4	21,21
K	62,99	56,81	Marly limestone and calcareous marl	RL2	0,24	48.66	Marly limestone and calcareous marl	GL4	12,14
Ti	0,502	55.58	Black Shale/ Urbino	GL3	5,24	48.66	Marly limestone and calcareous marl	GL4	20,36
Ca	35,41	48.66	Marly limestone and calcareous marl	GL4	0,05	55.52	Black Shale/ Urbino	GL3	0,2179
V	0,322	55.58	Black Shale/ Urbino	GL3	0,01	48.69	Marly limestone and calcareous marl	GL4	0,068
Mn	0,456	48.66	Marly limestone and calcareous marl	GL4	0,01	56.72	Marly limestone and calcareous marl	GL3	0,1572
Fe	0,322	53.14	Black Shale/ Leenhardt	GL3	0,01	37.31	Black shales, marly limestone and calcareous marl	GL4	0,068
Ni	0,243	49.32	Blach Shale, marl	GL4	0,0014	44.78	Black shales, marly limestone and calcareous marl	GL4	0,011
Cd	0,038	69.33	Marly limestone and calcareous marl	-	0	37.01	Black Shale	-	0,02

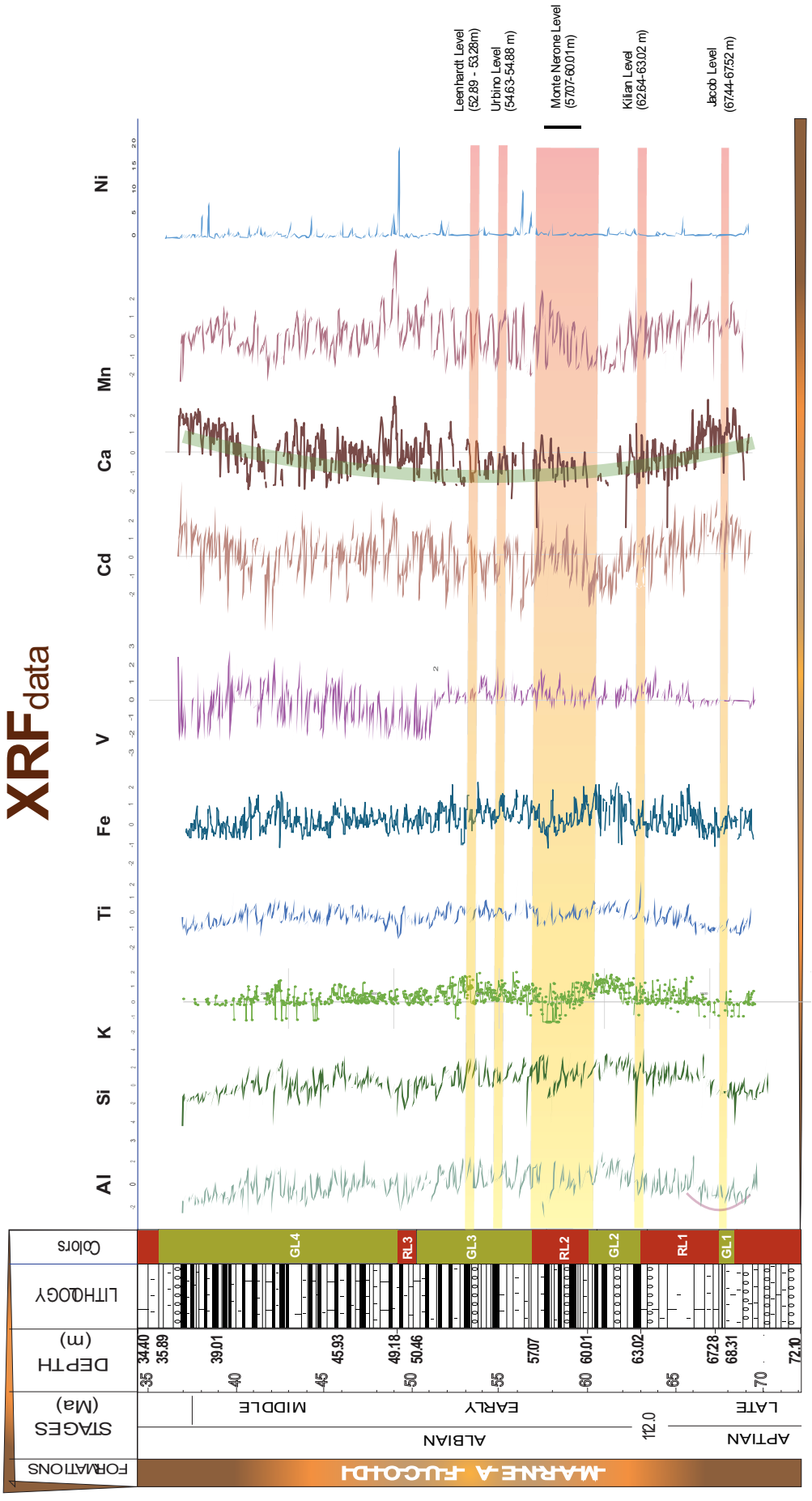

Fig 15 – XRF data (Al, Si, K, Ti, Fe, V, Cd, Ca, Mn, Ni) measured in the PLG core, correlated to the stratigraphic Marne a

To enhance model interpretability, the detected data and trends presented in the results were normalized using the pad deviation method described in Equation 7. This normalization procedure ensured that the data were scaled to a comparable range. A comprehensive analysis of the dataset revealed the presence of 28 elements, with 1089 measurements recorded for each element. The 10 elements exhibiting the highest precision are presented in this study (fig. 15), positioned within the stratigraphic framework.

A comparative analysis of the normalized and non-normalized data (fig. 16) revealed a high degree of symmetry between the two datasets. This symmetry may be attributed to the symmetric distribution of the data, the type of normalization employed, or rounding errors.

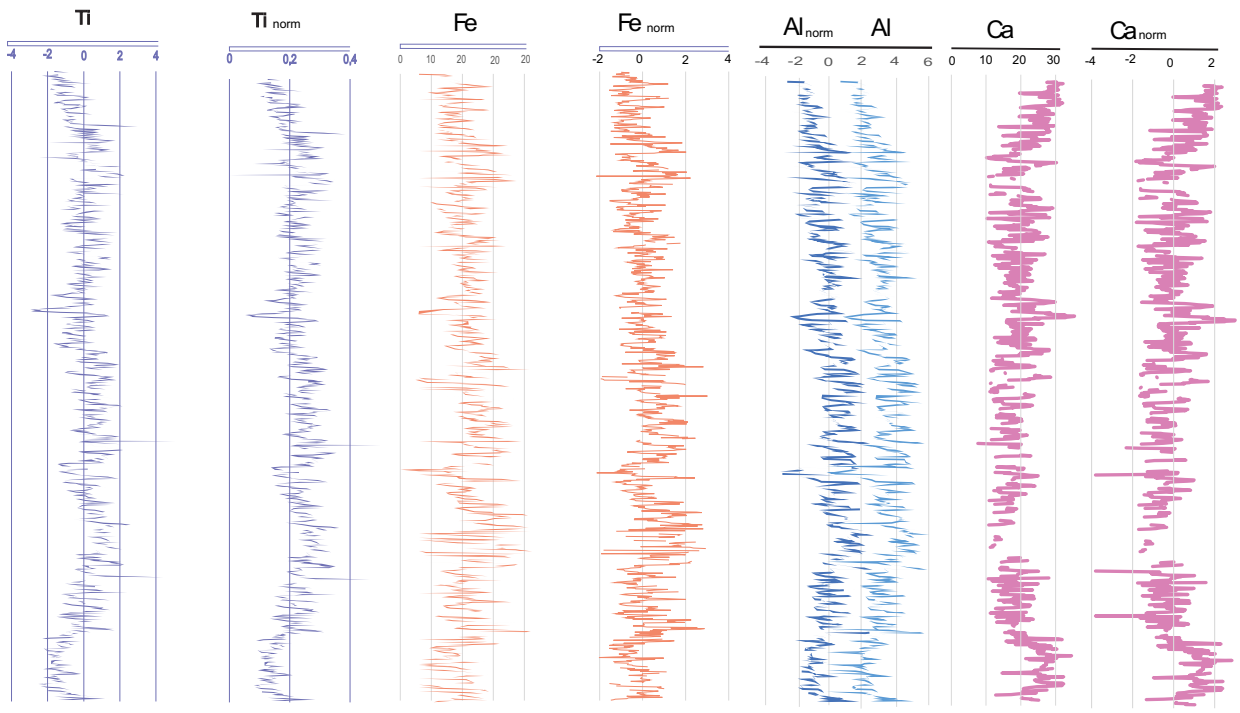

Fig. 16 – Graphs comparing the correlation among XRF data normalized and non-normalized for Ti, Fe, Al and Ca.

It is essential to note that data normalization is a critical step in data processing, ensuring that the data are scaled to a comparable range. This normalization procedure enables meaningful comparisons and interpretations of the results and is a crucial aspect of robust data analysis.

5.5.4 Principal Components Analysis (PCA)

The results of the geochemical/statistical PCA analysis are summarized in the following tables, graphics and figures. The data are organized according to lithology and stratigraphic intervals, allowing for a detailed comparison of the geochemical characteristics across different levels and intervals. In general, the abundances of Al, Si, Ti, and Fe exhibit similar trends. In general, they show slightly higher values in the middle of the section, roughly between the Monte Nerone and the Leenhardt level (Fig. 15). Superimposed on these trends are medium- and short-term rhythmic fluctuations, showing minima just above the Monte Nerone level, close to the Leenhardt level, and in the upper part of the section. The trends of these elements are opposite to those of Ca, Cd, and Mn. Notably, in the black shale layers Al, Si, Ti, and Fe are highest, while Ca, Cd, and Mn are lowest. On the other hand, there is no clear match between the elemental variations and the switches between greenish and reddish lithology. V shows a fluctuating signal, but not clearly correlatable with any other element, and with distinctly more noisy values from 51m upwards.

[1] JACOB LEVEL (67.44-67.52m)

PC1 represents 67,45% and PC2 29,97% variance of the Jacob Level. PC1 and PC2 together explain 97,43% of the total variance. Table 4a and 4b presents the Summary and loadings values. Figures 17 and 21 shows the main element in PC 1 as Cd and PC 2 is mostly represented by Fe and Ti.

Table 4a. PCA Summary with eigenvalues and percentages of variances for the JACOB Level

Principal Components	Eigenvalues	% Variance
1	0.854792	**67.454**
2	0.379819	**29.973**
3	0.0326072	2.5731

Table 4b. PC1 and PC2 Loading Values for JACOB LEVEL. Principal elements highlighted

Elements	PC 1	PC 2
Al	-0.12152	0.23858
Si	0.00054805	0.25986
K	-1.7858E-17	-4.0426E-17
Ca	-0.00055777	-0.47406
Ti	0.14434	**0.32994**
V	0	0
Mn	-0.037026	-0.52832
Fe	0.13186	**0.49766**
Ni	0.098337	0.049536
Cd	**0.96746**	-0.11276

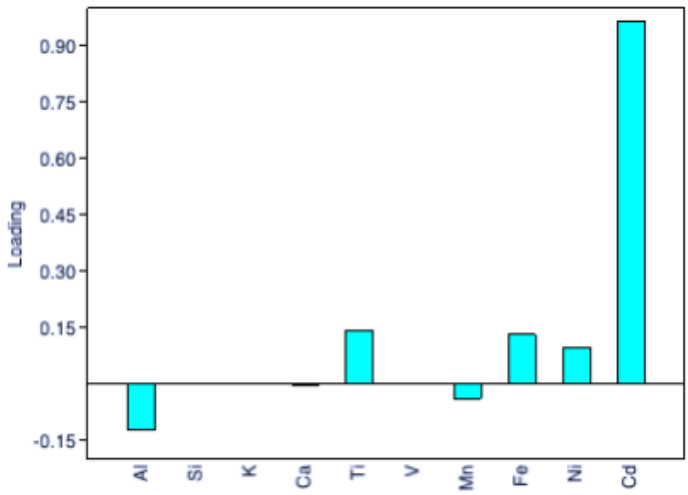

Fig. 17 - *Loadings Plots* in reference to Principal Component 1 for Jacob Level. The principal element positively correlated to PC1 is Cadmium. Data generated by PAST4 software.

[2] KILLIAN LEVEL (62.64 – 63.02m)

PC 1 represents 70,99% variance of the Killian Level. PC1 and PC2 together explain 82,64% of the total variance. Table 5a, 5b shows the Summary and loadings values. Figures 18 and 21 show the main elements in PC 1 as the terrigenous Al followed by Ti and Fe respectively. PC 2 is represented by Cd.

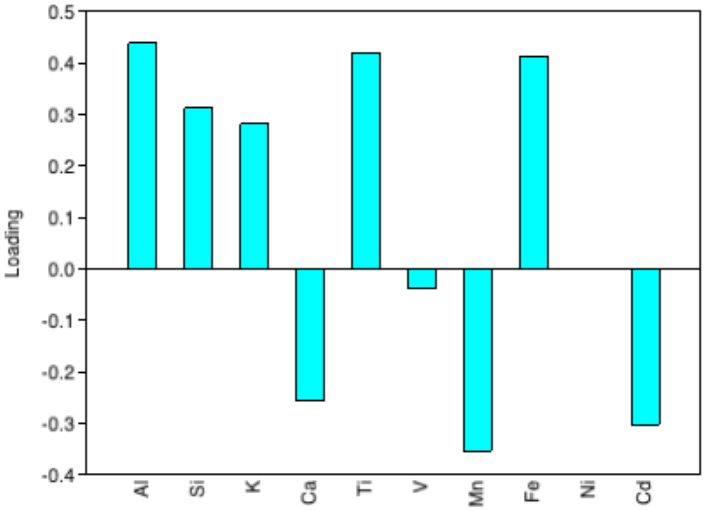

Fig.18 - *Loadings Plots* in reference to Principal Component 1 for Killian Level. The terrigenous Al, Si, K, Ti, and Fe are the principal element positively correlated to PC1. Data generated by *PAST4* software.

Table 5a. PCA Summary with eigenvalues and percentages of variances for the KILIAN Level

Principal Components	Eigenvalues	% Variance
1	3.69993	70.99
2	0.607071	11.648
3	0.461763	8.8598
4	0.176015	3.3772
5	0.116752	2.2401
6	0.0628522	1.2059
7	0.0429447	0.82398
8	0.0333588	0.64005
9	0.00787096	0.15102
10	0.00332558	0.06380

Table 5b. PC1 and PC2 Loading Values for KILIAN LEVEL. Principal elements highlighted

Elements	PC 1	PC 2
Al	**0.43875**	0.088771
Si	0.31251	0.2873
K	0.282	0.0071935
Ca	-0.25607	-0.67033
Ti	**0.41991**	-0.15369
V	-0.037273	0.041532
Mn	-0.35314	-0.05611
Fe	**0.41325**	-0.17422
Ni	-4.7018E-05	0.17585
Cd	-0.30256	**0.60862**

[3] MONTE NERONE (57.07-60.01m)

PC 1 represents 51,43% and PC 2 12,17% variance of the Monte Nerone Level. PC1 and PC2 together explain 80,76% of the total variance. Table 6a, 6b shows the Summary and loadings values. Figures 19 and 21 shows the main elements in PC 1 as the terrigenous Al, Si, K, Ti, Fe and PC 2 is mostly represented by Si and Mn.

Fig.19 – *Loadings Plots* in reference to Principal Component 1 for Monte Nerone Level. The terrigenous Al, K, Si, Ti and Fe are the principal elements positively correlated to PC1. Data generated by *PAST4* software.

Table 6a. PCA Summary with eigenvalues and percentages of variances for the MONTE NERONE Level

Principal Components	Eigenvalues	% Variance
1	3.79696	**67.632**
2	0.683233	**12.17**
3	0.266727	4.751
4	0.23666	4.2154
5	0.201447	3.5882
6	0.141531	2.521
7	0.120198	2.141
8	0.0815118	1.4519
9	0.067334	1.1994
10	0.0185506	0.33043

Table 6b. PC1 and PC2 Loading Values for MONTE NERONE LEVEL. Principal elements highlighted

Elements	PC 1	PC 2
Al	**0.40857**	0.37466
Si	**0.33769**	**0.60482**
K	**0.40011**	-0.033541
Ca	-0.13635	0.1596
Ti	**0.31064**	-0.034251
V	-0.031131	-0.054167
Mn	-0.5004	**0.48359**
Fe	**0.38259**	-0.11216
Ni	0.0011392	-0.44716
Cd	-0.21475	0.12933

[4] URBINO LEVEL (54.63 – 54.88m)

PC 1 represents 51,43% and PC 2 29,33% variance of the Urbino Level. PC1 and PC2 together explain 80,76% of the total variance. Table 7a, 7b shows the Summary and loadings values. Figures 20 and 21 shows the main elements in PC 1 as the terrigenous Al, Si, K and Fe. PC 2 is mostly represented by Cd.

Table 7a. PCA Summary with eigenvalues and percentages of variances for the URBINO Level

Principal Components	Eigenvalues	% Variance
1	**0,639144**	**51,431**
2	**0,364471**	**29,329**
3	0,13543	10,898
4	0,0820426	6,6019
5	0,0135583	1,091
6	0,00555804	0,44725
7	0,00143587	0,11554
8	0,00107519	0,086519

Table 7b. PC1 and PC2 Loading Values for URBINO LEVEL. Principal elements highlighted

Elements	PC 1	PC 2
Al	**0.49546**	0.015942
Si	**0.4254**	0.13869
K	**0.31766**	0.097497
Ca	-0.40396	-0.24917
Ti	0.18391	-0.093911
V	0.081893	-0.64438
Mn	-0.32741	0.10667
Fe	**0.32136**	0.17588
Ni	0.077847	0.02691
Cd	-0.22893	**0.66471**

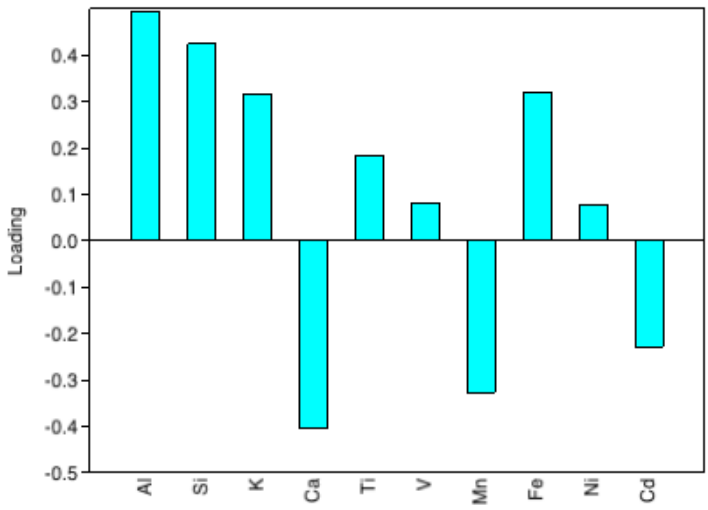

Fig. 20 - *Loadings Plots* in reference to Principal Component 1 for Urbino Level. PC1 is positively correlated for the terrigenous elements Al. Si, F e K. Data generated by PAST4 software.

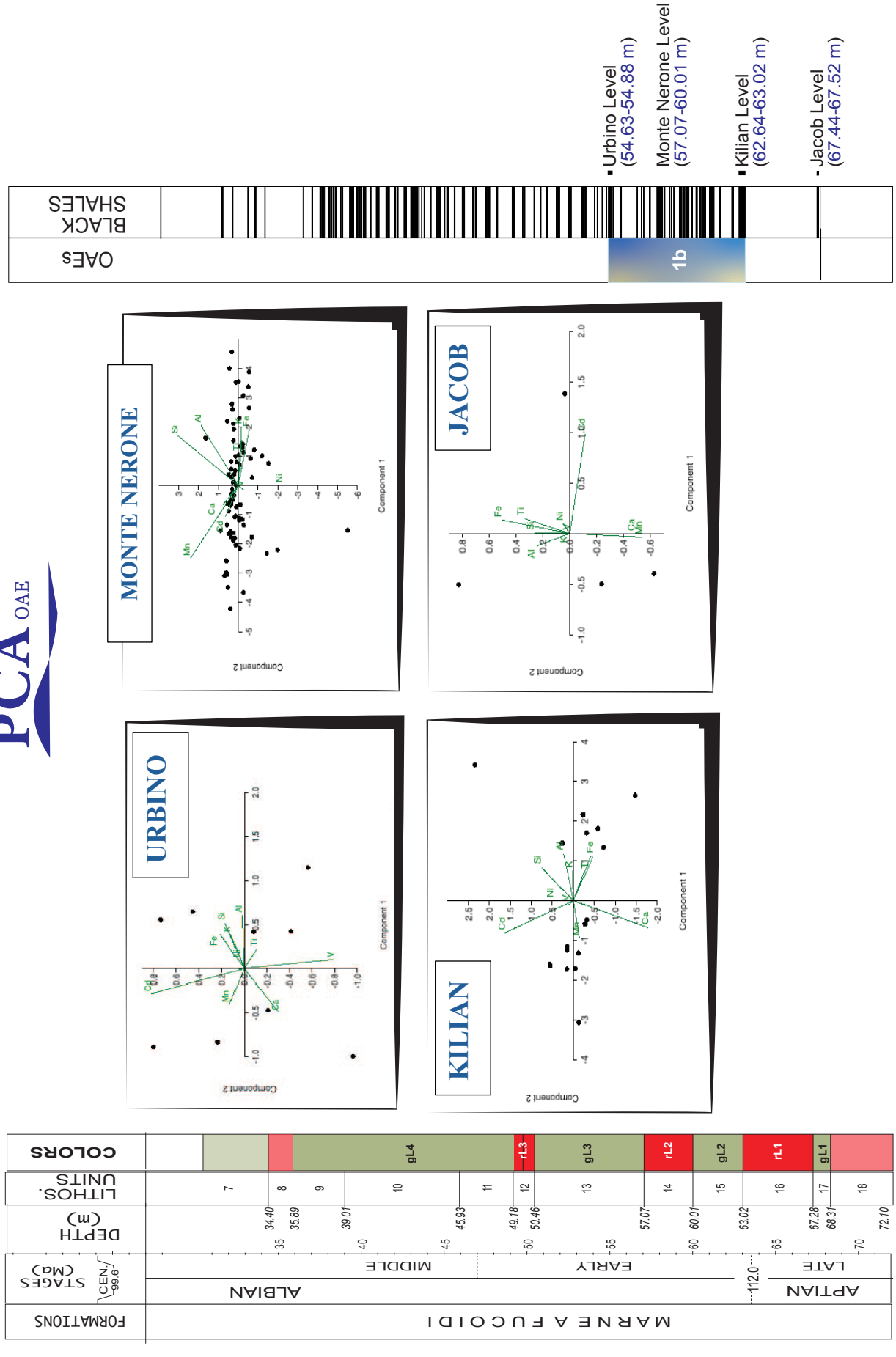

Fig.21 - PCA *Scatter Plots* of the anoxic Aptian - Albian levels: Urbino, Monte Nerone, Killian and Jacob. Data generated on *PAST4* software.

The second PCA analysis was made for the intervals PRE OAE 1b, OAE 1b and POST OAE 1b.

[5] PRE OAE 1b interval (63.05 – 67.41m)

PC1 represents 55,2% and PC2 20% variance of the pre OAE 1b Level. PC1 and PC2 together explain 71% of the total variance. Table 8a, 8b shows the Summary and loadings values. Figures 22 and 33 shows the main element in PC1 as Ti, Al, Si and Fe. PC 2 is mostly represented by V and Ti.

Table 8a. PCA Summary with eigenvalues and percentages of variances for the PRE OAE 1b

Principal Components	Eigenvalues	% Variance
1	3.29255	**55.209**
2	0.977331	**16.388**
3	0.504693	8.4627
4	0.341226	5.7217
5	0.276916	4.6433
6	0.210872	3.5359
7	0.120529	2.021
8	0.0993878	1.6665
9	0.0822005	1.3783
10	0.0580596	0.97354

Table 8b. PC1 and PC2 Loading Values for PRE OAE 1b. Principal elements highlighted

Elements	PC 1	PC 2
Al	**0.38743**	-0.090824
Si	**0.37074**	-0.13389
K	0.15044	0.0052131
Ca	-0.32316	0.1997
Ti	**0.43922**	**0.49176**
V	0.042495	**0.75759**
Mn	-0.42216	0.30068
Fe	**0.33806**	-0.059813
Ni	0.098843	0.015947
Cd	-0.2973	-0.15461

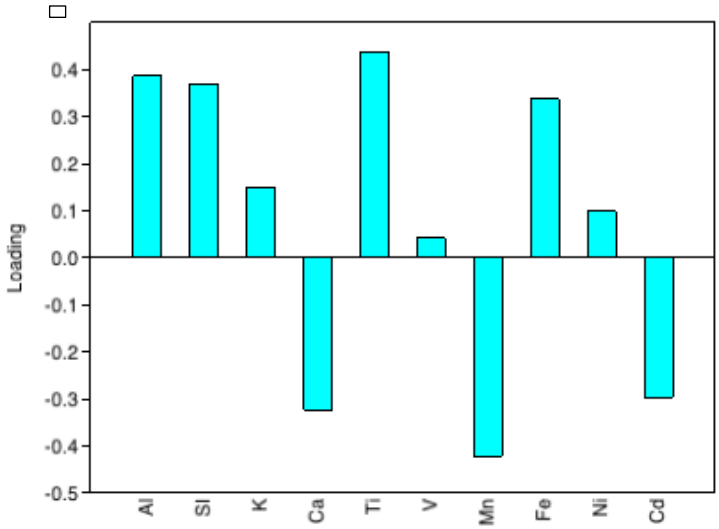

Fig.22 – *Loadings Plots* in reference to Principal Component 1 for pre OAE 1b. The terrigenous Ti, Al, Si and Fe are the principal elements positively correlated to PC1. Data generated by *PAST4* software.

[6] OAE 1b interval (54.64 – 63.02m)

PC1 represents 69,24% and PC2 9,46% variance of the OAE 1b Level. PC1 and PC2 together explain 78,7% of the total variance. Table 9a, 9b shows the Summary and loadings values. Figures 23 and 33 shows the main element in PC 1 as Al, K, Fe, Si and Ti. PC 2 is mostly represented by Si and Mn.

Table 9a. PCA Summary with eigenvalues and percentages of variances for the OAE 1b

Principal Components	Eigenvalues	% Variance
1	3.98213	**69.242**
2	0.544032	**9.4597**
3	0.307198	5.3416
4	0.238439	4.146
5	0.199832	3.4747
6	0.152513	2.6519
7	0.133888	2.3281
8	0.08852	1.5392
9	0.0823251	1.4315
10	0.0221654	0.38542

Table 9b. PC1 and PC2 Loading Values for OAE 1b. Principal elements highlighted

Elements	PC 1	PC 2
Al	**0.41305**	0.38394
Si	**0.32811**	**0.59281**
K	**0.37856**	-0.023977
Ca	-0.16472	0.13209
Ti	**0.34248**	-0.049997
V	-0.016563	-0.069511
Mn	-0.48041	**0.46677**
Fe	**0.38512**	-0.075158
Ni	0.021255	-0.46675
Cd	-0.23272	0.18556

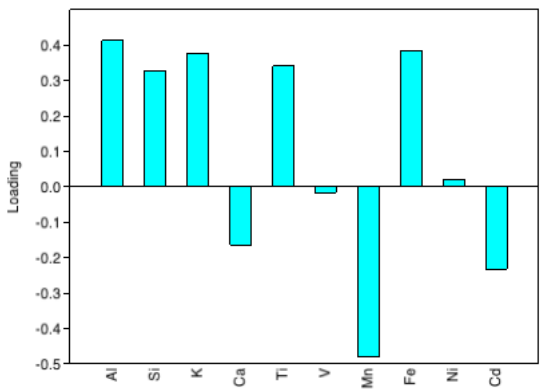

Fig. 23 – *Loadings Plots* in reference to Principal Component 1 for OAE 1b. The terrigenous Al, Si, K, Ti and Fe are the principal element positively correlated to PC1. Data generated by *PAST4* software.

[7] POST-OAE 1b interval (36.02 - 54.61m)

PC1 represents 47,53% and PC2 14,37% variance of the post OAE 1b Level. PC1 and PC2 together explain 61,90% of the total variance. Table 10a, 10b shows the Summary and loadings values. Figures 24 and 33 shows the main element in PC1 they are Al, Ti, Si and Fe. PC 2 is mostly represented by Ni.

Table 10a. PCA Summary with eigenvalues and percentages of variances for POST OAE 1b

Principal Components	Eigenvalues	% Variance
1	**4.22597**	**47.53**
2	**1.27769**	**14.37**
3	0.888798	9.9964
4	0.818056	9.2007
5	0.51488	5.7909
6	0.432158	4.8605
7	0.387299	4.356
8	0.163274	1.8364
9	0.122667	1.3796
10	0.0604268	0.67962

Table 10b. PC1 and PC2 Loading Values for POST OAE 1b. Principal elements highlighted

Elements	PC 1	PC 2
Al	**0.41898**	-0.10731
Si	**0.37442**	-0.161
K	0.12875	-0.016302
Ca	-0.38717	-0.047152
Ti	**0.39669**	-0.088219
V	0.24291	-0.1881
Mn	-0.33311	-0.085078
Fe	**0.30117**	-0.023312
Ni	0.095459	**0.93284**
Cd	-0.30107	-0.19733

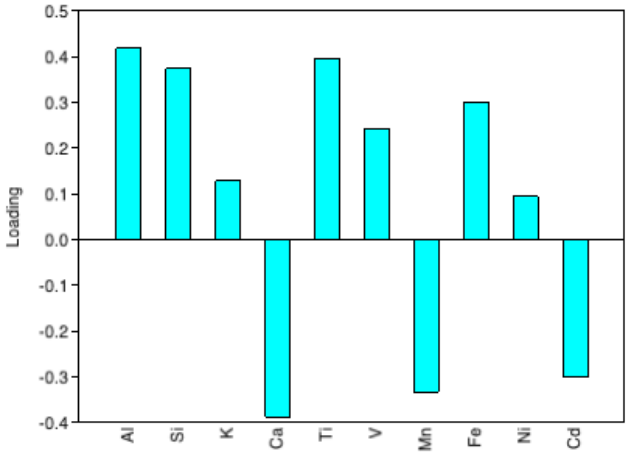

Fig. 24 – *Loadings Plots* in reference to Principal Component 1 for pos OAE 1b. The terrigenous Al, Si, Ti and Fe are the principal element positively correlated to PC1. Data generated by PAST4 software.

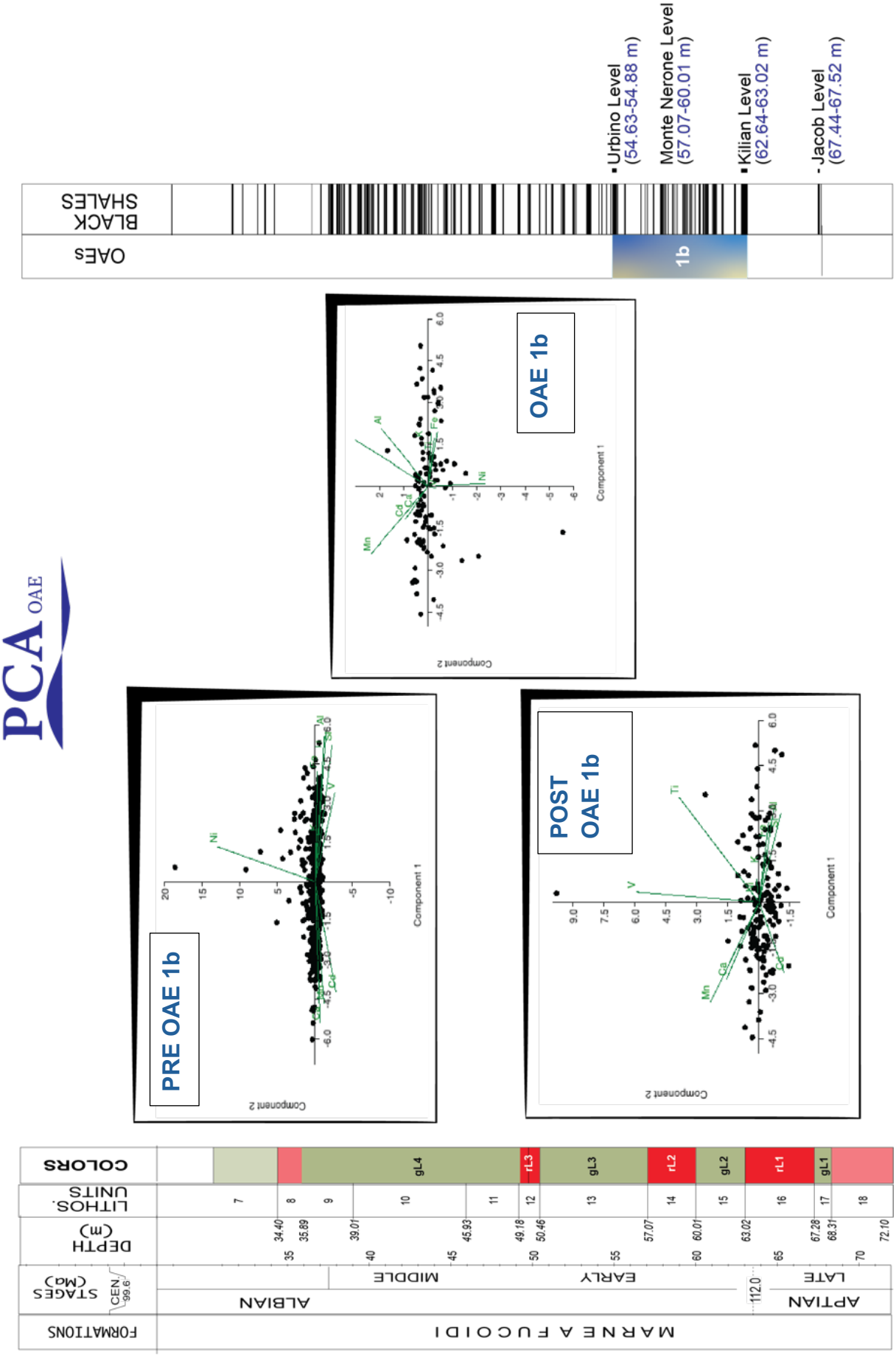

Fig. 25 – PCA *Scatter Plot* of *Marne a Fucoidi* Stratigraphic Levels during Aptian – Albian OAE 1b. POS 1b (36.02 - 54.61m), OAE 1b (54.64 – 63.02m) and PRE OAE 1b (63.05 – 67.41m). (Data generated on *PAST4* software.

The next dataset was made for the Green and Red stratigraphic levels from Coccioni, 2012.

[8] [1] GREEN Level 1 (67.28-68.31m)

PC1 represents 47,18% and PC2 27,4% variance of the Green Level 1. PC1 and PC2 together explain 74,65% of the total variance. Table 11a, 11b shows the Summary and loadings values. Figures 26 and 33 shows the main element in PC1 as Mn and Si. PC 2 is mostly represented by Fe.

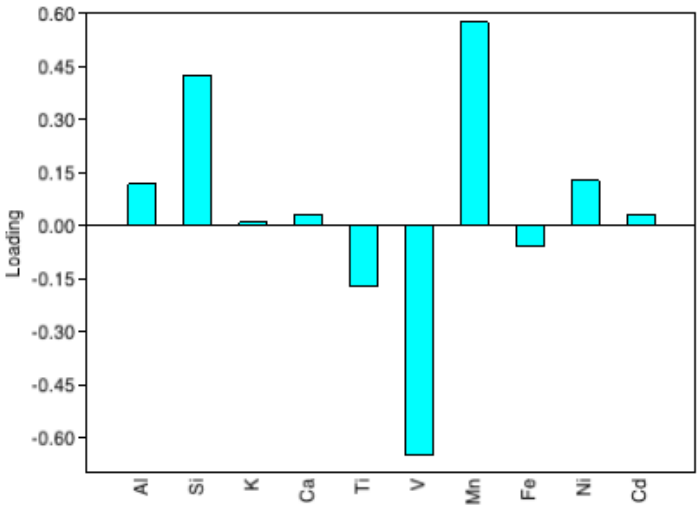

Fig. 26 - *Loadings Plots* in reference to Principal Component 1 for Green Level 1 (GL1). Si and Mn are the principal elements positively correlated to PC1. Data generated by *PAST4* software.

.

Table 11a. PCA Summary with eigenvalues and percentages of variances for GREEN LEVEL 1 (GL1)

Principal Components	Eigenvalues	% Variance
1	1.41435	**47.186**
2	0.823123	**27.461**
3	0.438829	14.64
4	0.129974	4.3363
5	0.0600101	2.0021
6	0.0456863	1.5242
7	0.035483	1.1838
8	0.0221039	0.73744
9	0.0191595	0.63921
10	0.00866762	0.28917

Table 11b. PC1 and PC2 Loading Values for GREEN LEVEL 1 (GL1). Principal elements

Elements	PC 1	PC 2
Al	0.11957	0.22066
Si	**0.42688**	0.26711
K	0.0099943	0.036445
Ca	0.031955	-0.43357
Ti	-0.17102	0.18542
V	-0.64883	-0.10507
Mn	**0.57559**	-0.19884
Fe	-0.058879	**0.57771**
Ni	0.12763	0.016626
Cd	0.032682	-0.52122

[2] RED Level 1
(63.05-67.28m)

PC1 represents 54,5% and PC2 16,98% variance of the Red Level 1. PC1 and PC2 together explain 71,48% of the total variance. Table 12a, 12b shows the Summary and loadings values. Figures 27 and 33 shows the main elements in PC1 are Ti, Al, Si and Fe. PC 2 is mostly represented by Ti and V.

Table 12a. PCA Summary with eigenvalues and percentages of variances for RED LEVEL 1 (RL1)

Principal Components	Eigenvalues	% Variance
1	3.22607	**54.491**
2	1.00572	**16.988**
3	0.495547	8.3702
4	0.345539	5.8364
5	0.276198	4.6652
6	0.204437	3.4531
7	0.121128	2.046
8	0.101438	1.7134
9	0.0847979	1.4323
10	0.0594928	1.0049

Table 12b. PC1 and PC2 Loading Values for RED LEVEL 1 (RL1). Principal elements highlighted

Elements	PC 1	PC 2
Al	**0.38949**	-0.083884
Si	**0.35989**	-0.13987
K	0.16032	0.015216
Ca	-0.31502	0.20832
Ti	**0.42758**	**0.49683**
V	0.034069	**0.75782**
Mn	-0.44146	0.28395
Fe	**0.34682**	-0.044277
Ni	0.10113	0.021424
Cd	-0.29061	-0.15997

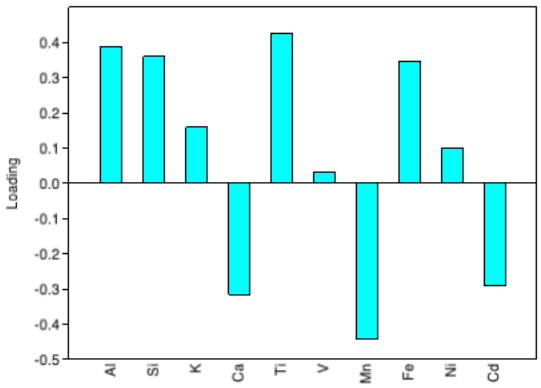

Fig. 27 - *Loadings Plots* in reference to Principal Component 1 for Red Level 1 (RL1). The terrigenous Al, Si, Ti and Fe are the principal elements positively correlated to PC1. Data generated by PAST4 software.

[3] GREEN Level 2 (60.01-63.02m)

PC1 represents 53,45% and PC2 15,16% variance of the Green Level 2. PC1 and PC2 together explain 68,61% of the total variance. Table 13a, 13b shows the Summary and loadings values. Figures 28 and 33 shows the main element in PC1 as Si, AL, Fe and Ti. PC 2 is mostly represented by Fe.

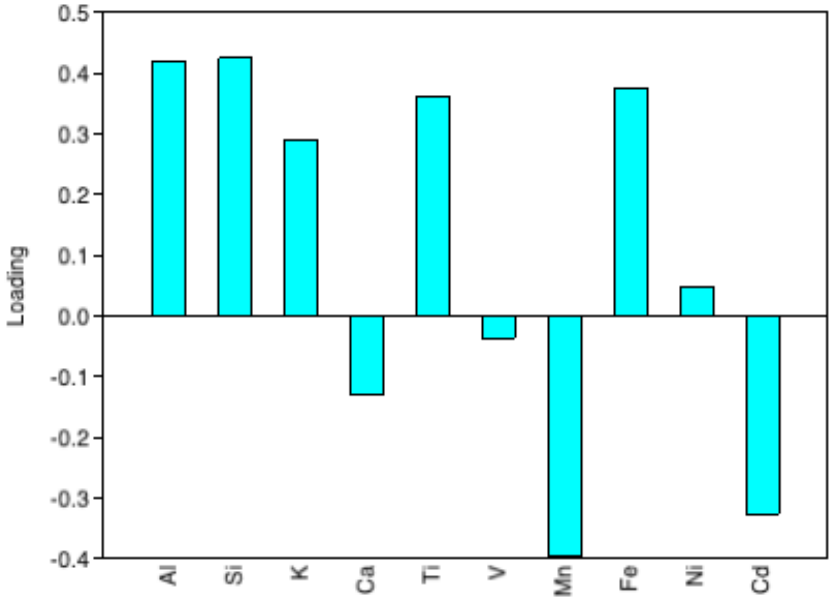

Fig. 28 - *Loadings Plots* in reference to Principal Component 1 for Green Level 2 (GL2). Al, Si, Ti and Fe are the principal elements positively correlated to PC1. Data generated by PAST4 software.

Table 13a. PCA Summary with eigenvalues and percentages of variances for GREEN LEVEL 2 (GL2)

Principal Components	Eigenvalues	% Variance
1	2.18376	**53.455**
2	0.619447	**15.163**
3	0.396246	9.6995
4	0.235357	5.7612
5	0.150445	3.6827
6	0.135016	3.305
7	0.123415	3.021
8	0.116945	2.8626
9	0.0809265	1.981
10	0.0436596	1.0687

Table 13b. PC1 and PC2 Loading Values for GREEN LEVEL 2 (GL2). Principal elements highlighted

Elements	PC 1	PC 2
Al	**0.42095**	-0.18658
Si	**0.42612**	-0.26773
K	0.29074	-0.10438
Ca	-0.12927	0.014132
Ti	**0.36271**	0.062022
V	-0.036007	0.17341
Mn	-0.39645	0.19671
Fe	**0.37585**	**0.88687**
Ni	0.048578	0.034323
Cd	-0.32609	0.14862

[4] RED Level 2 (RL2) (57.08-60.01m)

PC1 represents 72,85% and PC2 6,3% variance of the Red Level 2. PC1 and PC2 together explain 79,15% of the total variance. Table 14a, 14b shows the Summary and loadings values. Figures 29 and 33 shows the main element in PC1 as Al, Si, K, Ti and Fe. PC 2 is mostly represented by Ca, Si and Mn.

Table 14a. PCA Summary with eigenvalues and percentages of variances for RED LEVEL 2 (RL2)

Principal Components	Eigenvalues	% Variance
1	3.81986	72.849
2	0.330723	6.3072
3	0.257804	4.9166
4	0.222894	4.2508
5	0.204832	3.9064
6	0.135196	2.5783
7	0.115184	2.1967
8	0.0760979	1.4513
9	0.0626035	1.1939
10	0.018352	0.34999

Table 14b. PC1 and PC2 Loading Values for RED LEVEL 2 (RL2). Principal elements highlighted

Elements	PC 1	PC 2
Al	**0.3962**	0.29854
Si	**0.3182**	**0.43485**
K	**0.40291**	0.076915
Ca	-0.13797	**0.50689**
Ti	**0.31281**	0.029985
V	-0.031154	-0.37025
Mn	-0.51524	**0.39707**
Fe	**0.38578**	0.059865
Ni	0.01642	-0.32006
Cd	-0.21681	0.23927

Fig.29 - *Loadings Plots* in reference to Principal Component 1 for Red Level 2 (RL2). Al, Si, K, Ti and Fe are the principal elements positively correlated to PC1. Data generated by PAST4 software.

[5] GREEN Level 3 (GL3) (50.49-57.08m)

PC1 represents 46% and PC2 16,48% variance of the Green Level 3. PC1 and PC2 together explain 62,55% of the total variance. Table 15a, 15b shows the Summary and loadings values. Figures 30 and 33 shows the main element in PC1 as Al, Si and Ti. PC 2 is mostly represented by Ni and K.

Table 15a. PCA Summary with eigenvalues and percentages of variances for GREEN LEVEL 3 (GL3)

Principal Components	Eigenvalues	% Variance
1	3.62098	**46.065**
2	1.29565	**16.483**
3	0.91966	11.7
4	0.546584	6.9534
5	0.485383	6.1748
6	0.32192	4.0953
7	0.31199	3.969
8	0.161226	2.0511
9	0.144451	1.8376
10	0.0528208	0.67196

Table 15b. PC1 and PC2 Loading Values for GREEN LEVEL 3 (GL3). Principal elements highlighted

Elements	PC 1	PC 2
Al	**0.44406**	-0.27598
Si	**0.42121**	-0.26825
K	0.18572	**0.39348**
Ca	-0.19792	-0.11351
Ti	**0.33532**	-0.051243
V	-0.022835	0.19196
Mn	-0.53867	-0.22466
Fe	0.2476	-0.052696
Ni	0.0095336	**0.75281**
Cd	-0.2953	-0.15721

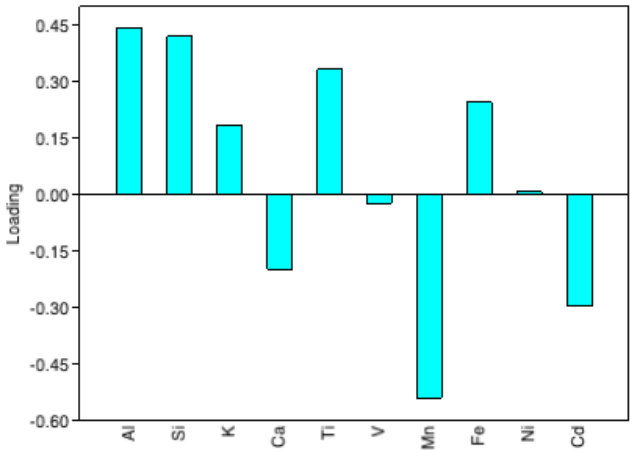

Fig.30 - Loadings *Plots* in reference to Principal Component 1 for Green Level 3 (GL3). Al, Si, K, Ti and Fe are the principal elements positively correlated to PC1. Data generated by PAST4

[6] RED Level 3 (RL3) (49.20-50.46m)

PC1 represents 68,8% and PC2 15,08% variance of the Red Level 3. PC1 and PC2 together explain 83,89% of the total variance. Table 16a, 16b shows the Summary and loadings values. Figures 31 and 33 shows the main element in PC1 is Ni and PC 2 is mostly represented by Cd, Mn and Ca.

Table 16a. PCA Summary with eigenvalues and percentages of variances for RED LEVEL 3 (RL3)

Principal Components	Eigenvalues	% Variance
1	10.8533	**68.813**
2	2.3788	**15.082**
3	1.59285	10.099
4	0.634238	4.0213
5	0.124882	0.79179
6	0.0717501	0.45492
7	0.0671048	0.42546
8	0.0301239	0.19099
9	0.0124936	0.079213
10	0.00658101	0.041726

Table 16b. PC1 and PC2 Loading Values for RED LEVEL 3 (RL3). Principal elements highlighted

Elements	PC 1	PC 2
Al	-0.055546	-0.2419
Si	-0.059036	-0.20018
K	0.00015062	-0.11892
Ca	-0.024518	**0.34495**
Ti	-0.0041775	-0.1898
V	-0.015659	-0.016543
Mn	-0.048587	**0.39564**
Fe	-0.025431	-0.16763
Ni	**0.99344**	0.035322
Cd	-0.051369	**0.73899**

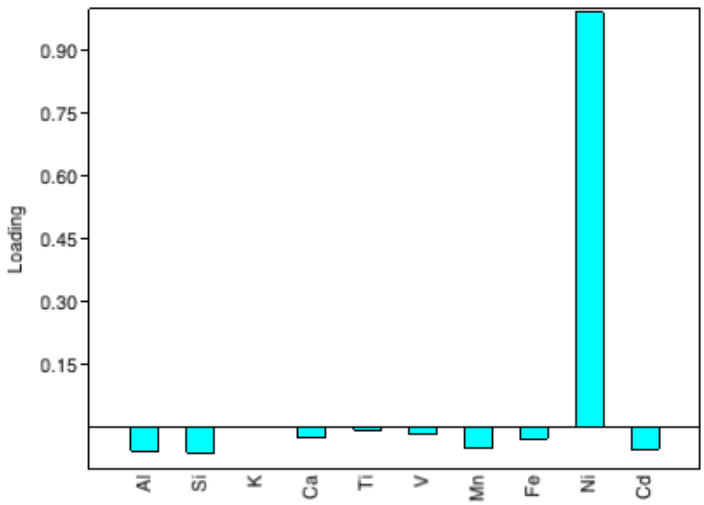

Fig.31 - *Loadings Plots* in reference to Principal Component 1 for Red Level 3 (RL3). High level of Nickel as the principal element positively correlated to PC1. Data generated by *PAST4* software.

[6] Green Level 4 (GL4) (39.01 – 49.17m)

PC1 represents 50,69% and PC2 11,99% variance of the Green Level 4. PC1 and PC2 together explain 62,68% of the total variance. Table 17a, 17b shows the Summary and loadings values. Figures 33 and 32 shows the main element in PC1 as Al, Si and Ti and PC 2 is mostly represented by Cd and V.

Table 17a. PCA Summary with eigenvalues and percentages of variances for GREEN LEVEL 4 (GL4)

Principal Components	Eigenvalues	% Variance
1	4.13897	**50.69**
2	0.978961	**11.989**
3	0.852684	10.443
4	0.601212	7.3631
5	0.531778	6.5127
6	0.42621	5.2198
7	0.292368	3.5807
8	0.157305	1.9265
9	0.116912	1.4318
10	0.0687999	0.8426

Table 17b. PC1 and PC2 Loading Values for GREEN LEVEL 4 (GL4). Principal elements

Elements	PC 1	PC 2
Al	**0.37918**	0.09036
Si	**0.34809**	0.19647
K	0.090409	-0.025377
Ca	-0.42063	0.072686
Ti	**0.41336**	0.15243
V	0.27299	**0.63665**
Mn	-0.31365	0.12436
Fe	0.29176	-0.076052
Ni	0.083481	-0.15995
Cd	-0.33778	**0.68696**

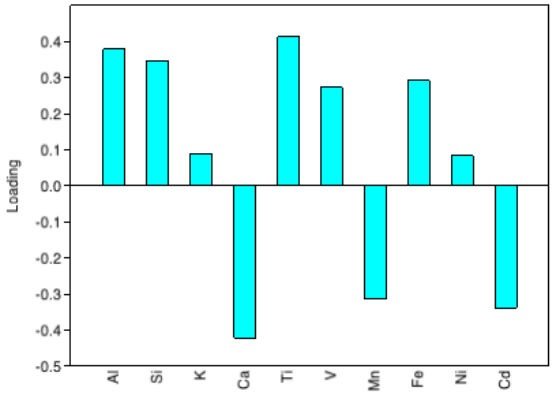

Fig.32 - *Loadings Plots* in reference to Principal Component 1 for Green Level 4 (GL4). The terrigenous Al, Si, Ti, V and Fe are the principal element positively correlated to PC1. Data generated by *PAST4* software.

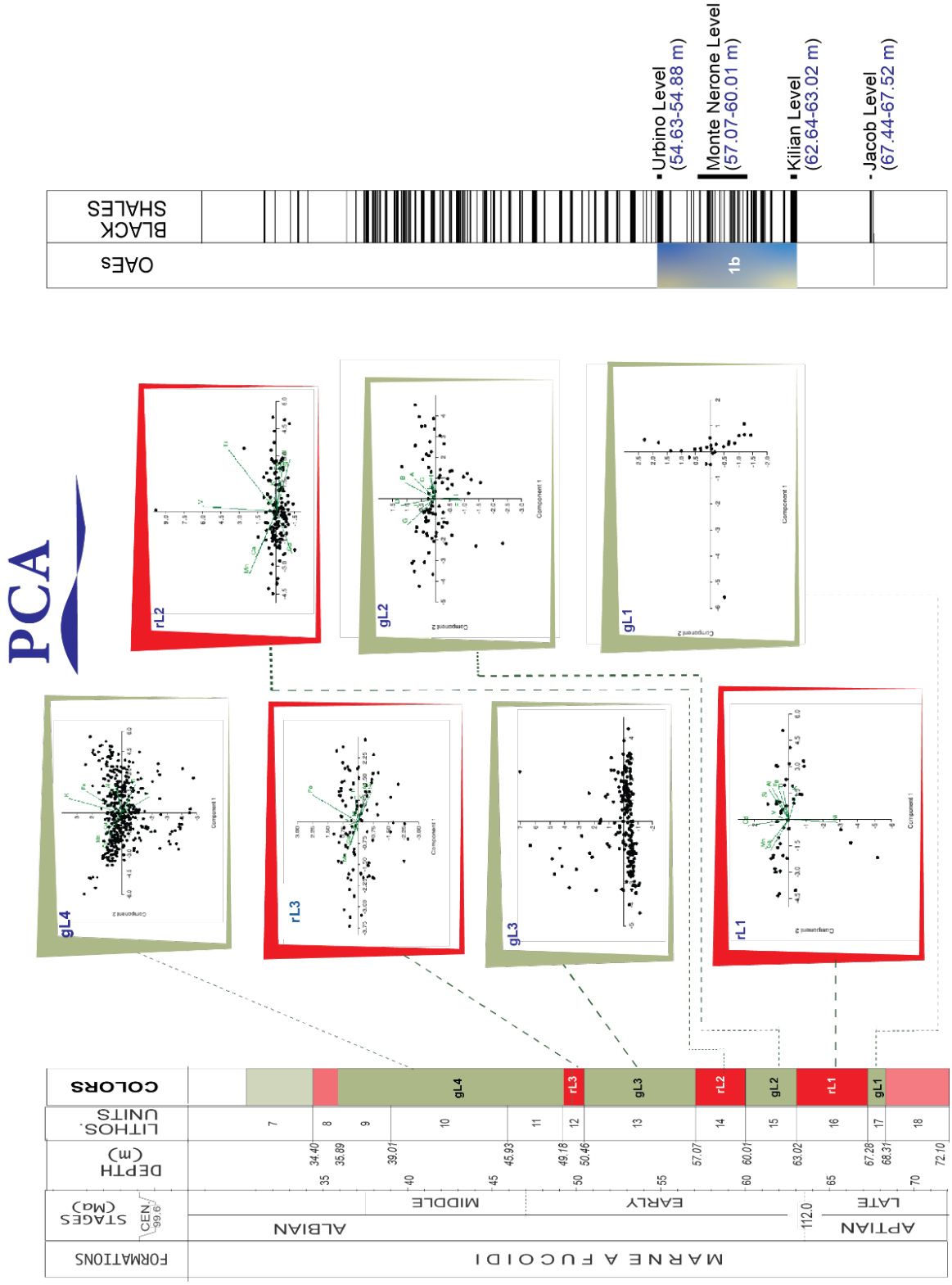

Fig. 33 – PCA *Scatter Plot* of Green (gL1, gL2, gL3 and gL4) and Red (rL1, rL2 and rL3) *Marne a Fucoidi* Stratigraphic Levels during Aptian – Albian OAE 1b. Data generated on *PAST4* software.

5.6 | Discussion

Originally, the OAE 1b in the Umbria-Marche basin was represented only by the Urbino/Paquier Level, whereas currently it includes 4 more black shale levels (Bodin et al, 2023). This event occurs in a period with extreme climatic instability, which makes it difficult to estimate its exact duration and the environmental changes related to it. Despite all the uncertainties, Ramos et al. (2024) estimate a new timespan of ~2.84 Myr for the OAE 1b interval (Jacob to Leenhardt levels).

5.6.1 Elemental Analysis & Principal Components

High resolution PCA analysis of different levels in the Aptian-Albian PLG core shows a high influence of terrigenous elements during this period. Fluctuations of the detrital elements such as Al, Ti, and Fe in XRF data (Figure 16) present long and short term cyclicities that can represent orbital variations. The actual occurrence and significance of orbital signals in the elemental dataset of the PLG core has been assessed by Ramos et al (2024), therefore we do not address this aspect here.

Al appears to be coupled to Si, K, Fe, and Ti due to their common detrital nature. Manganese, Calcium, and Cadmium content are usually correlated to one another, and anticorrelated to the terrigenous fraction (Fig.20). Calcium shows higher values in the light bioturbated facies, richer in carbonate, while Al presents higher values in the darker, carbonate poor levels. These fluctuations indicate a relative increase of detrital and decrease in biogenic inputs on local scale during anoxic phases.

When plotting the data along the PC1 and PC2, two distinct clusters based on origins and compositions emerge: the terrigenous elements versus the authigenic/biogenic elements. PC1 appears to represent the overall composition of the geological interval, as the terrigenous elements had high loadings. PC2 in general, is representing the biogenic and authigenic elements Ca, Mn, and Cd. V and Ni as redox sensitive trace elements, fluctuate across different levels, sometimes correlated with detrital elements, other times not. Although the concentrations of elements vary throughout the whole interval, the chemical signal is dominated by Cd in the Jacob level, and by Ni in Green Level 1, and Red Level 3 (Figs. 16, 21 and 33)

Fluctuations in aluminum (Al) and titanium (Ti) levels can be linked to changes in continental runoff and freshwater input into the basin. Freshwater, being less dense, remains at the ocean surface, enhancing water column stratification. As a result, deep water becomes less oxygenated. The biological pump exports organic matter to the deep sea, consuming oxygen in the process. In a poorly mixed water column, oxygen levels at the bottom decrease, leading to the preservation of organic matter (e.g., Giorgioni et al., 2017).

From the stratigraphic bottom to the top, we analyzed the four main black shale horizons within the *OAE* 1b interval (Jacob, Killian, Monte Nerone and Urbino/Paquier) and the red and green levels identified by Coccioni et al. (2015). The following reconstruction is referred to local changes in the PLG sequence from the Aptian-Albian boundary (Jacob level/Green Level 1) to the uppermost Urbino Level.

Black Shales – Anoxic levels

The Jacob Level consists of dark gray to black shale sediments (Coccioni, 2012; Fig. 11), characterized by high total organic carbon (TOC) values of up to 5.9% and Type II sedimentary organic matter. This suggests a significant marine contribution, complemented by terrestrial inputs (Erbacher et al., 1999; Heimhofer et al., 2006; Sabatino et al., 2015). Our analysis reveals an anomalously high cadmium (Cd) content, accompanied by slight increases in titanium (Ti) and iron (Fe) (Fig. 16). The elevated Ti and Fe levels may indicate increased aeolian input, whereas the high Cd content suggests high primary productivity. This finding is consistent with Sabatino et al. (2015), who reported increased barium (Ba) content in the equivalent interval of the PLG outcrop section, interpreted as pulses of high primary productivity and export of organic matter. These pulses are thought to be driven by elevated atmospheric pCO2, enhanced terrestrial weathering, and increased nutrient delivery to the ocean.

The Kilian Level, second in the sequence of the *OAE* 1b interval, is described by Coccioni et al. (2012) as a dark grey to black shale. (Fig.11). Here, the terrigenous elements (Al, Si, K, Ti, and Fe) present the highest contents of all the black shale levels and are correlated to each other. A negative shift in carbon isotope curve indicates a major contribution of isotopically light terrestrial carbonate ions, delivered by enhanced continental runoff during

more humid conditions. This is supported also by relatively high TOC values (up to 1%) described by Sabatino et al. (2015), and an enrichment of Ti, Mg, and K recorded at the top of this level, suggesting that the highest detrital input occurred at the end of the sub-event. This can indicate enhanced organic matter preservation due to intensified precipitation and terrestrial runoff in more humid climate conditions.

In the Monte Nerone Level (Fig.11), the third in the sequence of the *OAE* 1b, sediments consist of centimetric dark shales, alternated with reddish clayey marls (Sabatino et al, 2015). TOC presents values up to 0.6% and high terrigenous elements' values suggest the presence of strong continental input. The high Mn values suggest a less anoxic environment respect to the other black shale levels.

The Urbino/Paquier level, the fourth in the sequence of the *OAE* 1b interval, yields the highest TOC values up to 9.8% (Sabatino et al., 2015; Fig.11). Previous studies have highlighted that the climax of the OAE 1b occurred between the Killian and Urbino levels, with the latter being the most extended and pronounced black shale interval. The sediments are mostly laminated indicating oxygen-depleted conditions (Sabatino et al., 2015). We identify expressive loadings of V and Ni, correlated to terrigenous elements, which can reflect reducing conditions during the deposition. Previous studies identified evidence of enhanced primary productivity and export of organic matter (Erbacher et al., 1999). The enrichment in Zn, Cd, and Mo can be related to H_2S availability at the seafloor during the organic-rich level deposition (Huckriede and Meischner, 1996; Pacton, 2011; Sabatino et al., 2015). On the other hand, our data do not record anomalous values of these elements in this level (Fig. 15).

Red and Green Levels

The Green Level 1 (GL1) occurs in the upper Aptian and contains the Jacob Level. The Principal Components (PCA) shows a high loading of Mn and Si, anticorrelated with V. The weak signal of terrigenous elements suggests that the composition was mainly controlled by redox conditions rather than detrital input. However, the relatively high Mn values and barely detected V suggest that the redox potential was sufficiently higher to allow Mn precipitation and preservation (Calvert & Pedersen, 1996).

Red Level 1 is an interval between the Jacob and Killian Levels, described by Coccioni et al. (2012) as thinly interbedded pale reddish to dark reddish marls to clayey marls (Fig.11). It presents a main component related to terrigenous elements, especially Ti, indicating a significant terrestrial/aeolian input. V values increase and occur anticorrelated with the terrigenous elements, probably indicating reducing conditions or incorporation into organic matter via biogenic processes.

The Green Level 2 is an alternation of black shales, marls, and radiolarian beds (Coccioni et al., 2012; Fig.11) showing high loadings of terrigenous elements (Al, Si, Ti, and especially Fe), anticorrelated with Mn and Cd. This indicates a main control of the detrital input on the chemical composition, alongside redox conditions.

The Red Level 2 stratigraphically corresponds almost entirely to the Monte Nerone level and exhibits similar geochemical signatures to the GL2 (Fig. 11). It is characterized by an increase in terrigenous elements, with higher loadings of K and Ti, respect to the GL2, which may represent a shift towards a more arid climate.

The Green Level 3 is an alternation of black shales, marls, limestones, and radiolarian beds, including also the Urbino level (Fig. 33). Elemental geochemistry shows high values of Mn, Cd, and Ca, anticorrelated with Al, Si, Ti, and K, indicating a relative increase in productivity at the surface and oxic conditions at the bottom, diluting the terrigenous fraction.

Red Level 3 (Fig.11) is a marly limestone interval almost 1m thick. The PC1 is dominated by Ni above all other elements. Nickel in the oceans shows lower concentrations in surface waters and higher concentrations in deeper layers. This distribution is driven by biological uptake in surface waters, followed by remineralization in deeper waters as organic matter decomposes (Sclater et al., 1976). Therefore, the high Ni content in this interval can indicate an increase in organic matter export to the sediment, despite the relative more oxic conditions suggested by the red color and the redox elements' signature.

The Green Level 4, situated at the top of the section, is characterized by an alternating sequence of marls, limestones, and black shales (Coccioni, 2012). As illustrated in Fig. 15 and 33, and Tables 17a and 17b, this level exhibits fluctuating abundance of terrigenous elements, mirrored by Ca, relatively low Cd and Mn and high V values. This suggests relatively low

oxygen levels in bottom waters, with fluctuating terrigenous and biogenic input coming from the surface, probably controlled by seasonal and orbital cycles (Giorgioni et al., 2017).

5.6.2 Paleoceanographic changes during Aptian-Albian OAE 1b

The clusters (i) Pre OAE, (ii) OAE 1b, and (iii) post-OAE 1b reveal similar patterns with high Ti, Al, Si, Fe, K, and anticorrelated to Mn, Ca, and Cd. Particularly, K content is higher, and Ca is lower within the OAE 1b interval. This could indicate a relatively drier climate, with more intense eolian input and reduced carbonate productivity (Algeo & Liu, 2020; Tribovillard et al., 2006). This, however, was punctuated by strong and frequent shifts in climatic conditions, responsible for the lithological and geochemical changes observed in the short term. The most anomalous signature is observed in the Jacob level, suggesting that a peak in primary productivity occurred in this interval, alongside changes in terrestrial input and redox conditions, probably associated with particularly humid climatic conditions. Relatively high productivity can also be inferred in the Kilian and Urbino levels, whereas the Cd and TOC values suggest that oxygen depletion was mainly related to water circulation rather than primary productivity in the Monte Nerone level.

In the studied succession, Mn depletion was recorded in the Jacob, Kilian, and Monte Nerone intervals, indicating that the bottom waters were oxygen-depleted. However, particularly high Mn is observed in the Urbino/Paquier level, suggesting that Mn could be incorporated in an early diagenetic carbonate phase in anoxic conditions (Wittkop et al., 2020).

The dysoxia/anoxia at the seafloor is deduced by redox sensitive trace metals in the Kilian and Paquier levels (Benamara et al., 2020; Wang et al., 2022). However, low oxygen conditions occur repeatedly throughout the entire Marne a Fucoidi Formation, as testified by the several black shale levels, which were controlled mainly by orbital forcing (e.g. Herbert and Fischer, 1986; Giorgioni et al., 2012; 2017). The fact that no major shift in elemental composition is observed within the OAE 1b interval indicates that there was no significant perturbation in the climatic and oceanographic mechanisms acting in the western Tethys, but rather an intensification of the already unstable climatic conditions. Moreover, we observe that the variations in chemical composition do not systematically match with the color of the lithology, indicating that the various environmental factors, such as terrigenous input,

carbonate productivity, and redox conditions, did not always change at the same time, and thus could respond to different forcings.

With respect to the Jacob Level, the anomalous high content of Cd, low detrital input, high TOC content and accumulation of marine organic carbon (Sabatino et al., 2015), acts as evidence of very high primary productivity during its deposition, which seems to have different driving mechanisms compared to the other 1b black shales and green/red levels. Recent investigations on the onset of the OAE 1b with new age models (Leandro et al., 2022; Ramos et al., 2024) and Osmium isotopes ($^{187}Os/^{188}Os$; Matsumoto et al., 2022) indicate that volcanic activity occurred in correspondence of this episode, which could have warmed the relatively cold climate and contributed to enhance the primary productivity in the oceans, triggering extensive burial of pelagic organic matter.

The general and fundamental hallmark of *OAEs* is an enrichment of sedimentary organic matter in deep marine sediments associated with a prominent increase in $\delta^{13}C_{carb}$ values, up to several permill, such as in the OAE 1a and OAE 2 (Schlanger & Jenkyns, 1976; Jenkyns, 1980, 2010). However, the $\delta^{13}C_{carb}$ curve in the OAE 1b interval of the PLG section presents a general decreasing trend, with various abrupt negative excursions (Fig. 14). According to Sabatino et al. (2015), the negative excursions occur in the Kilian, Monte Nerone, and Urbino/Paquier levels and could be related to a major input of isotopically light terrestrial carbonate ions, due to an increase of continental runoff during more humid conditions. These variations can be observed at a regional extent at least, as they were identified also by Bodin et al. (2023), in the Briers Section, in Southeast of France.

Values of εNd can be linked to sediment provenance to track changes in terrigenous input (Stille et al., 1989). The PLG εNd record exhibits a general persistence of a relatively low values, compatible to Mesozoic rocks from southern Europe, west and south Africa (-11 and -7; Robinson et al., 2021), and lithogenic dust sediments from southern Algeria and northern Mali (-15 to -10; Scheuvens et al., 2013). The εNd shows no significant trend, which may indicate that the terrigenous fraction came always from the same source during this period. The terrestrial input in the pelagic Umbria Marche Basin came from suspended clay fraction within the water column and wind dust. Thus, we can infer from the εNd record that there were no major changes in water circulation, such as the influx of new water masses delivering clay from

a new source, nor alteration of the main winds' patterns during the deposition of the studied interval.

These observations, alongside its extremely longer duration, indicate that different mechanisms were acting during the OAE 1b than during the other OAEs. Instead of a single abrupt event, this interval seems to represent a period of very unstable climatic and oceanographic conditions, punctuated by frequent and rapid changes. Therefore, the OAE 1b can be interpreted just as a period of increased climatic instability at a time of already unstable conditions, as proposed by Wortmann et al. (1999) and Giorgioni et al. (2015).

Figures 34 and 35 present an integration of the data collected with previous studies (Sabatino et al., 2015; Matsumoto et al., 2020; Bodin et al., 2023), providing a comprehensive visualization of the geochemical signature of Poggio le Guaine and equivalent sections. A highly unstable carbon cycle is testified by the rapid fluctuations in the $\delta^{13}C_{carb}$ records throughout the Aptian-Albian period, in the PLG and Briers sections. The geochemical elemental correlation (Al and Ti curves) reveals cyclic variations, which can be related to astronomically driven variations (Giorgioni et al., 2012; Bodin et al., 2023; Ramos et al., 2024). These cyclic variations controlled the monsoonal system, leading to a modification of hydrological cycle, continental runoff, primary productivity, and water circulation during the Aptian-Albian time. The implications of these orbital variations from a stratigraphic and paleoclimatic perspective have been addressed in detail in the recent study by Ramos et al. (2024).

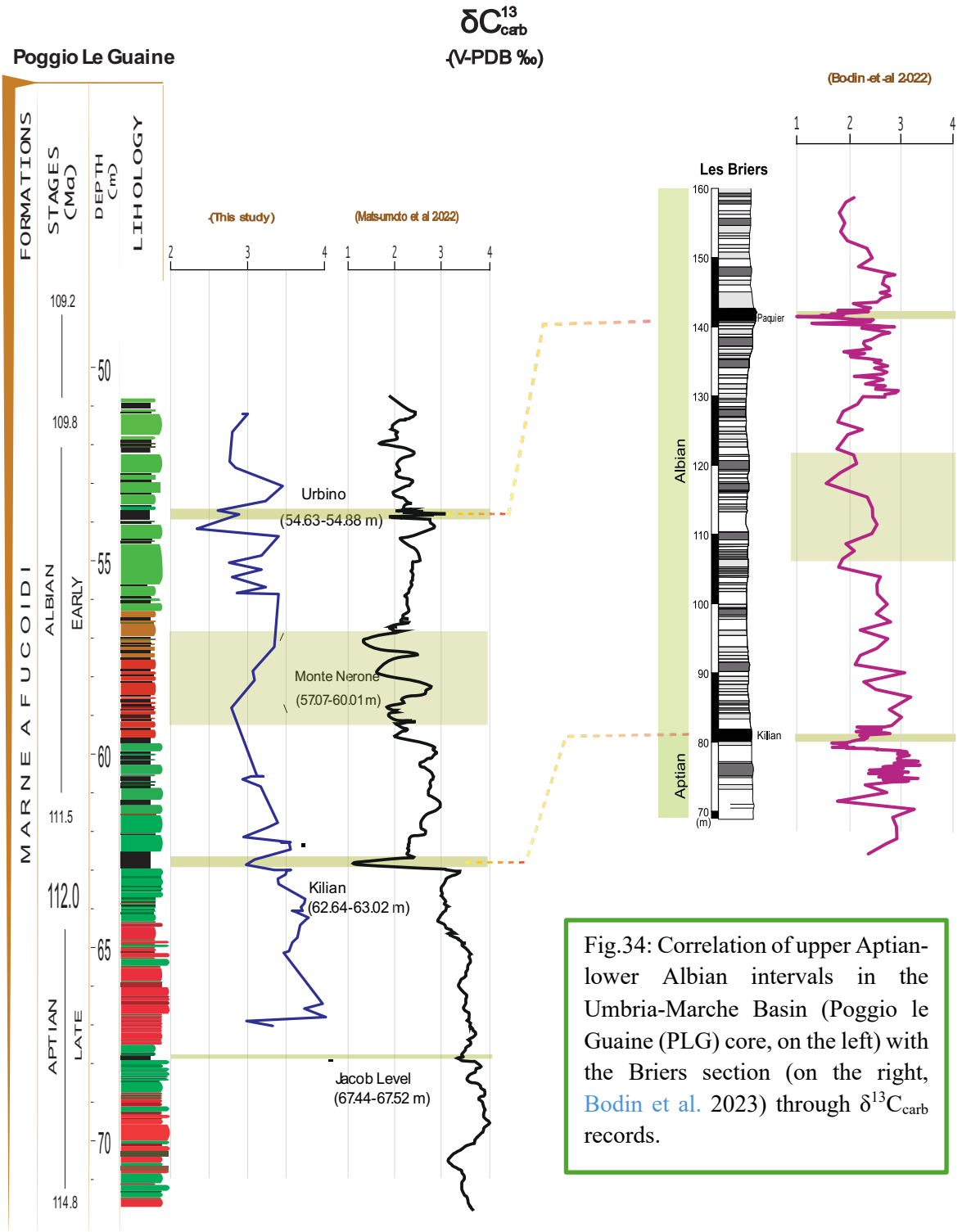

Fig.34: Correlation of upper Aptian-lower Albian intervals in the Umbria-Marche Basin (Poggio le Guaine (PLG) core, on the left) with the Briers section (on the right, Bodin et al. 2023) through $\delta^{13}C_{carb}$ records.

On the other hand, the various sub-events associated to thicker black shale layers (Jacob, Kilian, and Urbino), do not occur in phase with the cyclic variations, and, therefore, were not driven by orbital forcing. Besides, despite being all related to negative $\delta^{13}C_{carb}$ shifts, their elemental signatures are different from one another. Bodin et al. (2023) previously defined long-term variations in Al and Ti trends with similar trend of increasing values from the Jacob level up to around Killian level, followed by a subsequent decrease. Sabatino et al. (2015) also showed a increase in Ti/Al in the Kilian level (fig. 35). Our data display terrigenous increase in the Kilian and Urbino/Paquier levels as well, yet with Ti increasing significantly more than Al, indicating stronger winds at those times. These conditions contrast with those during the deposition of the Jacob level, characterized by lower terrestrial input and higher primary productivity and organic matter preservation.

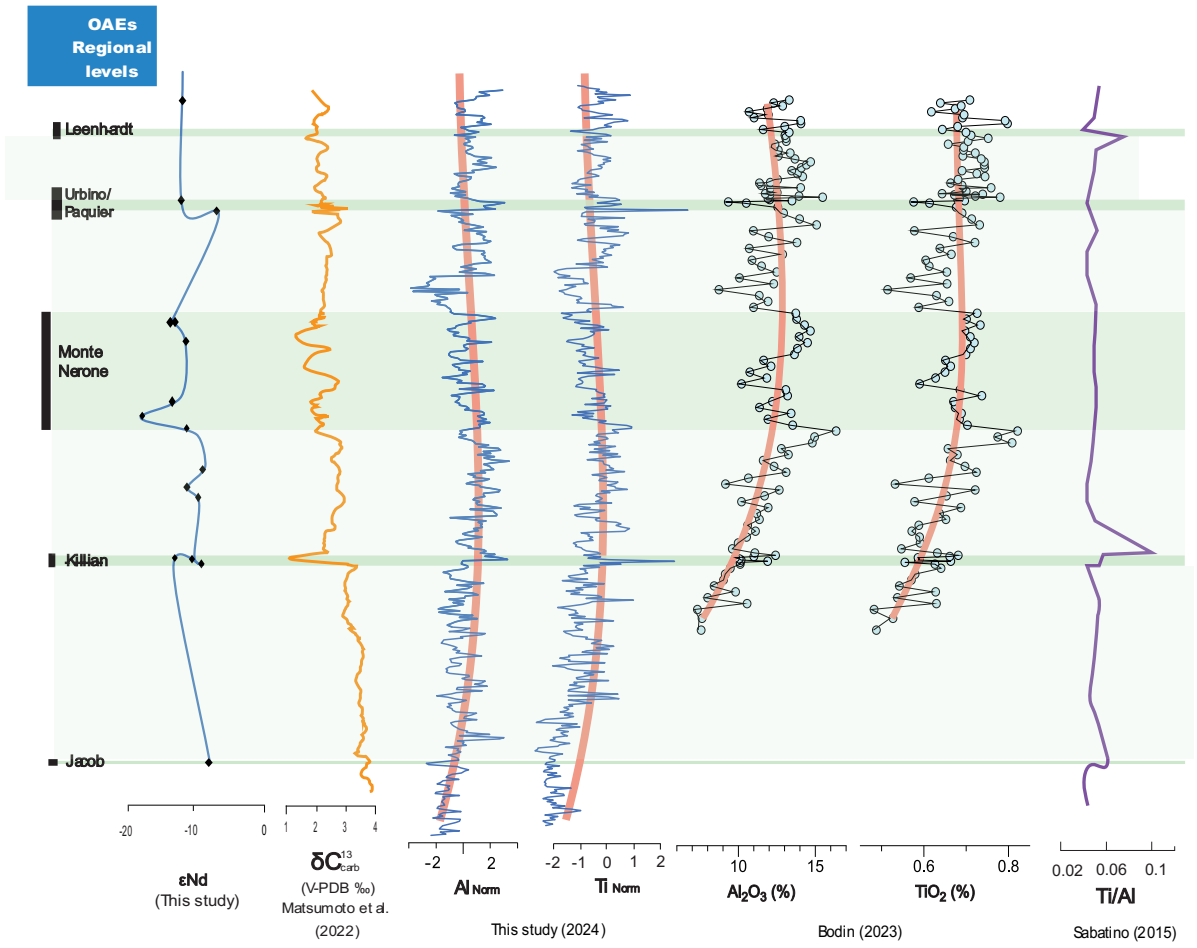

Fig.35: – Integration our new PLG εNd record with published δ13C data from Matsumoto et al. (2022) and elemental data from this study, Bodin et al. (2023), and Sabatino et al. (2015). The resulting composite record reveals a long-term cyclic trend in terrigenous elements, highlighted by the red lines.

The OAE 1b stands out for its unique characteristics, distinguishing it from the more prominent events, such as the OAE 1a and 2. This episode is marked by an unusually prolonged interval of highly unstable conditions, characterized by climatic fluctuations, but not associated to episodes of an extreme disturbance in the global carbon cycle. The geochemical signature of elements is highly variable and unstable across the entire interval but does not display significant differences between the lithofacies from within and out of the OAE 1b interval. Moreover, the anoxic and non-anoxic levels do not display distinct geochemical differences, apart from the relatively higher number of terrigenous elements in the formers. The main black shale layers, Jacob, Killian and Urbino levels, represent episodes of more intense anoxic conditions at regional extent, but the drivers were different from one another. In summary, the climatic and oceanographic conditions in Tethys were particularly unstable during the Aptian-Albian on the long term. They were controlled by a delicate balance of factors and mechanisms, which enhanced the instability during the OAE 1b, without the impulse of a particular external trigger, like for the other OAEs.

5.7. Conclusion

To better understand the mechanisms responsible for the palaeoceanographic changes across the upper Aptian to the lower Albian interval of the OAE 1b in the Poggio le Guaine section, we present a multiproxy geochemical dataset. Our results integrate $\delta^{13}C$, εNd, and geochemical XRF elemental analysis to reconstruct the paleoenvironmental and sedimentary dynamics of OAE1b in PLG section at very high stratigraphic resolution.

The $\delta^{13}C$ record allows the identification of anoxic levels, while the εNd indicates a prolonged period of relatively homogenous sediment provenance.

The red and green intervals exhibit similar geochemical signatures, notably with iron content lacking a distinct correlation with the lithological color variation. This indicates that the change in color could not express deep modifications in the paleoenvironment and, therefore, the ocean was extremely sensitive, even to weak perturbations, during the deposition of the Marne a Fucoidi Formation. This corroborates the theory of an extremely unstable ocean in the Aptian-Albian.

The OAE 1b stands out as an anomalous anoxic event, marked by prolonged duration and extremely unstable climatic and oceanographic conditions. It lacks extreme carbon cycle disruptions, the classical positive $\delta^{13}C$ excursions of the other OAEs, and significant changes

in oceanic circulation, sediment supply, or environmental conditions. The main black shale layers, Jacob, Kilian, and Urbino/Paquier, represent episodes of more intense anoxic conditions at regional scale, at least, related to various mechanisms, not controlled by a single, specific forcing. Therefore, the OAE 1b can be considered just a particularly intense expression of the unstable ocean-climate system of the Aptian-Albian, differently from the other OAEs of the mid-Cretaceous.

CHAPTER 6 | Conclusion and Final Considerations

The results presented in this thesis contribute to the understanding of the minor Oceanic Anoxic Events, particularly the OAE 1b, and the paleoceanographic and paleoenvironmental changes during the Aptian-Albian. For this research we have used geochemical tools such as Carbon Isotopes for the definition of the OAE 1b interval, alongside XRF data and statistical Principal Component Analysis for paleoenvironmental reconstructions, and Neodymium Isotope Composition for tracing the provenance of the detrital fraction in the black shales of the PLG core. The main outcomes of our study are summarized here:

- The PLG εNd record exhibits relatively low values, ranging from -10 to -15, with a slight decrease around the Monte Nerone Level. This shift may be attributed to changes in sediment input from a strong continental source, influenced by varying weathering conditions. The εNd record suggests a relatively constant detrital sediment source throughout the studied interval, without significant shifts during the Killian, Monte Nerone, and Urbino levels. These fluctuations indicate a dominant ancient continental crust (or sedimentary rocks that have been extensively weathered from the continents) as source of εNd values, compatible with measurements from northern Europe and West coast Africa dust sediments.

- The black shales outside and within the OAE 1b interval exhibit short and long-term fluctuations of major and trace elements signatures, indicating that the climatic and oceanographic variations were controlled by similar factors before, during, and after the OAE 1b, but with different intensity. Therefore, the black shale rich layers characterizing the OAE 1b interval in the Marne a Fucoidi Formation testify to an intensification of the warm and wet climatic conditions, instead of perturbations due to additional forcings.

- The geochemical compositions of the red and green intervals are remarkably similar, suggesting that the underlying mechanisms driving anoxic and non-anoxic episodes remained consistent across both depositional environments. The distinct red coloration

can be attributed to the slight oxidation of iron-bearing minerals, which were delivered via the terrigenous supply. In contrast, the green levels exhibit the same Fe content, but in a more reduced state, indicating differences in redox conditions rather than changes in geochemical input

- OAE 1b is a distinct anoxic event characterized by:
  - Prolonged duration with highly-unstable climatic conditions
  - No extreme disturbance in the carbon cycle
  - Global black shale occurrence without the classical positive excursion geochemical signature
  - No significant changes in oceanic circulation, sediment supply, or environmental conditions
  - Unchanged provenance of clay sediments
  - Similar geochemical signature in the whole interval.
  - Black shale levels of regional extent can express relatively more intense anoxic bottom conditions, related to higher detrital input or primary productivity, but not necessarily controlled by orbital forcing.
  - The OAE 1b differs from classical OAEs, such as OAE 1a and 2, presenting unique characteristics.

The comparison of εNd isotopic data for anoxic events is unprecedented and would be suggestive for future research on major anoxic events and other stratigraphic sections. Further investigations will be crucial for elucidating the unique climatic and oceanographic conditions of the Aptian-Albian period and the mechanisms underlying the origin of OAE 1b. Expanding this high-resolution elemental dataset to other OAE intervals within the PLG core and to additional sections will provide invaluable insights into the dynamics of these events.

The dataset produced in this work also contributed to the following scientific publications:

Teixeira, K.M., Savian, J.F., Mello, R.G., Leandro, C.G., Kochhann, M.V., Giorgioni, M., Vidal, P.H.P.C., de Martini, A.P., Jovane, L., Frontalini, F. and Coccioni, R., 2023. Environmental magnetic characterization for the Pialli Level and the Cretaceous Oceanic Red Bed 7 (late Albian, Poggio le Guaine core, central Italy). Global and Planetary Change, 230, p.104281.

Ramos, J.M.F., Savian, J.F., Franco, D.R., Figueiredo, M.F., Frontalini, F., Coccioni, R., Leandro, C.G., Giorgioni, M., Vidal, P.H., Fazio, G. and Jovane, L., 2024. Astronomical calibration of the Ocean Anoxic Event 1b and its implications for the cause of mid-Cretaceous events: a multiproxy record. Paleoceanography & Paleoclimatology, 39, 11, e2024PA004860

REFERENCES

Algeo, T.J., Li, C., 2020. Redox classification and calibration of redox thresholds in sedimentary systems. Geochim. Cosmochim. Acta. https://doi.org/10.1016/j.gca.2020. 01.055. in press (online).

Algeo, T.J., Liu, J., 2020. A re-assessment of elemental proxies for paleoredox analysis, Chemical Geology, Volume 540, 2020, 119549, ISSN 0009-2541, https://doi.org/10.1016/j.chemgeo.2020.119549.

ARTHUR, M. A. and PREMOLI SILVA I., 1982. Development of wide- spread organic carbon-rich strata in the Mediterranean Tethys. In: Schlanger, S. O. and Cita, M. B., Eds., *Nature and origin of Cretaceous carbon-rich facies*, 7–54. London: Academic Press.

Arthur, M.A., Jenkyns, H.C., Brumsack, H.-J., and Schlanger, S.O., 1990. Stratigraphy, geochemistry, and paleoceanography of organic-carbon-rich Cretaceous sequences. *In* Ginsburg, R.N., and Beaudoin, B. (Eds.), *Cretaceous Resources, Events and Rhythms. NATO ASI Ser. 304*: Dordrecht, Netherlands (Kluwer Acad.), 75–119.

Arz, HW et al. (1998): Correlated millennial-scale changes in surface hydrography and terrigenous sediment yield inferred from last-glacial marine deposits off northeastern Brazil. *Quaternary Research*, **50(2)**, 157-166, https://doi.org/10.1006/qres.1998.1992

Bailey, I., Liu, Q., Swann, G.E., Jiang, Z., Sun, Y., Zhao, X. and Roberts, A.P., 2011. Iron fertilization and biogeochemical cycles in the sub-Arctic northwest Pacific during the late Pliocene intensification of northern hemisphere glaciation. *Earth and Planetary Science Letters*, *307*(3-4), pp.253-265.

Batenburg et al (2016). Orbital control on the timing of oceanic anoxia in the Late Cretaceous – Climate of the past, pag.12, 1995–2009.

Barras, C., Mouret, A., Maria Pia Nardelli, Edouard Metzger, Jassin Petersen, Carole La, Helena L. Filipsson, Frans Jorissen, Experimental calibration of manganese incorporation in foraminiferal calcite, Geochimica et Cosmochimica Acta,Volume 237,2018,Pages 49-64,

Barron E. J., Arthur M. A., Kauffman E. G., 1983, Cretaceous rhythmic bedding sequences: a plausible link between orbital variations and climate. Earth and Planetary Science Letters, v. 72, p. 327-340.

Barras, C., Mouret, A., Nardelli, M., Metzger, E., Petersen, J., La, C., Filipsson, H., & Jorissen, F. (2018). Experimental calibration of manganese incorporation in foraminiferal calcite. *Geochimica et Cosmochimica Acta*.

Bayon G., German C. R., Boella R. M., Milton J. A., Taylor R. N. and Nesbitt R. W. (2002) An improved method for extracting marine sediment fractions and its application to Sr and Nd isotopic analysis. Chem. Geol. 187, 179–199. http://dx.doi.org/ 10.1016/s0009-2541(01)00416-8.

Broecker W., S. (2010). "The Oceanic CaCO3 Cycle" in Heinrich D Holland, Karl K. Turekian - Readings from the Treatise on Geochemistry, Academic Press, 2010 – 680 pags.

Bruland, K., R. Middag, M. Lohan (2013). Major controls of trace metals in seawater include nutrient input, dissolved oxygen, and dissolved metals, with a focus on phosphorus and nitrogen (2013).

Bennett, W.W, Canfield. Redox-sensitive trace metals as paleoredox proxies: A review and analysis of data from modern sediments Earth-Sci. Rev. (2020), Article 103175.

Bodin, S., Charpentier, M.,Ullmann., Rudra, A., Sanei, H. (2023) Carbon Cycle during the late Aptian-early Albian OAE 1b: A Focus on the Killian-Paquier levels interval. Global and Planetary Change 222 (2023) 104074.

Bom, M., Ceolin, D., Kochhann, K., Krahl, G., Fauth, G., Bergue, C., Savian, J., Junior, O., Simões, M., & Assine, M. (2021). Paleoenvironmental evolution of the Aptian Romualdo Formation, Araripe Basin, Northeastern Brazil. Global and Planetary Change, 203, 103528. https://doi.org/10.1016/J.GLOPLACHA.2021.103528.

Boyd, Philip & Ellwood, Michael. (2010). The biogeochemical cycle of iron in the ocean. Nature Geoscience - NAT GEOSCI. 3. 10.1038/ngeo964.

Boyd, P. (2013). Ocean Iron Cycle. , 187, 161-179. https://doi.org/10.1029/2008GM000775.

Breheret, J.-G., 1997. L'Aptien et l'Albien de la fosse vocontienne (des bordures au bassin). Evolution de la s´edimentation et enseignements sur les´ev´enements anoxiques. In: Soci´et´e G´eologique du Nord, Publication n◦ 25, p. 614.

Breheret, J.-G., Crumi`ere, J.-P., 1989. Organic-rich episodes in the mid-Cretaceous (Aptian to Turonian) pelagic realm of the Vocontian Basin (SE France). Geobios, m´emoire sp´ecial 11, 205–210.

Bruggmann, S., Severmann, S., & McManus, J. (2020). Marine Sediments as a Source of Dissolved Nickel to the Global Ocean. *Goldschmidt Abstracts*. https://doi.org/10.46427/gold2020.274.

Burdige, D. (1993). The biogeochemistry of manganese and iron reduction in marine sediments. *Earth-Science Reviews*, 35, 249-284. https://doi.org/10.1016/0012-8252(93)90040-E.

Burns, V., & Burns, R. (1978). Post-depositional metal enrichment processes inside manganese nodules from the north equatorial Pacific. *Earth and Planetary Science Letters*, 39, 341-348. https://doi.org/10.1016/0012-821X(78)90020-1.

Cameron, V., & Vance, D. (2014). Heavy nickel isotope compositions in rivers and the oceans. *Geochimica et Cosmochimica Acta*, 128, 195-211. https://doi.org/10.1016/J.GCA.2013.12.007.

Caetano-Filho, S., Dias-Brito, D., Rodrigues, R., de Azevedo, R.L.M., 2017. Carbonate microfacies and chemostratigraphy of a late Aptian–early Albian marine distal section from the primitive South Atlantic (SE Brazilian continental margin): record of global ocean-climate changes? Cretac. Res. 74, 23–44.

Cameron, V., Vance, D. (2014). Heavy nickel isotope compositions in rivers and the oceans, Geochimica et Cosmochimica Acta, Volume 128, 2014, Pages 195-211,

Coccioni, R., Franchi, R., Nesci, O., PerilliI, N., Wezel, F. C. and Battistini, F.,1990b. Stratigrafia, micropaleontologia e mineralogia delle Marne a Fucoidi delle sezioni di Poggio le Guaine e del Fiume Bosso (Appennino umbro–marchigiano). In: Comitato Centinario Raffaele Piccinini Ed., Atti 3° Convegno Internazionale "Fossili, Evoluzione, Ambiente", Pergola, 21–28 Ottobre 1990, 1. Ostra Vetere (AN) Italy, Tecnostampa.

Coccioni, **R., 2012**. Umbria-Marche Basin, Central Italy: A Reference Section for the Aptian-Albian Interval at Low Latitudes. Scientific Drilling, No. 13, April 2012.

Coccioni, **R., 2014.** The neglected history of Oceanic Anoxic Event 1b: insights and new data from the Poggio le Guaine section (Umbria–Marche Basin). Stratigraphy, vol. 11, nos. 3– 4, pp. 245–282, text figures 1– 6, table 1, plates 1-5, 2014.

Elderfield, H. 1976. Manganese fluxes to the oceans. (1 june 1976).

Erba, E., 1992. Calcareous nannofossil distribution in pelagic rhythmic sediments (Aptian-Albian Piobbico core, central Italy). *Riv. Ital. Paleont. Strat.*, 97:455–484. CONFERIR O 1991.

Elderfield, H. (1976). Manganese fluxes to the oceans. *Marine Chemistry*, 4, 103-132. https://doi.org/10.1016/0304-4203(76)90001-3.

Erba, E., Tremolada, F., 2004. Nannofossil carbonate fluxes during the Early Cretaceous: phytoplankton response to nutrification episodes, atmospheric CO2 and anoxia. Paleoceanography 19, 1–18. http://dx.doi.org/10.1029/2003PA000884.

Erbacher, J., 1994. Entwicklung und Pal¨aoozeanographie mittelkretazischer Radiolarien der westlichen Tethys (Italien) und des Nordatlantiks. Tübinger Mikropal¨aontogische Mitteilungen 12, 1–120.

Erbacher, J., Hemleben, C., Huber, B.T., Markey, M., 1999. Correlating environmental changes during early Albian oceanic anoxic event 1B using benthic foraminiferal paleoecology. Mar. Micropaleontol. 38, 7–28.

Erbacher, J., Huber, B.T., Norris, R.D., Markey, M., 2001. Increased thermohaline stratification as a possible cause for an ocean anoxic event in the Cretaceous period. Nature 409, 325–327.

Erbacher J., Friedrich O., Wilson P. A., Lehmann J., Weiss W., 2011, Short-term warming events during the boreal Albian (mid-Cretaceous). Geology, v. 39, n. 3, p. 223-226, doi: 10.1130/G31606.1

Fujimaki H., Shinjo R., Asahara Y., Tanimizu M. and Dragusanu C. (2000) JNdi-1: A neodymium isotopic reference in consistency with LaJolla neodymium. Chemical Geology. 168, 279– 281. http://dx.doi.org/10.1016/s0009-2541(00)00198-4.

Gambacorta, G. et al. Carbon-and oxygen-isotope records of mid-Cretaceous Tethyan pelagic sequences from the Umbria–Marche and Belluno Basins (Italy). N. Stratigr. 48, 299–323 (2015).

Giorgioni, M., Weissert, H., Bernasconi, S.M., Hochuli, P.A., Coccioni, R., Keller, C.E., 2012. Orbital control on carbon cycle and oceanography in the mid-Cretaceous greenhouse. Paleoceanography 27, PA1204.

Giorgioni, M., Weissert, H., Bernasconi, S.M., Hochuli, P.A., Keller, C.E., Coccioni, R., Petrizzo, M.R., Lukeneder, A., Garcia, T.I., 2015. Paleoceanographic changes during the Albian-Cenomanian in the Tethys and North Atlantic and the onset of the Cretaceous chalk. Glob. Planet. Chang. 126, 46–61.

Greenacre, Michael & Groenen, Patrick & Hastie, Trevor & Iodice D'Enza, Alfonso & Markos, Angelos & Tuzhilina, Elena. (2022). Principal component analysis. Nature Reviews Methods Primers. 2. 100. 10.1038/s43586-022-00184-w.

Grippo A., Fischer A. G., Hinnov L. A., Herbert T. D., Premoli Silva I., 2004, Cyclostratigraphy and Chronology of the Albian Stage (Piobbico core, Italy), in: Cyclostratigraphy: approaches and case histories. SEPM Special Publication 81, p. 57-81

Han, T., Fan, H., & Wen, H. (2018). Dwindling vanadium in seawater during the early Cambrian, South China. Chemical Geology. https://doi.org/10.1016/J.CHEMGEO.2018.05.022.

Haq B. U., Hardenbol J., Vail P. R., 1987. Chronology of Fluctuating Sea Levels Since the Triassic: Science, v. 235, n. 4793, p. 1156-1167, doi: 10.1126/science.235.4793.1156

Harlavan, Y., Kedem, N., Dor, Y., Avigad, D., Morag, N., & Calvo, R. (2021). Constructing the provenance of siliciclastic sediments using their clay fraction. *Goldschmidt2021 abstracts*. https://doi.org/10.7185/gold2021.8046.

Hay W., 2008, Evolving ideas about the Cretaceous climate and ocean circulation. Cretaceous Research, v. 29, p. 725-753

Hindshaw, R. S., Tosca, N. J., Piotrowski, A. M., and Tipper, E. T.: Clay mineralogy, strontium and neodymium isotope ratios in the sediments of two High Arctic catchments (Svalbard), Earth Surf. Dynam., 6, 141–161, https://doi.org/10.5194/esurf-6-141-2018, 2018.

Herbert T. D. & Fischer A. G., 1986. Milankovitch climatic origin of the mid-Cretaceous black shale rhythms in central Italy: Nature, v. 321, n. 19, p. 739-743.

Herrle, J. O., Kossler, P., Friedrich, O., Erlenkeuser, H., Hemleben, C., 2004. High resolution carbon isotope records of the Aptian to lower Albian from SE France and the Mazagan Plateau (DSDP Site 545); a stratigraphic tool for paleoceanographic and paleobiologic reconstruction. Earth and Planetary Science Letters, 218: 149-161.

Huber B. T., Norris R. D., MacLeod K. G., 2002, Deep-sea paleotemperature record of extreme warmth during the Cretaceous. Geology, v. 30, n. 2, p. 123-126

Hulten, M.M.P, A. Sterl, A. Tagliabue, J.-C. Dutay, M. Gehlen, H.J.W. de Baar, R. Middag. Aluminium in an ocean general circulation model compared with the West Atlantic Geotraces cruises, Journal of Marine Systems, Volume 126, 2013, Pages 3-23.

Huxley T. H., 1968. On a Piece of Chalk: Macmillan's Magazine

Jenkyns, H.C., 1980. Cretaceous anoxic events: from continent to oceans. J. Geol. Soc. Lond. 137, 171–188.

Jenkyns, H. (2010). Geochemistry of oceanic anoxic events. *Geochemistry*, 11. https://doi.org/10.1029/2009GC002788.

Leckie, R.M., Bralower, T.J., Cashman, R., 2002. Oceanic anoxic events and plankton evolution: biotic response to tectonic forcing during the mid-Cretaceous. Paleoceanography 17 (3), 1–29.

Middag, R., Baar, D., Laan, P., & Bakker, K. (2009). Dissolved aluminium and the silicon cycle in the Arctic Ocean. *Marine Chemistry*, 115, 176-195. https://doi.org/10.1016/J.MARCHEM.2009.08.002.

Miller K. G., Kominz M. A., Browning J. V., Wright J. D., Mountain G. S., Katz M. E., Sugarman P. J., Cramer B. S., Christie-Blick N., Pekar S. F., 2005, The Phanerozoic Record of Global Sea-Level Change: Science, v. 310, n. 5752, p. 1293-1298, doi: 10.1126/science.1116412.

Minming Cui, George W. Luther, Maya Gomes. Constraining the major pathways of vanadium incorporation into sediments underlying natural sulfidic waters, Geochimica et Cosmochimica Acta, Volume 359, 2023, Pages 148-164.

Mutterlose, J., & Alsen, P. (2009). The Early Cretaceous of North-East Greenland: A crossroads of belemnite migration. In *Abstract volume* (pp. 186-187). University of Plymouth.

Moran, S., & Moore, R. (1988). Evidence from mesocosm studies for biological removal of dissolved aluminium from sea water. *Nature*, 335, 706-708.

Mortimore - A chalk revolution What have we done to the Chalk of England. Proceedings of the Geologists' Association, 2011.

Kenneth W. Bruland. Oceanographic distributions of cadmium, zinc, nickel, and copper in the North Pacific, Earth and Planetary Science Letters, Volume 47, Issue 2,1980, Pages 176-198

Kraft, S., Frank, M. Hathorne, H.C, Weldeab, S (2013). Assessment of seawater Nd isotope signatures extracted from foraminiferal shells and authigenic phases of Gulf of Guinea sediments. Geochimica et Cosmochimica Acta 121 (2013) 414–435.

Larson, R. L., and E. Erba (1999), Onset of the mid-Cretaceous greenhouse in the Barremian-Aptian: Igneous events and the biological, sedimentary, and geochemical responses, Paleoceanography, 14(6), 663–678, doi:10.1029/1999PA900040.

Leckie, R.M., Bralower, T.J., Cashman R. (2002). Oceanic anoxic events and plankton evolution: biotic response to tectonic forcing during the mid–Cretaceous. Paleoceanography 17, 13 – 29. doi: 10.1029/2001PA000623

Liu, J., Shi, X., Chen, L., Huang, Y., Wang, Y., Cui, Y., & Bu, W. (2005). REE and εNd of clay fractions in sediments from the eastern Pacific Ocean: Evidence for clay sources. *Science in China Series D: Earth Sciences*, 48, 701-712. https://doi.org/10.1360/03YD0276.

Lugmair, G.W., Marti, K., Lunar initial 143Nd/144Nd: Differential evolution of the lunar crust and mantle, Earth and Planetary Science Letters, Volume 39, Issue 3,1978, Pages 349-357, ISSN 0012-821X, https://doi.org/10.1016/0012-821X(78)90021-3.

Mortimore R., 2011. A chalk rhuxevolution: what have we done to the Chalk of England: Proceedings of the Geologists' Association, v. 122, p. 232–297.

Matsumoto, H., Kuroda, J., Coccioni, R., Frontalini, F., Sakai, S., Ogawa, O., Ohkouchi, N. Marine Os isotopic evidence for multiple volcanic episodes during Cretaceous Oceanic Anoxic Event 1b. Scientific Reports 10, article number 12601. 28 july, 2020.

Matsumoto, H., Shirai, K., Huber, B.T., MacLeod, K.G., Kuroda, J., 2023. High-resolution marine osmium and carbon isotopic record across the Aptian–Albian boundary in the southern South Atlantic: evidence for enhanced continental weathering and ocean acidification. Palaeogeogr. Palaeoclimatol. Palaeoecol. 613, 111414.

Middag, R., Baar, D., Laan, P., & Bakker, K. (2009). Dissolved aluminium and the silicon cycle in the Arctic Ocean. *Marine Chemistry*, 115, 176-195. https://doi.org/10.1016/J.MARCHEM.2009.08.002.

Mitchell et al (2008). Oceanic anoxic cycles Orbital prelude to the Bonarelli Level (OAE 2). EPSL, 267, 1-16

Moosavizadeh, M., Mahboubi, A., Moussavi-Harami, R., & Kavoosi, M. (2014). Early Aptian oceanic anoxic event (OAE 1a) in Northeastern Arabian Plate setting: an example from Dariyan Formation in Zagros fold–trust belt, SE Iran. Arabian Journal of Geosciences, 7, 4745-4756. https://doi.org/10.1007/s12517-013-1025-z.

Mort, H.P., Adatte, T., Follmi, K.B., Keller, G., Steinmann, P., Matera, V., Berner, Z., Stüben, D., 2007a. Phosphorus and the roles of productivity and nutrient recycling during oceanic anoxic event 2. Geology 35, 483–486.

Navarro-Ramirez, J.-P., Bodin, S., Heimhofer, U., Immenhauser, A., 2015. Record of Albian to early Cenomanian environmental perturbation in the eastern sub- equatorial Pacific. Palaeogeogr. Palaeoclimatol. Palaeoecol. 423, 122–137.

Orians, K., Boyle, E., & Bruland, K. (1990). Dissolved titanium in the open ocean. *Nature*, 348, 322-325. https://doi.org/10.1038/348322A0.

Petrizzo, M.R., Huber, B.T., Gale, A.S., Barchetta, A., Jenkyns, H.C., 2012. Abrupt planktic foraminiferal turnover across the Niveau Kilian at Col de Pr´e-Guittard (Vocontian Basin, southeast France): new criteria for defining the Aptian/Albian boundary. Newslett. Stratigr. 45, 55–74.

Peybernes, C., Giraud, F., Jaillard, E., Robert, E., Masrour, M., Aoutem, M., Icame, N., 2013. Stratigraphic framework and calcareous nannofossil productivity of the Essaouira-Agadir Basin (Morocco) during the Aptian-Early Albian: comparison with the north-Tethyan margin. Cretac. Res. 39, 149–169.

Phelps, R.M., Kerans, C., Da-Gama, R.O.B.P., Jeremiah, J., Hull, D., Loucks, R.G., 2015. Response and recovery of the Comanche carbonate platform surrounding multiple Cretaceous oceanic anoxic events, northern Gulf of Mexico. Cretac. Res. 54, 117–144.

Price, G.D., 2003. New constraints upon isotope variation during the early Cretaceous (Barremian-Cenomanian) from the Pacific Ocean. Geol. Mag. 140, 513–522.

Premoli Silva, I., Erba, E., Tornaghi, M., 1989. Paleoenvironmental signals and changes in surface fertility in Mid Cretaceous Corg-rich pelagic facies of the Fucoid Marls (Central Italy). Geobios Mém. Spec. 11, 225–236. http://dx.doi.org/10.1016/S0016- 6995(89)80059-2.

Pucéat E., Lecuyer C., Sheppard S. M. F., Dromart G., Reboulet S., Grandjean P., 2003, Thermal evolution of Cretaceous Tethyan marine waters inferred from oxygen isotope composition of fish tooth enamels. Paleoceanography, v. 18, n. 2. p. 1029- 1039, doi:10.1029/2002PA000823

Ramos, J. M. F., Savian, J. F., Franco, D. R., Figueiredo, M. F., Leandro, C. G., Frontalini, F., et al. (2024). Astronomical calibration of the ocean anoxic event 1b and its

implications for the cause of mid- cretaceous events: A multiproxy record. *Paleoceanography and Paleoclimatology*, *39*, e2024PA004860. https://doi.org/10. 1029/2024PA004860

Robinson, S., Ivanovic, R., Tina van de Flierdt, Cécile L. Blanchet, Kazuyo Tachikawa, Ellen E. Martin, Carys P. Cook, Trevor Williams, Lauren Gregoire, Yves Plancherel, Catherine Jeandel, Thomas Arsouze. Global continental and marine detrital εNd: An updated compilation for use in understanding marine Nd cycling. Chemical Geology, Volume 567, 2021.

Sabatino, N., Coccioni, R., Manta, D.S., Baudin, F., Vallefuoco, M., Traina, A., Sprovieri, M., 2015. High-resolution chemostratigraphy of the late Aptian – early Albian oceanic anoxic event (OAE 1b) from the Poggio le Guaine section (Umbria – Marche Basin, central Italy). Palaeogeography, Palaeoclimatology, Palaeoecology 426, pag. 319 – 333

Schlanger, S.O., and Jenkyns, H.C., 1976. Cretaceous oceanic anoxic events: Causes and consequences. *Geol. Mijnbouw*, 55:179–184.

Scheuvens, D., Shutz, L, Kandler, K., Ebert, M., Weinbruch, S. Bulk composition of northern Africa dust and its source sediments – a compilation. Earth Science rev. (2013).

Sclater, F., Boyle, E., & Edmond, J. (1976). On the marine geochemistry of nickel. *Earth and Planetary Science Letters*, 31, 119-128. https://doi.org/10.1016/0012-821X(76)90103-5.

Stille, P., Clauer, N., & Abrecht, J. (1989). Nd isotopic composition of Jurassic Tethys seawater and the genesis of Alpine Mn-deposits: Evidence from Sr-Nd isotope data. *Geochimica et Cosmochimica Acta*, 53, 1095-1099. https://doi.org/10.1016/0016-7037(89)90214-7.

Sun, X., Higgins, J., & Turchyn, A. (2016). Diffusive cation fluxes in deep-sea sediments and insight into the global geochemical cycles of calcium, magnesium, sodium and potassium. *Marine Geology*, 373, 64-77. https://doi.org/10.1016/J.MARGEO.2015.12.011.

Tachikawa K., Arsouze, T., Bayon, G., Bory, A., Colin, C., et al. The large-scale evolution of neodymium isotopic composition in the global modern and Holocene Ocean revealed from seawater and archive data. Chemical Geology, 2017, 457, pp.:131-148 (IF 3,482). 10.1016/j.chemgeo.2017.03.018 . hal-01497960

Tanaka T., Togashi S., Kamioka H., Amakawa H., Kagami H., Hamamoto T., Yuhara M., Orihashi Y., Yoneda S., Shimizu H., Kunimaru T., Takahashi K., Yanagi T., Nakano T., Tarduno (1991) …

Tiraboschi, D., Erba, E., Calcareous nannofossil biostratigraphy (Upper Bajocian–Lower Bathonian) of the Ravin du Bès section (Bas Auran, Subalpine Basin, SE France): Evolutionary trends of Watznaueria barnesiae and new findings of ‘‘Rucinolithus’’ morphotypes. Geobios (2009), doi:10.1016/j.geobios.2009.10.002

Trabucho Alexandre, J., Van Gilst, R.I., Rodríguez-López, J.P., De Boer, P.L., 2011. The sedimentary expression of oceanic anoxic event 1b in the North Atlantic. Sedimentology58,1217–1246.http://dx.doi.org/10.1111/j.136

Tréguer1, P.J., Jill N. Sutton1, Mark Brzezinski3, Matthew A. Charette4, Timothy Devries5, Stephanie Dutkiewicz6, Claudia Ehlert7, Jon Hawkings8,9, Aude Leynaert1, Su Mei Liu, et al (2021). The biogeochemical cycle of silicon in the modern ocean. Biogeosciences, 18, 1269–1289, 2021 https://doi.org/10.5194/bg-18-1269-2021.

Tribovillard, N., Algeo, T. J., Lyons, T., & Riboulleau, A. (2006). Trace metals as paleoredox and paleohydrologic proxies: An update. Chemical Geology, 232(3-4), 12-32.

Turgeon, S., Brumsack, H. (2006). Anoxic vs dysoxic events reflected in sediment geochemistry during the Cenomanian–Turonian Boundary Event (Cretaceous) in the Umbria–Marche Basin of central Italy. Chemical Geology 234 (2006) 321-339

Yannick. M., 2017. Contrôles sur la répartition des argiles organiques dans les bassins profonds : cas de l'Atlantique central au Crétacé. Université Toulouse 3 Paul Sabatier (UT3 Paul Sabatier).

Wagner, T., Herrle, J.O., Sinninghe Damsté, J., Schouten, S., Stuesser, I., Hofmann, P., 2008. Rapid warming and salinity changes of Cretaceous surface waters in the subtropical North Atlantic. Geology 36, 203–206. http://dx.doi.org/10.1130/G24523A.1.

Wang, Y., Bodin, S., Blusztajn, J.S., Ullmann, C.V., Nielsen, S.G., 2022. Orbitally-paced global oceanic deoxygenation decoupled from volcanic CO2 emission during the middle Cretaceous OAE 1b (Aptian-Albian transition). Geology 50, 1324–1328.

Wehausen, R., Brumsack, H., (2002). Astronomical forcing of the East Asian monsoon mirrored by the composition of Pliocene South China Sea sediments. Earth and Planetary Science Letters 201 (2002) 621- 636.

Wittkop, Chad & Swanner, Elizabeth & Grengs, Ashley & Lambrecht, Nicholas & Fakhraee, Mojtaba & Myrbo, Amy & Bray, Andrew & Poulton, Simon & Katsev, Sergei. (2020). Evaluating a primary carbonate pathway for manganese enrichments in reducing environments. Earth and Planetary Science Letters. 538. 10.1016/j.epsl.2020.116201.

Wortmann U., Hesse R., Zacher W., 1999, Major-element analysis of cyclic black shales: Paleoceanographic implications for the Early Cretaceous deep western Tethys: Paleoceanography, v. 14, n. 4, p. 525-541.

Wu ingzhe, Leopoldo D. Pena, Robert F. Anderson, Alison E. Hartman, Louise L. Bolge, Chandranath Basak, Joohee Kim, Micha J.A. Rijkenberg, Hein J.W. de Baar, Steven L. Goldstein. Assessing neodymium isotopes as an ocean circulation tracer in the Southwest Atlantic, Earth and Planetary Science Letters, Volume 599, 2022, Volume 599.

Xu, H., & Weber, T. (2021). Ocean Dust Deposition Rates Constrained in a Data-Assimilation Model of the Marine Aluminum Cycle. *Global Biogeochemical Cycles*, 35. https://doi.org/10.1029/2021GB007049.